Title

Surface Engineering Hybrid Organic − Inorganic Molecules − Nanocrystals for Functional Nanomaterials

Author

Xia, Pan

Publication Date

2019

UNIVERSITY OF CALIFORNIA
RIVERSIDE

Surface Engineering Hybrid Organic − Inorganic Molecules − Nanocrystals for Functional Nanomaterials

A Dissertation submitted in partial satisfaction
of the requirements for the degree of

Doctor of Philosophy

in

Materials Science and Engineering

by

Pan Xia

December 2019

Dissertation Committee:
- Dr. Ming Lee Tang, Chairperson
- Dr. Lorenzo Mangolini
- Dr. Ruoxue Yan

The Dissertation of Pan Xia is approved:

____

____

____
Committee Chairperson

University of California, Riverside

Acknowledgements

It’s very exciting to prepare my PhD dissertation after 5-year study. This is an unforgettable experience full of exploring, challenges, excitement, struggling and happiness. It is such an enjoyable, passionate and exhilarating experience to work with my advisor and lab mates in UC Riverside. I have learnt a lot from this experience both as a scientist, and on a personal level, and it will be the memory of my whole life. Here, I would like to thank people who have helped me so much throughout my Ph.D. study.

I would like to sincerely appreciate the help from my advisor Dr. Ming Lee Tang, who have guide me my 5-year PhD research. Without her support and training, I couldn’t finish all works in the dissertation.

I would like to thank my family members. My grandmothers, Jiulian Huang and Xuelian Hu, brought me up and support my education. My parents, Chiyuo Xia and Meiying Xiao, who bring me life and spend their best times to earn money to support my education. It’s rare in a rural area of China to support a girl’s education to University and even graduate school. My younger brother, Yong Xiao, give me a lot of personal support and companion.

I would like to thank my committee members, Dr. Lorenzo Mangolini, in research and Dr. Ruoxue Yan. Dr. Lorenzo Mangolini collaborated with my research projects and gave me a lot of suggestions and supports. Dr. Ruoxue Yan are very helpful in research and classes. And my oral exam committee members, Dr. Bryan M. Wong, Dr. Alexander Greaney, Dr. Valentine I. Vullev and Dr. David Bocian. I want to thank all my lab mates who provided me a lot of help in my research. They are Xin Li, Zhiyuan Huang, Melika Mahboub, Tingting Huang, Emily Moses, Kefu Wang, Lloyd Kao, Vi Dao, Timothy Koh, Zhongxiang Wang, Bo Yin and Carter Gerke and all the alumni who have helped me.

I would like to thank all my collaborators from whom I have learned a lot. Dr. Valentine Vullev, Dr. Chun Hung Lui, Juan J. Romero, Jieying Jiao, Jeremiah van Baren, Dr. George Shu Heng Pau, Dr. Kenneth R. Graham, Zhiming Liang, Daniel W. Davies, Bijal B. Patel, Ying Diao, Maotong Qin, Joseph Schwan, Emily K. Raulerson, Devin Coleman, Dr. Lorenzo Mangolini and Dr. Sean T. Roberts.

I also want to thank all people gives me help in my research, including Dr. Krassimir Bozhilov, Dr Yongtao Cui, Dr. Junchen Guo, Linxiao Geng, Dan Borchardt, Erfu Liu, Mashael Altaiary and Xiong Huang.

I would like to thank all funding that support my research under Ming Lee Tang's guidance, including Army Research Office (ARO), Nature Science Foundation (NSF), Department of Energy (DOE), Alfred P. Sloan Foundation and Samsung GRO American.

December 3, 2019

Pan Xia

Acknowledgement of previously published materials

1. Xia P, Huang Z, Li X, Romero JJ, Vullev VI, Pau GSH, et al. On the efficacy of anthracene isomers for triplet transmission from CdSe nanocrystals. Chemical Communications 2017, 53(7): 1241-1244.

2. Xia P, Liang Z, Mahboub M, van Baren J, Lui CH, Jiao J, et al. Surface Fluorination for Controlling the PbS Quantum Dot Bandgap and Band Offset. Chemistry of Materials 2018, 30(15): 4943-4948.

3. Xia P, David DD, Patel BB, Qin M, Liang Z, Graham KR, et al. Spin-coated fluorinated PbS QD superlattice thin film with high hole mobility. 2019 (submitted).

4. Xia P, Raulerson EM, Coleman D, Gerke CS, Lorenzo Mangolini, et al Achieving Spin-triplet Exciton Transfer between Silicon and Molecular Acceptors for Photon Upconversion. Nature Chemistry, 2019 doi:10.1038/s41557-019-0385-8.

The co-author, Ming Lee Tang, listed in all publications directed and supervised the research which forms the basis for this dissertation.

ABSTRACT OF THE DISSERTATION

Surface Engineering Hybrid Organic − Inorganic Molecules − Nanocrystals for Functional Nanomaterials

by

Pan Xia

Doctor of Philosophy, Graduate Program in Materials Science and Engineering
University of California, Riverside, December 2019
Dr. Ming Lee Tang, Chairperson

Hybrid organic nanocrystal materials outstand as good candidates in photovoltaic cells, photodetectors, light emitting devices, phototherapies and optogenetics applications due to controllable bandgap via varying size and shape in synthesis and tunable optical and electronic properties via surface modification. My dissertation is mainly focusing on two parts: (a) Chemically surface modification of semiconductor nanocrystals with anthracene derivatives to serve as triplet sensitization in energy transfer process (b) Chemically surface modification lead sulfide semiconductor nanocrystals to tune band offsets and alignment of PbS QDs in thin film transistors.

Starting from anchoring anthracene carboxylic acid and anthracene dithiocarbamate acid isomers on CdSe nanocrystal surface to investigate how molecular orientation and orbital overlap affects triplet energy transfer from NC donor to anthracene transmitter on the hybrid photon upconversion system. We are interested in the effect of isomeric substitutions on the transmitter for triplet energy transfer between nanocrystal donor and molecular acceptor. Each isomeric acceptor is expected to bind in a unique orientation with respect to the NC donor. We see that this orbital overlap drastically affects the transmission of triplets and small

perturbations to molecular structure can drastically realign the relative levels of excited states, thus impacting TET transfer in this hybrid platform.

Photostable nontoxic and earth abundant hybrid semiconductor nanocrystals are in demand for triplet sensitization in biological and environmentally-sensitive applications including phototherapy and bioimaging. However, hybrid nanocrystal materials applied in triplet sensitization to date have made exclusive use of NCs containing toxic elements or expensive rare earth elements. We address this challenge by chemically functionalizing non-toxic silicon NCs with triplet-accepting anthracene ligands, upconverting 488 – 640 nm photons to 425 nm violet light further for biological use.

Fully fluorinated perfluorocarbon ligands are shown to modify the energetics and dielectric environment of quantum dots resulting in a large hypsochromic shift in the optical gap. This work shows that electron-withdrawing halogens like fluorine and chlorine can control the bandgap and band offsets of nanocrystals for the future design and optimization of functional organic/inorganic hybrid nanostructures.

Motivated by the oleophobic and electron-withdrawing nature of perfluorocarbons, I explore the effect of a trifluoromethyl coating on lead sulfide quantum dots in thin film transistor geometry. The low surface energy conferred by the oleophobic perfluorocarbons creates QDs packed in a primitive cubic lattice with long range order.

Table of Contents

List of Figures

List of Tables

2 Chapter 1. Introduction

1.1 Introduction to surface engineering semiconductor nanocrystals

The ability to synthesize high-quality, size-tunable and shape-tunable colloidal semiconductor nanocrystals has made it building blocks in nanotechnology area. Moreover, semiconductor nanomaterials have widely applied in photovoltaic cells, photodetector[1], light emitting devices[2], phototherapy[3, 4] and optogenetics[4] arising from their size-dependent and surface-dependent optical and electronic properties. These applications require control of the photophysical properties of NCs, which are directly influenced by the surface chemistry. Surface ligands of NCs could induce trap states and tuning the energy levels of semiconductor nanocrystals. Two well-known examples of the effect are addition of thiol molecules on NC surface quenching band edge emission of NCs [5] and surface ligand of NCs tuning the its energy levels.[6] However, atomic and molecular understanding surface chemistry of NCs and how it affect the optical and electronic properties of NCs are still under investigation.

Most synthetic routes to high-quality NCs with tunable sizes and shapes mostly employ long hydrocarbon molecules containing a coordinating headgroup such as oleic acid (OA), phosphonic acid and oleylamine as ligands, which sterically stabilize NCs in nonpolar, hydrophobic solvents but behave as physical barrier in energy transfer and charger transfer within NCs. Thus, replace surface long insulating ligands with functional semiconductor organic molecules to serve as energy transfer transmitter or with short ligand in length to not only tuning the energy levels but also forming conducting thin film are the extensively used strategies in surface engineering semiconductor nanocrystals field.[6]

However, designing and fabricating functional hybrid inorganic-semiconductor NCs with organic molecules are still to meet specific requirements are still difficult due to different properties of various semiconductor materials and surface ligands, different force between ligands and NC[7] and challenge to correlate the NC surface to its electronic properties. In this dissertation, on one part, semiconductor nanocrystals have been functionalized with conjugated organic molecules (like acene) to retain the mechanical strength and electronic properties of the inorganic portion, the processability and ease of functionalization of the organic constituents, while directing energy at nanoscale dimensions by control of multi-excitonic processes, seen examples in Fig. 1.1. On the other part, semiconductor nanocrystals are surface modified with ionic bond short ligands to tune the energy levels hence controlling band alignment in quantum dots (QD) based thin film solar cells and tuning surface energy of semiconductor nanocrystals to obtain periodic alignment in thin film-based devices (see Fig.1.2). Several characterizations methods have applied to characterize ligands on NC surface, including nuclear magnetic resonance (NMR), infrared spectroscopy and x-ray photoelectron spectroscopy (XPS).

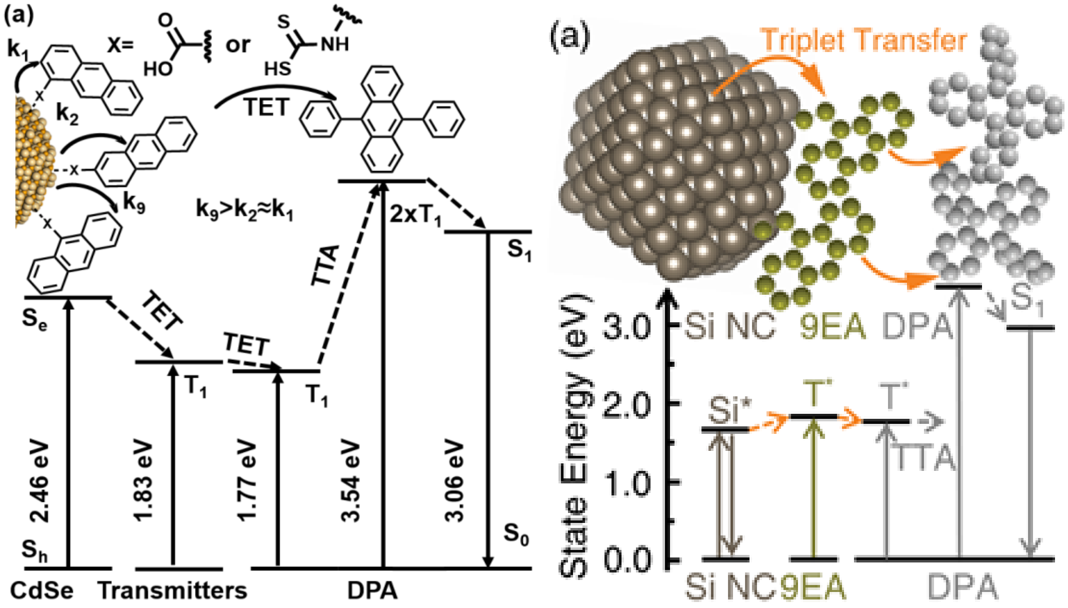

Fig. 2.1 (a) Schematic of the energy transfer in this hybrid photon upconversion system, with 2.39 nm diameter CdSe nanocrystals (NCs) as sensitizer and 9,10-diphenylanthracene (DPA) as annihilator. Isomeric anthracene derivatives functionalized with carboxylic acid and dithiocarbamate binding groups at the 1-, 2- and 9- positions on the aromatic ring serve as transmitter ligands with different rates of triplet energy transfer for each isomer (k1, k2 and k9 respectively). (b) Schematic illustration of Si NC based photon upconversion. Light absorbed by Si NCs produces an excited electron-hole pair that transfers to 9-ethyl anthracene (9EA), forming a molecular spin-triplet exciton. Excited 9EA molecules then transfer these excitons to DPA molecules diffusing in solution. Higher energy photons are emitted after triplet-triplet annihilation (TTA) between pairs of excited DPA molecules.

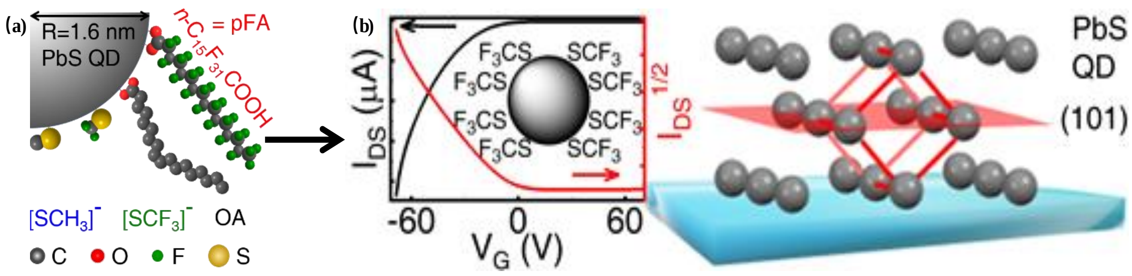

Fig. 2.2 (a) PbS QDs (diameter = 3.3 nm) with perfluorohexadecanoic acid (pFA), trifluoromethane thiolate (-SCF$_3$), methanethiolate, (-SCH$_3$), and oleic acid (OA) ligands. (b) Partial ligand exchanged PbS@SCF$_3$ is further ligand exchanged with [NMe$_4$][SCF$_3$] in thin film and form superlattice thin film transistors.

1.2 Surface modification semiconductor nanocrystals for photon upconversion

Recent decays, organic-inorganic hybrid materials has attarcted large attention as it can combine the advantageous characteristics of crystalline inorganic semiconductors with processability of organic materials. In particular, hybrid semiconductor nanocrystals (NCs) and conjugated dye molecules outstand as a candidate to form materials for triplet sensitzation. Triplet sensitization is an essential step in photon upconversion[8], photoredox catalysis[9], phototherapy[10] and photoimaging. In comparison to organic sensitizers, semiconductor NCs have a number of advantages such as high photostability, broad spectral range of light absorption, and size-tunable bandgap. An atomic and molecular understanding of the organic-inorganic interface is critical in enhancing electronic communication between the various components.

Our focus is on the hybrid photon upconversion system, specifically on how molecular orientation and orbital overlap affects triplet energy transfer (TET) from NC donor to anthracene transmitter. We are interested in the effect of isomeric substitutions on the transmitter for triplet energy transfer (TET) between nanocrystal (NC) donor and molecular acceptor. Each isomeric acceptor is expected to bind in a unique orientation with respect to the NC donor. We see that this orbital overlap drastically affects the transmission of triplets. Here, two functional groups, the carboxylic acid and dithiocarbamate, were varied between the 1-, 2- and 9- positions of the anthracene ring to give three ACA and three ADTC isomers. These six anthracene isomers served as transmitters for triplets between CdSe NC sensitizers and 9, 10-diphenylanthracene annihilators for photon upconversion. The photon upconversion quantum yield (QY) is the highest for 9-ACA (12%), lowest for 9-ADTC (0.1%), around 3% for both 1-ACA and 1-ADTC, and about 1 % for the 2-isomers. These trends in QYs are reflected in the rates of TET given by ultrafast transient absorption spectroscopy where a maximum of 3.8 x107 s-1 for 9-ACA was measured. Molecular excited state energy levels were measured both in solution and polymer hosts to correlate structure to TET. This work confirms that anthracene excited states levels are very sensitive to molecular substitution, which in combination with orbital overlap, critically affect Dexter-based TET.

In Fig.1.1 (a), hybrid inorganic CdSe nanocrystals and organic anthracene carboxylic acid (ACA) or dithiocarbamate (ADTC) as organic ligands on NCs surface severs as photon upconversion platform to upconvert low energy photons to high energy photons. How the orbital overlap of NCs and surface ligands and the affect triplet energy transfer from NCs to anthracene derivatives are investigated. Our research confirms that small perturbations to molecular structure can drastically realign the relative levels of excited states, thus impacting TET transfer in this hybrid platform.

1.3 Applying nontoxic silicon nanocrystals in photon upconversion process

In recent years, inorganic semiconductor nanocrystals (NCs) capable of strong and broad-band light absorption that is also facilely tunable from ultraviolet to infrared via NC sizes and compositions, interfaced with spin-triplet exciton accepting organic molecules have emerged as promising materials for converting incoherent long-wavelength light into the visible range.[8, 11] However, these materials to date have made exclusive use of NCs containing toxic elements, precluding their use for biological or environmentally-sensitive applications. We address this challenge by chemically functionalizing non-toxic silicon NCs with triplet-accepting anthracene ligands. Photoexciting these structures drives spin-triplet exciton transfer from silicon to anthracene via a single 15 ns Dexter energy transfer step with nearly 50% yield. When paired with 9,10-diphenylanthracene emitters, these particles readily upconvert 488 –

640 nm photons to 425 nm violet light with efficiencies as high as 7 ± 0.9% and can be readily incorporated into aqueous micelles for biological use.

This is the first time nontoxic indirect bandgap silicon nanocrystals being involved in triplet sensitization process. In Fig.1.1 b), silicon nanocrystals with octadecene as capping ligands and 9 ethyl anthracene as transmitter is excited with incident light, 488nm or 532nm, 640 nm and then energy transfer from NCs to transmitter and then emitter in solitons to fuse triplet to emit higher energy photons. Our demonstration of spin-triplet exciton transfer from silicon to molecular triplet acceptors can critically enable new technologies for solar energy conversion, quantum information, and near-infrared driven photocatalysis.

1.4 Tuning energy levels of PbS QDs to arrange band alignment

Capable bulk synthesis[12] near-infrared PbS QDs with earth-abundant elements have attracted greatly attention as promising candidates for photovoltaic applications because of a tunable energy bandgap that covers the optimal bandgap range for single and multi-junction solar cells1. The ability to tune device architecture via controlling the energy levels in semiconductor nanocrystals or QDs is crucible for high performing and cost-effective photovoltaic cells.[12] Shift band offsets of semiconductor nanocrystals is more difficult although a lot of synthetic methods could tune band gap of semiconductor NCs via controlling size and shape. conventional doping by introducing impurity atoms fail so far especially at the high temperatures necessary for synthesis as impurities tend to be expelled from the high crystalline nanocrystals.[13] While transition metal ions like Mn^{2+} have been successfully incorporated into the QD lattice, there is little perturbation to the band offsets.[14] The ability to adjust QD energy levels with the different ligand treatments potentially provides an inexpensive way to increase the depletion layer in QD solar cells. A depletion layer on the order of the absorption depth would improve charge extraction and ultimately increase the power conversion efficiency.[15-19] Fully fluorinated perfluorocarbon ligands are shown to modify the energetics and dielectric environment of quantum dots (QDs), resulting in a large hypsochromic shift in the optical gap. The original oleic acid (OA) ligands on PbS QDs can be completely replaced with thiolate and carboxylate-based perfluorocarbons, e.g. $-SCF_3$ and $CF_3(CF_2)_{14}COOH$ (pFA), respectively. Cyclic voltammetry confirms that the increase in electronegativity from the surface ligand combination of OA: pFA ~ 2:1 decreases the PbS QD band edge by 0.18 eV. The diminished reduction potential of the conduction band is confirmed by photo-induced electron transfer (PET) experiments. In contrast, the short thiolate ligands, $-SCF_3$ and $-SCH_3$, increase the donating ability of PbS QDs up to 7 times due to an increase in the permeability of the ligand shell. This work shows that electron-withdrawing halogens like fluorine and chlorine can control the bandgap and band offsets of nanocrystals for the future design and optimization of functional organic/inorganic hybrid nanostructures.

1.5 Modify surface of PbS QDs to build superlattice film for charge transfer

Generally, self-assembly of QDs is limited to insulating but ordered thin films, or disordered thin films. It is difficult to observe coherent electronic coupling in QD thin films because it is usually inhibited by disorder and/or prohibitively large interparticle distances. This stems from the prevailing methods of making QD thin films. Firstly, superlattices of QDs are generally assembled from QDs with long chain insulating ligands, [20-24] [20-24] [20-24]like oleic or octadecylphosphonic acid, whi4ch are close to 2 nm in length. This results in QDs that are too far apart for effective charge transfer. Secondly, thin films of QDs, e.g. those used in solar cells, are disordered because cross-linking occurs in a layer-by-layer fashion with no control over the order within or between nanoparticle layers.[25] Typically, thin films of QDs for photovoltaics are covalently held together by the displacement of existing insulating ligands with hydrazine or dithiols, by alternate exposure to individual solutions of QDs and cross-linking agents. The resulting covalent attachment of new QDs to existing layers is random, and cracks in the film develop as it contracts in arbitrary directions. A hybrid of these two methods has been attempted without achieving long-range order. For example, insulating superlattices of QDs have been backfilled with metal chalcogenide complexes (MCCs). [26, 27] This improved the electrical conductivity of the thin film but compromised the order within the film. [28, 29] Other examples of long-range order include the assembly of FePt, Au and PbS nanoparticles (NPs) at a liquid-air interface[30, 31]by Miliron and co-workers, and the assembly of gold NPs functionalized with tin-sulfide complexes.[32] While the metal nanoparticles showed increased conductance possibly due to improved film connectivity, the PbS thin film exhibited poor electronic properties. The poor mobility most likely arose from the surface defects introduced by the liquid layer in the self-assembly process. From these examples, it remains a challenge to induce long-range order while maintaining good electronic properties.

Thus, we explore the effect of a trifluoromethyl coating on lead sulfide quantum dots (PbS QDs) in thin film transistor (TFT) geometry. The low surface energy conferred by the oleophobic perfluorocarbons creates QDs packed in a primitive cubic lattice with long range order, as confirmed by grazing incidence small angle x-ray scattering (GISAXS) and transmission electron microscopy (TEM). Hole mobilities as high as 0.085 cm^2/ Vs were measured in the TFTs. No electron transport indicates that the electron-withdrawing nature of the trifluoromethyl ligand is eclipsed by the excess holes present in the PbS QDs, that likely stem from cation vacancies.

1.6 Notes and References

1. Konstantatos G, *et al.* Ultrasensitive solution-cast quantum dot photodetectors. *Nature* 2006, 442(7099): 180-183.

2. Steckel JS, *et al.* 1.3 µm to 1.55 µm Tunable Electroluminescence from PbSe Quantum Dots Embedded within an Organic Device. *Adv, Mater* 2003, 15(21): 1862-1866.

3. Pan Y, *et al.* Near-infrared upconversion-activated CRISPR-Cas9 system: A remote-controlled gene editing platform. *Sci Adv* 2019, 5(4): eaav7199.

4. Chen S, *et al.* Near-infrared deep brain stimulation via upconversion nanoparticle–mediated optogenetics. 2018, 359(6376): 679-684.

5. Owen JS, *et al.* Reaction Chemistry and Ligand Exchange at Cadmium−Selenide Nanocrystal Surfaces. *J Am Chem Soc* . 2008, 130(37): 12279-12281.

6. Brutchey R, *et al.* Surface Chemistry of Colloidal Semiconductor Nanocrystals: Organic, Inorganic, and Hybrid. In: B. Charleux CCaEL (ed). *Chemistry of Organo-Hybrids*, 2015, pp 233-271.

7. Rigsby EM, *et al.* Primary amines enhance triplet energy transfer from both the band edge and trap state from CdSe nanocrystals. *J. Chem. Phy* 2019, 151(17): 174701.

8. Huang Z, *et al.* Hybrid Molecule-Nanocrystal Photon Upconversion Across the Visible and Near-Infrared. *Nano Letters* 2015, 15(8): 5552-5557.

9. Ravetz BD, *et al.* Photoredox catalysis using infrared light via triplet fusion upconversion. *Nature* 2019, 565(7739): 343-346.

10. Heo JH, *et al.* Hysteresis-less inverted CH3NH3PbI3 planar perovskite hybrid solar cells with 18.1% power conversion efficiency. *Energy Environ Sci* 2015, 8(5): 1602-1608.

11. Huang Z, *et al.* Ligand enhanced upconversion of near-infrared photons with nanocrystal light absorbers. *Chem Sci* 2016, 7(7): 4101-4104.

12. Chuang C-HM, *et al.* Improved performance and stability in quantum dot solar cells through band alignment engineering. *Nat Mater* 2014, 13(8): 796-801.

13. Mikulec FV, *et al.* Organometallic Synthesis and Spectroscopic Characterization of Manganese-Doped CdSe Nanocrystals. *J Am Chem Soc* 2000, 122(11): 2532-2540.

14. Nag A, *et al.* Metal-free Inorganic Ligands for Colloidal Nanocrystals: S2–, HS–, Se2–, HSe–, Te2–, HTe–, TeS32–, OH–, and NH2– as Surface Ligands. *J Am Chem Soc* 2011, 133(27): 10612-10620.

15. Kramer IJ, *et al.* The Architecture of Colloidal Quantum Dot Solar Cells: Materials to Devices. *Chem Rev* 2014, 114(1): 863-882.

16. Greaney MJ, *et al.* Improving Open Circuit Potential in Hybrid P3HT:CdSe Bulk Heterojunction Solar Cells via Colloidal tert-Butylthiol Ligand Exchange. *ACS Nano* 2012, 6(5): 4222-4230.

17. Yaacobi-Gross N, *et al.* Molecular control of quantum-dot internal electric field and its application to CdSe-based solar cells. *Nat Mater* 2011, 10: 974.

18. Lazarenkova OL, *et al.* Miniband formation in a quantum dot crystal. *J Appl Phys* 2001, 89(10): 5509-5515.

19. Lazarenkova OL, *et al.* Electron and phonon energy spectra in a three-dimensional regimented quantum dot superlattice. *Phys Rev B* 2002, 66(24): 9.

20. Whitham K, *et al.* Entropic, Enthalpic, and Kinetic Aspects of Interfacial Nanocrystal Superlattice Assembly and Attachment. *Chem Mater* 2018, 30(1): 54-63.

21. Weidman MC, *et al.* Impact of Size Dispersity, Ligand Coverage, and Ligand Length on the Structure of PbS Nanocrystal Superlattices. *Chem Mater* 2018, 30(3): 807-816.

22. Kovalenko MV, *et al.* Nanocrystal superlattices with thermally degradable hybrid inorganic-organic capping ligands. *J Am Chem Soc* 2010, 132(43): 15124-15126.

23. Tang J, *et al.* Colloidal-quantum-dot photovoltaics using atomic-ligand passivation. *Nat Mater* 2011, 10(10): 765-771.

24. Nag A, *et al.* Metal-free Inorganic Ligands for Colloidal Nanocrystals: S2-, HS-, Se2-, HSe-, Te2-, HTe-, TeS32-, OH-, and NH2- as Surface Ligands. *J Am Chem Soc* 2011, 133(27): 10612-10620.

25. Kovalenko MV, *et al.* Colloidal nanocrystals with molecular metal chalcogenide surface ligands. *Science* 2009, 324(5933): 1417-1420.

26. Jang J, *et al.* Temperature-Dependent Hall and Field-Effect Mobility in Strongly Coupled All-Inorganic Nanocrystal Arrays. *Nano Lett* 2014, 14(2): 653-662.

27. Lee J-S, *et al.* Band-like transport, high electron mobility and high photoconductivity in all-inorganic nanocrystal arrays. *Nat Nanotechnol* 2011, 6(6): 348-352.

28. Tangirala R, *et al.* Modular inorganic nanocomposites by conversion of nanocrystal superlattices. *Angew Chem Int Ed Engl* 2010, 49(16): 2878-2882.

29. Dong A, *et al.* Electronically Coupled Nanocrystal Super lattice Films by in Situ Ligand Exchange at the Liquid-Air Interface. *Acs Nano* 2013, 7(12): 10978-10984.

30. Kovalenko MV, *et al*. Expanding the Chemical Versatility of Colloidal Nanocrystals Capped with Molecular Metal Chalcogenide Ligands. *J Am Chem Soc* 2010, 132(29): 10085-10092.

31. Xing G, *et al*. Long-range balanced electron-and hole-transport lengths in organic-inorganic CH3NH3PbI3. *Science* 2013, 342(6156): 344-347.

32. Stranks SD, *et al*. Electron-hole diffusion lengths exceeding 1 micrometer in an organometal trihalide perovskite absorber. *Science* 2013, 342(6156): 341-344.

2 Chapter 2. On the efficacy of anthracene isomers for triplet transmission from CdSe nanocrystals

2.1 Introduction

Hybrid materials made of organic and inorganic components may deliver synergies in charge or energy transfer. This is seen in perovskite and dye-sensitized solar cells (DSSCs). Perovskite solar cells have inherently long charge carrier diffusion lengths,[1, 2] resulting in an unrivalled trajectory in their power conversion efficiencies,[3, 4] especially when compared to other thin-film alternatives. DSSCs combine mesoporous titania with bound organo-metallic compounds to efficiently convert photons into current.[5-7] In terms of energy transfer, semiconductor nanocrystals (NCs), in conjunction with acene derivatives, have been demonstrated to upconvert light incident at solar fluxes effectively.[8-13] In all these hybrid systems, an atomic and molecular understanding of the organic-inorganic interface is critical in enhancing electronic communication between the various components. Investigation of the mechanism and factors affecting energy conversion are key to designing efficient solar light harvesting and converting structures. In fact, for the DSSCs, it has been shown that the conjugated backbone, functional group, metal center, etc. of the dye can drastically affect electron transfer to the titania photoanode.[14-17]

With this in mind, it is clear that similar considerations must apply to all hybrid platforms. Here, the focus is on a hybrid photon upconversion system, specifically on how molecular orientation and orbital overlap affects triplet energy transfer (TET) from NC donor to anthracene transmitter. We investigate the electronic communication between different isomers of anthracene transmitter ligands covalently bound to CdSe NCs, especially because excited states are very sensitive to environmental factors and molecular substitutions in anthracene.[18-20] Electronic communication is evaluated with two independent and complementary methods, transient absorption (TA) measurements and continuous wave (cw) photon upconversion experiments. This was motivated by our earlier observation that the 1-, 2- and 9- anthracene carboxylic acid (ACA) transmitter ligands gave noticeably different upconversion QYs for the conversion of green to violet light[8]. Using TA spectroscopy, we find that 9-ACA transmits triplets at rates two orders of magnitude higher than 1- and 2- ACA, giving the highest upconversion QY of 12%, while the 9-anthracene dithiocarbamate (9-ADTC) quenches the CdSe 100x faster than the 1- and 2-ADTC with a low upconversion QY of 0.1%. The 9-isomers effect energy or charge transfer at rates on the order of 10^7 s^{-1}, while the 2-isomers and 1-isomers have upconverison QYs of 1 % and 3% respectively with rates of TET around 10^5 s^{-1}. We hypothesize that the low upconversion QY for 9-ADTC may be due to the intramolecular charge transfer states which are reflected in the inherently low fluorescence QY of these dithiocarbamate (DTC) containing ligands.

2.2 Results and Discussion

Six different anthracene transmitter ligands were used in this study. They consist of anthracene substituted with either carboxylic acid or dithiocarbamate at the 1-, 2- or 9- positions of the conjugated ring (Fig. 2.1). These functional groups bind the anthracene moiety onto the surface of 2.39 nm diameter(half width at half maximum of the first exciton absorption is 14 nm) wurtzite octadecylphosphonic acid (ODPA) functionalized CdSeNCs CdSe/ODPA). In this hybrid organic-inorganic upconversion system, energy is transferred from the CdSe NCs (sensitizer) to the triplet state of the transmitter down an energy cascade to the 9, 10-diphenylanthracene (DPA) annihilator. Two DPA molecules in their triplet excited states collide with each other and undergo triplet-triplet annihilation (TTA) to emit a photon higher in energy than the incident light. Fig. 2.1 b) shows the electronic absorption and fluorescence spectra of the ACA and ADTC isomers in anhydrous THF at RT. Details are listed in Table 7.1. Comparing the emission of 1-ADTC, 9-ADTC and 2-ACA, the red-shifted, broad emission of 2-ADTC, 1-ACA and 9-ACA (λ_{ex} = 350 nm) with little vibrational fine structure is consistent with the functional group being coplanar with the anthracene ring, as described by Werner and Hercules, and later by Ghoneim.[21,] This bathochromic shift is solvent dependent. While the ACA isomers are commercially available, the ADTC isomers were synthesized in two steps (see Scheme 7.1). In comparison with the carboxylic acid, the dithiocarbamate functional group was expected to lower the tunnelling barrier for energy transfer across the NC- transmitter interface with the formation of a more covalent bond.[22] However, since the Weiss group showed that phenyl dithiocarbamates delocalize the CdSe excitonic hole onto the ligands,[23] charge transfer states stemming from interaction of the conjugated core with the DTC functional group could also inhibit TET across this interface.[22]

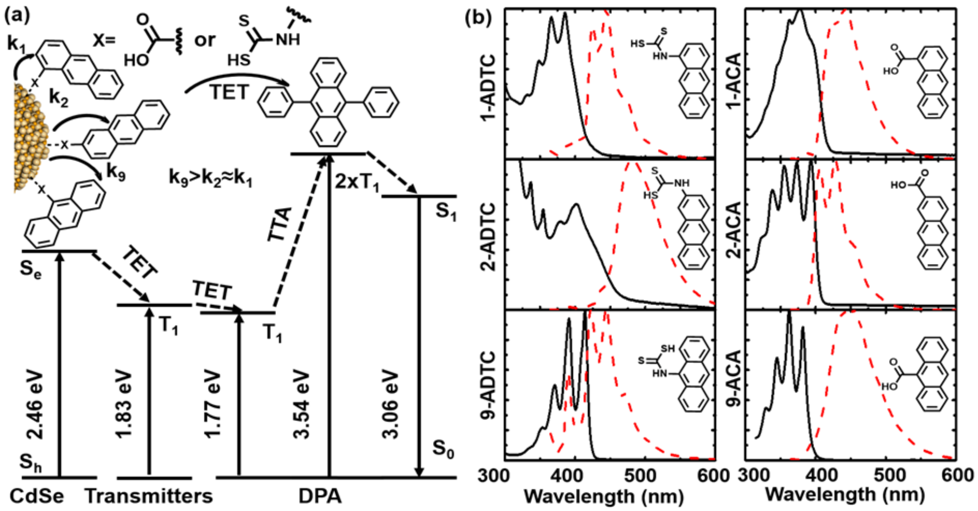

Fig. 2.1 (a) Schematic of the energy transfer in this hybrid photon upconversion system, with 2.39 nm diameter CdSe nanocrystals (NCs) as sensitizer and DPA as annihilator. Isomeric anthracene derivatives functionalized with carboxylic acid and dithiocarbamate binding groups at the 1-, 2- and 9- positions on the aromatic ring serve as transmitter ligands with different rates of triplet energy transfer for each isomer (k_1, k_2 and k_9 respectively). (b) Emission (dash line) and absorption (solid line) spectra of 1-ACA, 2-ACA, 9-ACA, 1-ADTC, 2-ADTC and 9-ADTC ligands in tetrahydrofuran at RT.

The ADTC isomers bind more strongly to the ODPA-coated CdSe NCs (CdSe/ADTC) than their ACA counterparts (CdSe/ACA). Using UV-Vis electronic absorption spectroscopy, we have shown there are an average of three 9-ACA transmitter ligands bound per CdSe NC. For the ADTC transmitters, 3 to 15 ligands are bound per NC (Fig. 7.1) even though the ratio of ADTC per NC is lower during ligand exchange. In contrast, for the ACA isomers, N, the average number of bound transmitter ligands per NC, is 2- 6 even when the transmitter concentration is 10 times higher and ligand exchange time longer, up to 12 hours.

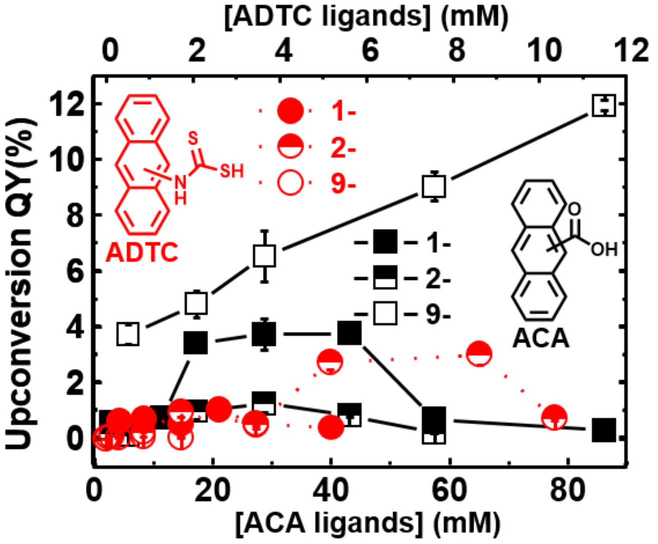

Fig. 2.2 the relationship between upconversion QY (%) and the transmitter concentration of ACA isomers (squares) and ADTC (circles) exchange. All upconversion samples were air-free in hexane with DPA annihilator concentration of 2.15 mM, excited with 12.7 W/cm^2 532 nm or 488 nm cw lasers at RT.

Table 2.1 Maximum upconversion QY (%) and N, the average number of bound ACA and ADTC transmitter ligands per CdSe NC. <τ>, the average lifetime and <k>, the average rates of energy transfer were obtained from fitting a stretched exponential to the kinetic decays at 505 nm in the transient absorption spectra.

Transmitter		Upconversion QY(%)	N	<τ>/ ns	<k> ×10^7 /s^{-1}
No transmitter		0.025[12]	0	39.9	-
ADTC isomer	1-	3.0±0.4	6	39.7	0.075
	2-	1.1±0.1	2	39.9	0.063
	9-	0.1 ±0.0	1	19.5	2.7
ACA isomer	1-	3.8 ±0.4	3	39.7	0.077
	2-	1.2 ±0.3	2	39.9	0.063
	9-	11.9 ±0.2	4	16.0	3.8

In general, anthracene transmitters functionalized at the 1- position are more effective compared to the 2- position in mediating energy transfer. This can be seen in Table 2.1 Maximum upconversion QY (%) and N, the average number of bound ACA and ADTC transmitter ligands per CdSe NC. <τ>, the average lifetime and <k>, the average rates of energy transfer were obtained from fitting a stretched exponential to the kinetic decays at 505 nm in the transient absorption spectra.and Fig. 2.2, where CdSe/1-ADTC and CdSe/1-ACA complexes give upconversion QYs of ~3%, compared to CdSe/2-ADTC and CdSe/2-ACA NCs which result in upconversion QYs ~1%. Fig. 2.2 shows that the decrease in the upconversion QY after a certain optimal ligand loading may be due to TTA between surface bound transimtters. Table 1 lists the maximum upconversion QYs for each transmitter ligand and the corresponding surface coverage. CdSe/9-ACA NCs shows the highest upconversion QY at around 12%, approximately 10 times higher than CdSe/2-ACA, while the CdSe/9-ADTC NCs have the lowest upconversion QY at 0.1%. Details of the ligand exchange procedure and characterization, including the average number of bound ligands per NC, N, are in the chapter 7.

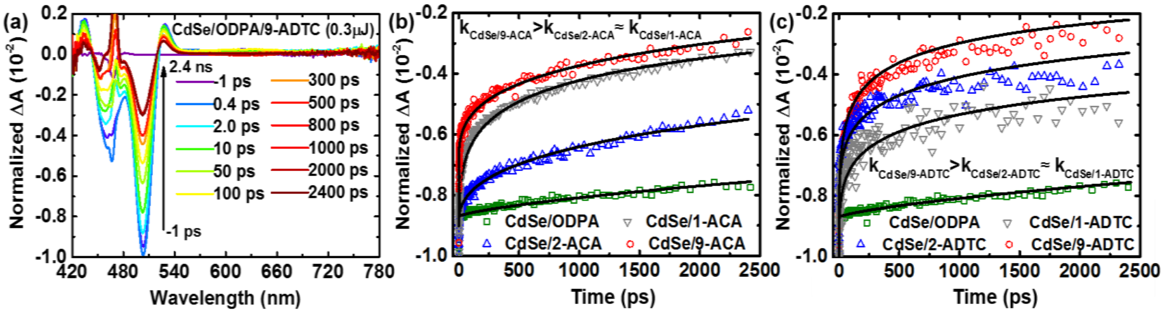

Fig. 2.3 (a) Ultrafast TA spectra of CdSe/ 9-ADTC (16.6 µM) using 465 nm pulsed laser excitation (0.3 µJ per pulse, > 30 fs full width at half maximum) in toluene at RT. Experimental decays from 1 picoseconds (ps) before excitation (violet) to 2.4 ns after excitation (red) is shown. (b) and (c) The ground state recovery of CdSe NCs investigated by its kinetics at 505nm, highlighting much faster quenching of its first excitonic state in the presence of transmitter ligands. Native CdSe/ODPA (green square) (b) CdSe/ACA: 1-ACA (grey triangle), 2-ACA (blue triangle) and 9-ACA (red circle); and (c) CdSe/ADTC: 1-ADTC (grey triangle), 2-ADTC (blue triangle) and 9-ADTC (red circle). The black solid line is the fit.

The appearance of the triplet excited states of anthracene (~433 nm) in the CdSe/ transmitter complexes in ultrafast TA experiments confirm direct TET from CdSe NCs to surface-anchored ligands, as seen in the report by Castellano et al.[12] To aviod multi-exciton annihilation, the pump power was kept at 0.3 μJ (> 30 fs full width at half maximum). TA spectra was acquired for up to 2.4 ns for each optimized CdSe/ transmitter complex with the highest upconversion QY. The decay of the first excited state of CdSe NCs coincided with the growth of an absorption peak located at 433 nm, which is the T_1 to T_n transition of anthracene. There were no transient signals corresponding to singlet states of these ligands, nor their radical cations or anions. Fig. 2.3a shows the TA spectra of CdSe/9-ADTC changing with time as an example. The TA spectra for the other five CdSe/ transmitter complexes are in Fig. 7.9. Transient kinetics of the ground state recovery of CdSe NC reveals the rate of TET from CdSe NCs is higher for the 9-ACA transmitter compared to the 1- and 2- isomers. Kinetics were monitored around the first exciton absorption, reflecting the generation of anthracene triplets. An empirical stretching exponential (eq. 7.7) was used to model the dynamics of interfacial TET and the ground state recovery of CdSe NCs (eq. 7.8 to eq. 7.9) and fitting values are listed in Table 7.9.[12] As shown in eq. 7.9 and Table 2.1, we calculate the average rate of energy transfer, <k>, with parameters from the fits, showing that CdSe/9-isomers have the highest energy transfer rate, an order of magnitude higher than CdSe/1- and CdSe/2-isomers. For example, $\langle k_{9\text{-ACA}} \rangle$ and $\langle k_{9\text{-ADTC}} \rangle$ are 3.8×10^7 and 2.7×10^7 s^{-1} respectively, while the corresponding rate for the other isomers range from 2.7×10^5 to 6.5×10^5 s^{-1}. This makes sense for 9-ACA because this transmitter always gives an upconversion QY exceeding 10%, while the upconversion QY for the 1- and 2- transmitters is between 1-3%. The measured $\langle k_{9\text{-ACA}} \rangle$, 3.8×10^7 s^{-1} (Table 2.1), is in agreement with the value reported by Bardeen,[12] $1.5\text{x}10^7$ s^{-1}, obtained from time resolved photoluminescence spectroscopy (TRPL), and also in agreement with Li et al's $1.0\text{x}10^7 s^{-1}$ rate.[12] However, $\langle k_{9\text{-ACA}} \rangle$ here is two orders of magnitude lower than the $3\text{x}10^9$ s^{-1} from Castellano's work[12], perhaps because they treated their CdSe/ ODPA NCs with oleic acid before ligand exchange, resulting in an average of 12 ligands per CdSe NC, N =3 for CdSe/9-ACA here.

We hypothesize that the discrepancy between the fast recovery of the exciton bleach for the CdSe/ 9-ADTC NCs, $<k_{9\text{-ADTC}}>$, and its low upconversion QY is related to the fast quenching of the excited state. This is reflected in the low fluorescence QY of 9-ADTC (0.05%), which indicates intersystem crossing (ISC), internal conversion and other nonradiative decay pathways such as the nπ* transitions from the lone pair on the nitrogen atom of the DTC group to the anti-bonding orbital on the anthracene ring are dominant. The fluorescence QY of six isomers in THF under N_2 atmosphere at RT are shown in Fig. 2.4a and Table 7.1. We found that the ACA isomers have a much higher fluorescence QY (0.2 - 0.4), compared to 0.0005 - 0.012 of the ADTC isomers. In THF, the 2-isomers have the highest fluorescence QY for both ACA and ADTC isomers. We also considered hole transfer as a possible reason for the low upconversion QY for the CdSe/9-ADTC NCs, especially since Weiss et al recently reported enhanced hole transfer from CdSe NCs to phenothiazine when covalently linked by phenyl dithiocarbamate.[24] To investigate if this process was thermodynamically feasible, we used cyclic voltammetry (CV) to measure the HOMO and LUMO of 9-ACA and 9-ADTC (Fig. 7.22). The molecular orbital levels are depicted in Fig. 2.4 b with the conduction and valance band of CdSe NCs[27]. From the energy diagram, hole transfer from CdSe NCs to bound ACA or ADTC isomers is possible, though there is not a large thermodynamic driving force. Conversely, electron transfer from ligands to CdSe QDs is also possible. However, there is no evidence of radical cation or radical anion formation for CdSe/1-, 2- and 9-ADTC complexes as there are no changes in the kinetic traces extracted from our TA spectra at 629 nm, 681 nm and 748 nm (anthracene radical cation[9]), or 452 nm, 596 nm and 732 nm (anthracene radical anion[25]). In addition, unlike the Weiss group, we did not observe a red shift in the absorption spectrum of the CdSe NCs after ligand exchange with the ADTC isomers, further discounting hole delocalization.

The larger <k_i>measured for the 9-isomers implies they are more effective transmitters. The 9-isomers may bind selectively to unique facets on the CdSe NC distinct from that for the 1- and 2- isomers. This might affect the electronic coupling with the NC, critical to efficient Dexter energy transfer across the molecular-nanocrystal interface[26]. The average number of bound ligands per CdSe, N, has a maximum value when functionalized with the 1- or 2- isomers, while N continuously increases with the 9- isomers as a function of transmitter concentration in Fig. 7.1. This qualitative difference indicates that molecular geometry might affect binding affinity, especially since anisotropic wurtzite CdSe NCs are employed here. In principle, these NCs have Cd^{2+} and Se^{2-} rich facets on opposing ends of the wurtzite c-axis, and Guyot-Sionnest has reported that 2.7 nm wurtzite CdSe/ ODPA NCs have a dipole moment of 40 Debye. Anisotropy not-withstanding, zinc blende CdSe NCs also have a permanent dipole, perhaps due to surface charges.[27]

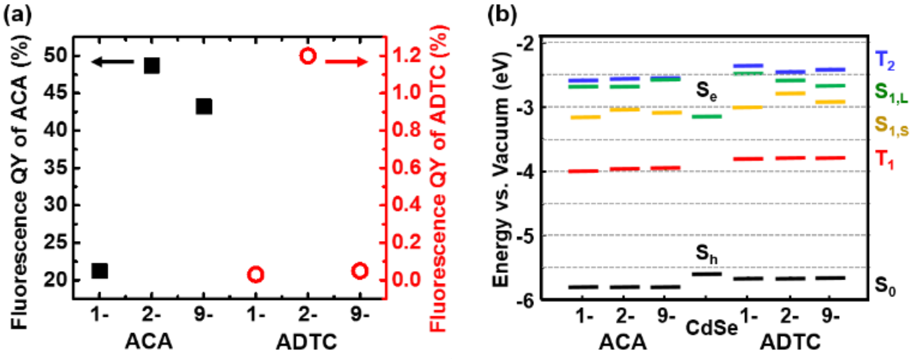

Fig. 2.4 (a) Fluorescence QY (%)of ACA (black square) and ADTC (red circle) isomers in anhydrous THF at RT. (b) Band offsets for CdSe NCs (diameter, d = 2.4 nm)[27] The HOMOs of ACA and ADTC were measured by cyclic voltammetry (CV) in dichloromethane. The first excited singlet state in THF and 4-Bromopolystyrene (4-BrPS) is denoted as S$_{1,\ L}$ and S$_{1,s}$ respectively. The first and second triplet excited state, T$_1$ and T$_2$ were measured from isolated anthracene molecules dispersed in 4-BrPS at RT.

The dielectric environment of the anthracene transmitter will affect its excited state energy levels, while its orientation with respect to the NC surface will affect the electronic coupling. For example, in isolated anthracene molecules, the T_2 state is below the S_1 state, resulting in efficient ISC and a low fluorescence QY. However, the relative energy values of these two states are reversed in crystalline anthracene, with T_2 being 73 meV higher in energy than the S_1, thus decreasing the rate of ISC.[27] In another example, for the single perylene diimide (PDI) molecule, the yield of triplets is less than 1%, but a cofacially stacked PDI-dimer forms an excimer with up to 50% yield of triplets from the initial excitations.[28] While it would be ideal to characterize the tilt angle or symmetry in the binding of the anthracene transmitter ligand to the NC surface, it is experimentally challenging to do so- the use of infrared spectroscopy to measure binding modes was inconclusive. Instead, we have measured the first and second triplet excited state levels (T_1 and T_2 respectively) of isolated anthracene transmitters embedded in 4-bromopolystyrene (4-BrPS).[29] As shown Fig. 2.4b, the T_1 to S_0 states cluster around 1.83 eV, while the T_2 to T_1 states are around 1.40 eV, in line with excited states of anthracene in poly (methyl methacrylate). Values are shown in Table 7.2.

2.3 Conclusion

The kinetic traces from the TA data shows that the 9-isomers, regardless of functional group, have the highest rate of TET or charge transfer from CdSe NCs to anthracene. TA experiments confirm that the 1-isomers have a higher rate of TET compared to the 2-isomers, which is reflected in the 3% photon upconversion QYs for the former compared to 1% for the latter. Though the DTC functional group has a higher binding affinity for the CdSe donors, the 9-ACA transmitter outperforms the 9-ADTC by more than two orders of magnitude in terms of photon upconversion. While prior work suggests the poor performance of 9-ADTC is due to charge transfer to sulphur containing ligands from the NC, it could also stem from the fast non-radiative processes inherent in the DTC family that quench molecular excited states particularly when the acid group is in the 9-position. This study shows that molecular orientation greatly affects TET, most likely by affecting orbital overlap between the NC donor and anthracene acceptor. It confirms that small perturbations to molecular structure can drastically realign the relative levels of excited states, thus impacting TET transfer in this hybrid platform.

2.4 Notes and References

1.Olshansky JH, et al. Hole transfer from photoexcited quantum dots: The relationship between driving force and rate. *J Am Chem Soc* 2015, 137(49): 15567-15575.

2.Xing G, et al. Long-range balanced electron-and hole-transport lengths in organic-inorganic CH3NH3PbI3. *Science* 2013, 342(6156): 344-347.

3.Stranks SD, et al. Electron-hole diffusion lengths exceeding 1 micrometer in an organometal trihalide perovskite absorber. *Science* 2013, 342(6156): 341-344.

4.Heo JH, et al. Hysteresis-less inverted CH 3 NH 3 PbI 3 planar perovskite hybrid solar cells with 18.1% power conversion efficiency. *Energy Environ Sci* 2015, 8(5): 1602-1608.

5.Burschka J, et al. Sequential deposition as a route to high-performance perovskite-sensitized solar cells. *Nature* 2013, 499(7458): 316-319.

6.O’regan B, et al. Low cost and highly efficient solar cells based on the sensitization of colloidal titanium dioxide. *Nature* 1991, 335(24): 737-740.

7.Kavan L, et al. Electrochemical and photoelectrochemical investigation of single-crystal anatase. *J Am Chem Soc* 1996, 118(28): 6716-6723.

8.Grätzel M. Photoelectrochemical cells. *Nature* 2001, 414(6861): 338-344.

9.Huang Z, et al. Hybrid molecule–nanocrystal photon upconversion across the visible and near-infrared. *Nano Lett* 2015, 15(8): 5552-5557.

10.Li X, et al. Distance-Dependent Triplet Energy Transfer between CdSe Nanocrystals and Surface Bound Anthracene. *J Phys Chem Lett* 2016, 7(11): 1955-1959.

11.Piland GB, et al. Dynamics of Energy Transfer from CdSe Nanocrystals to Triplet States of Anthracene Ligand Molecules. *J Phys Chem C* 2016, 120(11): 5883-5889.

12.Mahboub M, et al. Triplet Energy Transfer from PbS (Se) Nanocrystals to Rubrene: the Relationship between the Upconversion Quantum Yield and Size. *Adv Funct Mater* 2016, 26(33): 6091-6097.

13.Mongin C, et al. Direct observation of triplet energy transfer from semiconductor nanocrystals. *Science* 2016, 351(6271): 369-372.

14.Wu M, et al. Solid-state infrared-to-visible upconversion sensitized by colloidal nanocrystals. *Nat Photon* 2016, 10(1): 31-34.

15.Hagfeldt A, et al. Dye-sensitized solar cells. *Chem Rev* 2010, 110(11): 6595-6663.

16.Grätzel M. Dye-sensitized solar cells. J Photochem Photobiol, C 2003, 4(2): 145-153.

17.Qin P, et al. Influence of π-conjugation units in organic dyes for dye-sensitized solar cells. *J Phys Chem C* 2007, 111(4): 1853-1860.

18.Koumura N, et al. Alkyl-functionalized organic dyes for efficient molecular photovoltaics. *J Am Chem Soc* 2006, 128(44): 14256-14257.

19.Kearvell A, et al. Fluorescence quenching and external spin-orbit coupling effects. *Molecular Crystals 1968*, 4(1-4): 69-81.

20.Kearvell A, et al. Transitions Non-Radiatives dans les Molecules. J Chim Phys(Paris, 1969) 1969: 125.

21.Turro NJ, et al. Modern molecular photochemistry of organic molecules. University *Science* Books Sausalito, California, 2010.

22.Werner TC, et al. Fluorescence Of 9-Anthroic Acid and its Esters. Environmental Effects On Excited-State Behavior. *J Phys Chem* 1969, 73(6): 2005-&.

23.Ghoneim N, et al. Dual Luminescence, Structure and Excimers of 9-Anthracene Carboxylic-Acid. *J Lumin* 1993, 55(5-6): 271-275.

24.Hong C, et al. Novel aromatic–polyamine conjugates as cholinesterase inhibitors with notable selectivity toward butyrylcholinesterase. *Biorg Med Chem* 2014, 22(12): 3213-3219.

25.Zhu J, et al. Design, synthesis, X-ray crystallographic analysis, and biological evaluation of thiazole derivatives as potent and selective inhibitors of human dihydroorotate Dehydrogenase. *J Med Chem* 2015, 58(3): 1123-1139.

26.Jia C, et al. Molecule-electrode interfaces in molecular electronic devices. *Chem Soc Rev* 2013, 42(13): 5642-5660.

27.Frederick MT, et al. Control of Exciton Confinement in Quantum Dot-Organic Complexes through Energetic Alignment of Interfacial Orbitals. *Nano Lett* 2013, 13(1): 287-292.

28.Lian S, et al. Subpicosecond Photoinduced Hole Transfer from a CdS Quantum Dot to a Molecular Acceptor Bound Through an Exciton-Delocalizing Ligand. *ACS Nano* 2016, 10(6): 6372-6382.

29.Masnovi J, et al. Electron transfer from anthracenes. Comparison of photoionization, charge-transfer excitation and electrochemical oxidation. Can J Chem 1984, 62(11): 2552-2559.

30.Pedersen SU, et al. New methods for the accurate determination of extinction and diffusion coefficients of aromatic and heteroaromatic radical anions in N, N-dimethylformamide. *J Electroanal Chem* 1998, 454(1): 123-143.

31.Shim M, et al. Permanent dipole moment and charges in colloidal semiconductor quantum dots. *J Chem Phys* 1999, 111(15): 6955-6964.

32.Stacy WT, et al. Temperature Dependence of Intersystem Crossing in Crystalline Anthracene. *J Chem Phys* 1970, 52(4): 1962-&.

33.Ford TA, et al. Enhanced triplet exciton generation in polyfluorene blends. *Phys Rev B* 2005, 71(12): 125212.

34.Reineke S, et al. Room temperature triplet state spectroscopy of organic semiconductors. *Sci Rep* 2014, 4: 3797.

35.Padhye MR, et al. Lowest triplet state of anthracene. *J Chem Phys* 1956, 24(3): 588-594.

3 Chapter 3. Achieving spin-triplet exciton transfer between silicon and molecular acceptors for photon upconversion

3.1 Introduction

Inorganic semiconductor nanocrystals (NCs) interfaced with spin-triplet exciton accepting organic molecules have emerged as promising materials for converting incoherent long-wavelength light into the visible range. However, these materials to date have made exclusive use of NCs containing toxic elements, precluding their use for biological or environmentally-sensitive applications. Here, we address this challenge by chemically functionalizing non-toxic silicon NCs with triplet-accepting anthracene ligands. Photoexciting these structures drives spin-triplet exciton transfer from silicon to anthracene via a single 15 ns Dexter energy transfer step with nearly 50% yield. When paired with 9,10-diphenylanthracene emitters, these particles readily upconvert 488 – 640 nm photons to 425 nm violet light with efficiencies as high as 7 ± 0.9% and can be readily incorporated into aqueous micelles for biological use. Our demonstration of spin-triplet exciton transfer from silicon to molecular triplet acceptors can critically enable new technologies for solar energy conversion, quantum information, and near-infrared driven photocatalysis.

Materials that convert infrared light into the visible range are desirable as they can enable advanced schemes for photocatalysts,[1] solar energy harvesting,[2] deep tissue imaging,[3] and phototherapy.[4] Inorganic nanocrystals (NCs) functionalized with energy-accepting dyes form a promising platform to meet this demand. These materials achieve light upconversion by using photons absorbed by the NC to excite spin-triplet excitons centered on organic molecules tethered to their surface.[5–7] Pairs of these excitons can merge via a process known as triplet fusion to produce high-energy spin-singlet states that emit visible light. While upconversion efficiencies >10% have been achieved by this approach,[8,9] these systems have exclusively employed NCs containing toxic heavy elements, such as cadmium or lead,[5,6,10] limiting their range of utility. Replacement of these NCs with nontoxic infrared absorbers is a key step in designing upconversion systems suitable for both biological and environmental applications. This issue makes silicon highly attractive for NC-based upconversion systems as it is earth-abundant and non-toxic. Methodologies exist for producing silicon nanocrystals (Si NCs) in large quantities[11,12] and synthetic approaches available for attaching ligands to their surfaces via strong covalent silicon-carbon bonds.[13] Moreover, tethering triplet-exciton accepting dyes to Si NCs is attractive not only for photon upconversion, but also for functional interfaces that extract spin-triplet excitons produced by singlet fission, triplet fusion's inverse. Singlet fission is highly efficient in a number of polycyclic aromatic hydrocarbon solids and molecular dimers[14–22] and pairing this process with inorganic semiconductors offers potential for photovoltaics that surpass the Shockley-Queisser limit[2,23,24] and quantum information devices that employ spin-entangled exciton pairs.[25] Due to its dominance within the semiconductor industry, silicon represents a natural material partner and recent work reported by Baldo and coworkers on tetracene:silicon junctions has shown spin-triplet exciton transfer from tetracene to silicon.[26] While promising, this study was unable to identify a triplet exciton transfer mechanism and noted the interfacial structure of the tetracene:silicon junction had to be carefully controlled to observe any energy transfer. In this respect, dye-functionalized Si NCs can greatly aid in optimizing organic:silicon junctions by allowing triplet energy transfer to be studied in the absence of complicating effects such as exciton diffusion to and from the interface.

3.2 Results and Dissuasion

Here, we demonstrate Si NCs produced via a non-thermal plasma synthesis can be readily functionalized with anthracene triplet acceptors to produce photon upconversion systems that convert 488 – 640 nm photons to 425 nm violet light with efficiencies as high as 7 ± 0.9% and saturation threshold intensities as low as 950 mW/cm^2. These materials can be readily incorporated into aqueous micelles for biological imaging and upconvert light even in the presence of oxygen to a limited degree. Using femtosecond transient absorption, we find Si-to-anthracene triplet energy transfer occurs via the concerted transfer of an electron and hole (Dexter energy transfer) over 15 ns, a rate comparable to that achieved with direct bandgap NC systems,[7,27,28] which we achieve through use of the short, covalent tether anchoring these materials. We also identify energetic matching between the triplet exciton energies of the anthracene acceptors and Si NCs to be critical in achieving efficient energy transfer between them. Our work clearly demonstrates spin-triplet exciton transfer between Si and organic molecules is indeed possible, which is a critical step for realization of biocompatible photon upconversion systems, singlet fission-based solar cells, and quantum information devices.

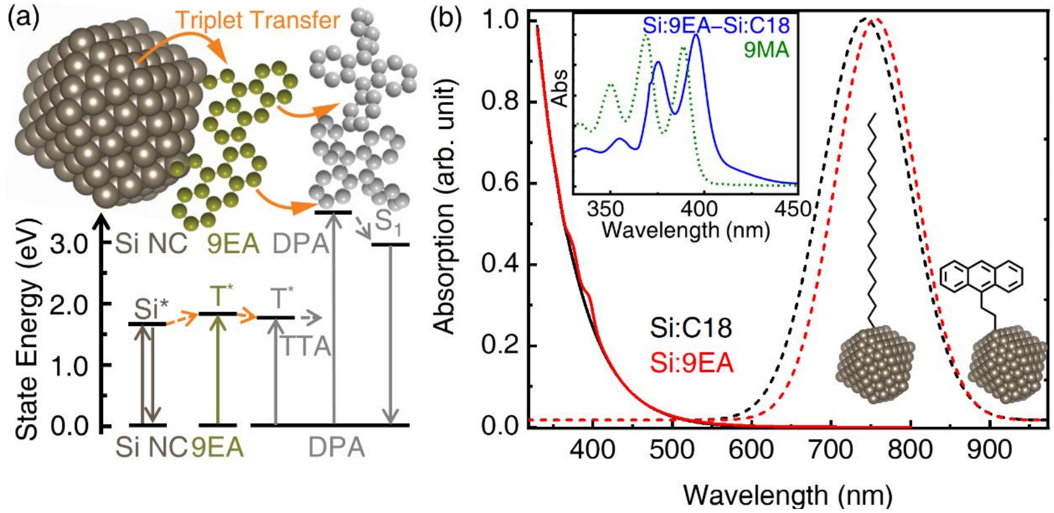

Fig. 3.1. (a) Schematic illustration of Si NC based photon upconversion. Light absorbed by Si NCs produces an excited electron-hole pair that transfers to 9-ethyl anthracene (9EA), forming a molecular spin-triplet exciton. Excited 9EA molecules then transfer these excitons to 9,10-diphenylanthracene (DPA) molecules diffusing in solution. Higher energy photons are emitted after triplet-triplet annihilation (TTA) between pairs of excited DPA molecules. (b) Absorption spectra (solid line) and emission spectra (dashed line, λ_{Ex} = 488 nm) of Si NCs functionalized with only octadecane (Si:C18, black) and a combination of octadecane and 9VA (Si:9EA, red) in toluene under argon at room temperature. (Inset) 9EA bound to Si exhibits a noticeable red-shift in its absorption features that are indicative of electronic interaction between Si and 9EA. Note, anthracene features seen in Si:9EA samples belong only to surface-bound anthracene as any free 9VA in solution has been removed via repeated washing steps.

Fig. 3.1a illustrates the NC-to-molecule triplet energy transfer scheme we employ for photon upconversion. In this scheme, low-energy photons absorbed by a Si NC produce electron-hole pairs (excitons) that pass their energy to 9,10-diphenylanthracene (DPA) molecules in solution, exciting them to a spin-triplet exciton state. When two excited DPA molecules encounter one another, they can undergo triplet-triplet annihilation (TTA), deexciting one while placing the other in a high-energy emissive spin-singlet state that proceeds to fluoresce. Prior work by our group[6,29,30] and others[7,10,31,32] has shown attachment of molecular triplet-accepting molecules to ionic chalcogenide NC triplet photosensitizers can significantly enhance photon upconversion by acting as a transmitter layer that facilitates energy transfer to molecules in solution. However, as Si NCs bind ligands via strong covalent bonds,[13] attachment of triplet transmitting molecules to these NCs requires chemistries that allow covalent attachment of acceptors while limiting the NCs' propensity to oxidize when exposed to trace amounts of water and oxygen. To this end, we chose to work with highly crystalline Si NCs synthesized via non-thermal plasma reduction of silane with hydrogen in the presence of argon.[11] Compared to Si nanoparticles made by other methods, the resulting surface hydride (SiH_x) makes these NCs amenable to thermal hydrosilylation. As detailed in the Supporting Information, Si NCs were thermally hydrosilylated with either 1-octadecene or a combination of 1-octadecene and 9-vinyl-anthracene (9VA) which converts to 9-ethyl-anthracene (9EA) on attachment. This yields two functional Si NC samples, one with a ligand shell containing only octadecane, which we label Si:C18, and a second containing a mixed ligand shell of octadecane and 9EA, which we denote Si:9EA for brevity (Fig. 7.3 Insert).

Unlike direct gap semiconductor NCs, Si NCs have a relatively featureless absorption spectrum reflecting their indirect bandgap (Fig. 3.1b, black). In line with previous reports, Si:C18 exhibits broad steady-state photoluminescence with an emission quantum yield of 16.1 ± 2.2% that peaks at 741 nm, indicating a particle diameter of 3.1 nm based on known sizing curves.[33] Upon hydrosilylation with 9VA, the NC emission red shifts by 46 meV and decreases in quantum efficiency to 8.2 ± 1.2% (Fig 3.1b). In parallel, distinct features appear in the absorption spectrum of Si:9EA that are indicative of surface-bound anthracene and are notably red-shifted by 55 meV relative to free 9-methylanthracene in toluene (Fig 3. 1b, inset). This shift is larger than that seen for comparable acene molecules bound to ionic chalcogenide NCs,[9,34–36] suggesting stronger electronic interaction between 9EA and the Si NC core. From the electronic absorption spectrum of Si:9EA, we estimate the average number of 9EA molecules bound to each Si NC, $\langle N_{9EA} \rangle$, to be 2 (Supporting Information, Section S2B). Nuclear magnetic resonance (Fig. 7.11) and attenuated total reflectance infrared spectroscopy (Fig. 7.12) also confirm the presence of surface-bound 9VA. We note infrared spectra signal some oxidation of functionalized Si NCs even when stored in a nitrogen glovebox with water <0.5 ppm and oxygen <0.2 ppm. This has been observed in Si NCs prepared by thermal hydrosilylation[37] and does not appear to be a severe barrier to triplet energy transfer.

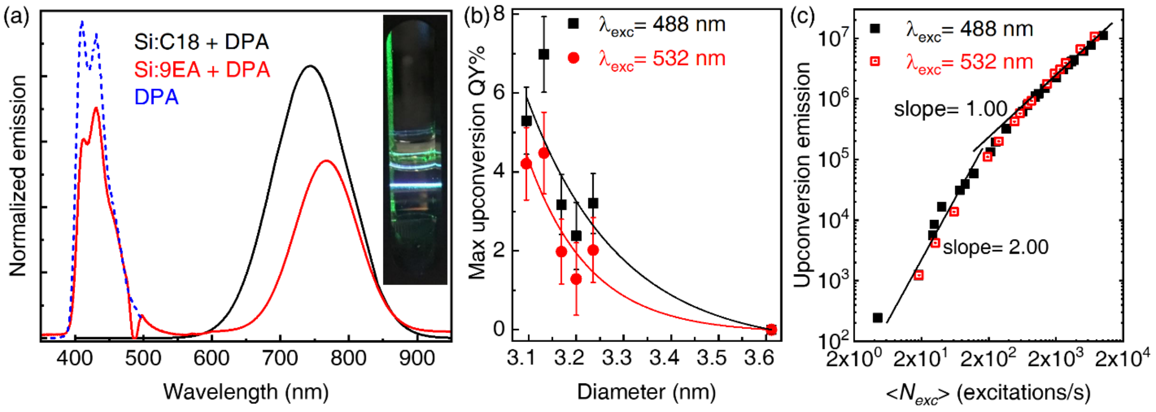

Fig. 3.2 (a) Photoluminescence spectra of 3.1 nm diameter Si NCs with octadecane only (Si:C18, black), Si NCs with 9VA functionalization (Si:9EA, red), and DPA only (blue, $\square_{\mathrm{Ex}}$ = 350 nm). (Insert) Excitation with green 532 nm light creates visible upconverted blue emission from DPA. (b) Dependence of the photon upconversion quantum yield (QY) on Si NC diameter showing that as NC size decreases, the upconversion QY increases. Solid lines are drawn as a guide to the eye. Error bars denote one standard deviation. (c) Log–log plot of the upconverted emission intensity of Si:9EA|DPA vs. $\langle N_{exc} \rangle$, the average number of times a NC is photoexcited per second under CW illumination. The upconversion emission intensity shows a transition from quadratic (slope = 2) to linear (slope = 1) regimes.

Photon upconversion measurements were performed under nitrogen with Si NC light absorbers and DPA molecular emitters in toluene at room temperature. In this multi-step triplet-based process, DPA emits violet light after combining the energy originating from two photons of lower energy. DPA is chosen because of its high (>97%) fluorescence QY and long-lived, low-lying first excited triplet state (T_1 = 1.77 eV)[38] that provides a small energetic driving force for triplet energy transfer from surface-bound 9EA (T_1 = 1.8 eV).[38,39] We find no evidence of photon upconversion when Si:C18 was used as a triplet photosensitizer in 5.2 mM DPA (Fig. 3.2a). This is expected as the octadecane ligand shell presents a formidable barrier to triplet energy transfer, which depends exponentially on the spatial separation of the energy donor and acceptor.[40] In contrast, Si:9EA displays ready photon upconversion when illuminated with visible light in the presence of DPA, achieving an upconversion QY as high as 7.0 ± 0.9% when small 3.1 − 3.2 nm diameter Si NCs are employed (Fig. 7.6 and Fig. 3.2b). Here, we have defined upconversion QY with a maximum value of 100%, meaning that 7% of absorbed photons go on to produce upconverted photons.

An important parameter for upconversion systems is the excitation rate threshold wherein the upconverted light intensity switches from a quadratic to a linear dependence on incident power. Above this threshold, TTA ceases to be rate-limiting as the steady-state triplet population in the system is sufficiently high that any photoexcited molecule will find an excited partner within their lifetime to undergo TTA. We find that for Si:9EA, this threshold falls at 0.95 W/cm^2 for a 488 nm exciting source (Fig. 3.2c) and doubles to 2 W/cm^2 for 532 nm light, reflecting the decreased absorption by the Si NCs at 532 nm relative to 488 nm. This is confirmed by plotting the upconversion intensity as a function of the excitation rate of the NCs, which causes data measured for 488 nm and 532 nm excitation sources to overlay (Fig. 3.2c). Under 640 nm excitation, a relatively low photon upconversion QY of 0.10 ± 0.07 % was measured (Fig. 7.6) showing that low-energy photons can drive upconversion despite the low optical density of Si NCs at this long wavelength.

Importantly, we find the upconverted photon quantum efficiency depends on Si NC size (Fig. 3.2b), increasing from ~0 to 7% as NC diameter decreases from 3.6 to 3.1 nm. Efforts to examine this trend further by producing smaller Si NCs were found to yield particles that were not colloidally stable after octadecane functionalization. The bandgap of Si NCs with aliphatic carbon ligands decreases with increasing Si NC diameter due to quantum confinement of charge carriers,[37,41] as noted by the peak emission wavelength of differently sized particles (Fig. 3.2b). This change in bandgap with NC size provides a clear hypothesis for the decrease in the upconversion QY we observe, as reducing Si's bandgp below 9EA's triplet energy (1.8 eV) will introduce a barrier for NC-to-molecule energy transfer.

To evaluate this hypothesis, we examined Si:C18 and Si:9EA using transient absorption (TA). Fig. 3.3a shows the spectral dynamics of Si:C18 after photoexcitation at 532 nm, which exhibit a set of broad induced absorption bands that relax over a series of time periods spanning a few nanoseconds to tens of microseconds. Such nonexponential decay has been noted previously for Si NCs[42] and can be well-reproduced by a fit model that assumes a Poisson distribution of quenching sites spread throughout the NC ensemble (Supporting Information, Section S7).

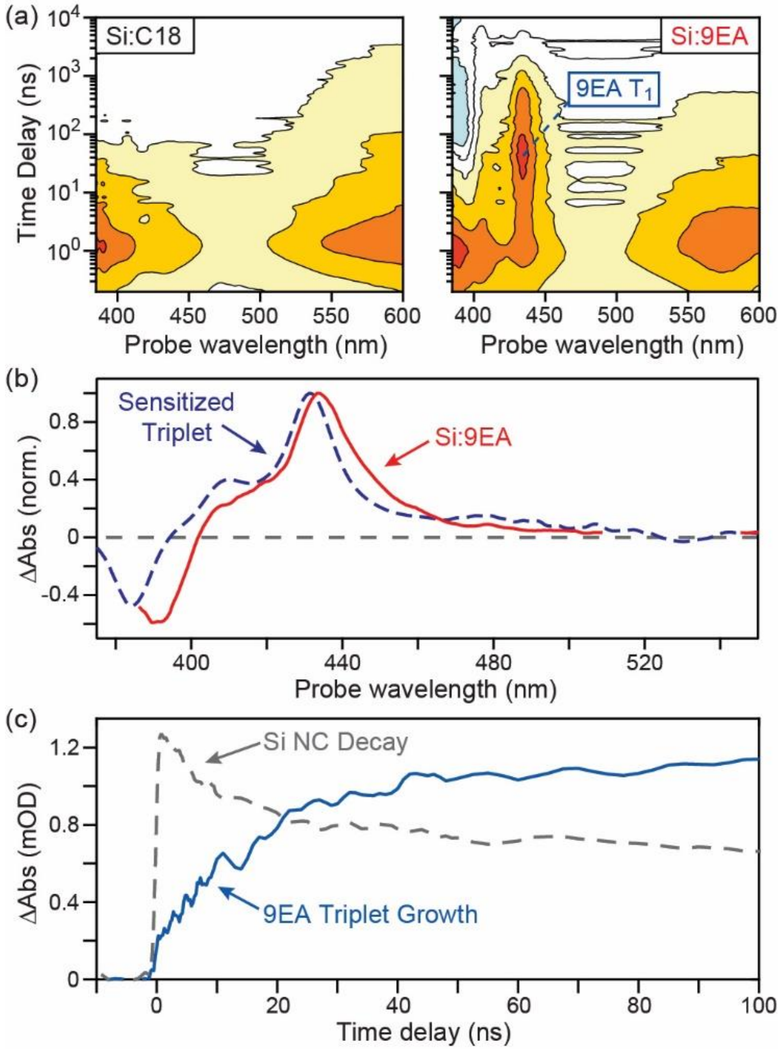

Fig. 3.3 (a) Transient absorption spectra of Si:C18 and Si:9EA. (Left) TA contour plot showing the decay of Si NC photoinduced absorption of Si:C18 following Si excitation at 532 nm. (Right) TA contour of Si:9EA showing growth of 9EA features, notably a photobleach at 395 nm (light blue contour) and induced absorption peaked at 435 nm (red/orange contours), superimposed on a Si induced absorption background. (c) Comparison of 9EA spectral features extracted from Si:9EA TA data agree with those identified in 9EA triplet sensitization experiments, confirming 9EA triplet formation following photoexcitation of Si in Si:9EA structures. (d) Kinetic traces showing 9EA triplet growth occurs on the same timescale as Si NC signal decay, with a persistent long-time Si NC signal.

Following 9EA functionalization, TA spectra show growth of a new induced absorption band peaked at 435 nm and a photobleach at 395 nm that develop over a 22 ns timescale superimposed on the Si NC signal (Fig. 3.3a, right). Isolating this new feature by subtracting the Si background yields the spectrum in Fig. 3.3b, which we assign to the 9EA triplet state based on comparison with triplet sensitization experiments (Supporting Information, Section S5). Fig. 3c plots both the 9EA triplet and excited Si NC population in time, demonstrating that the rise of the triplet signal and decay of the Si NCs occur on the same timescale, indicating 9EA triplet formation directly results from energy transfer from Si. These first order kinetics are in strong contrast to the dynamics shown in other triplet sensitizing NCs, such as PbS:pentacene, wherein NC surface states play a key role in transfer.[35,43] Rather, we see direct production of 9EA triplets as Si decays, implying the transfer occurs in a single Dexter energy transfer step from Si's lowest energy exciton band.

While it is tempting to assign the rate observed for 9EA signal growth to the Si-to-9EA Dexter energy transfer rate, this does not account for the fact that our Si:9EA ensemble consists of a distribution of variable-size NCs that bind differing numbers of 9EA molecules. The impact of this distribution is highlighted by the decay of the Si signal (Fig. 3.3c), which persists after the 9EA triplet decays. This implies that not all photoexcited Si NCs transfer an exciton to 9EA, which can be explained if a subset of NCs bind no 9EA molecules. Assuming 9EA is distributed among Si NCs according to a Poisson distribution, our prior estimate of 2 for $\langle \mathrm{N}_{9\mathrm{EA}} \rangle$ implies 13.5% of the NCs in our ensemble do not bind any 9EA molecules. While this explains a portion of the persistent Si signal at long time delays, it does not account for the shift of the NC emission energy we observe upon 9EA functionalization. Rather, the triplet energy of 9EA, 1.8 eV, is expected to introduce an energetic barrier for triplet energy transfer for some of the NCs in our ensemble with narrower band gaps. Any attempt to quantify the rate and yield of triplet energy transfer from Si to 9EA must account for these two effects.

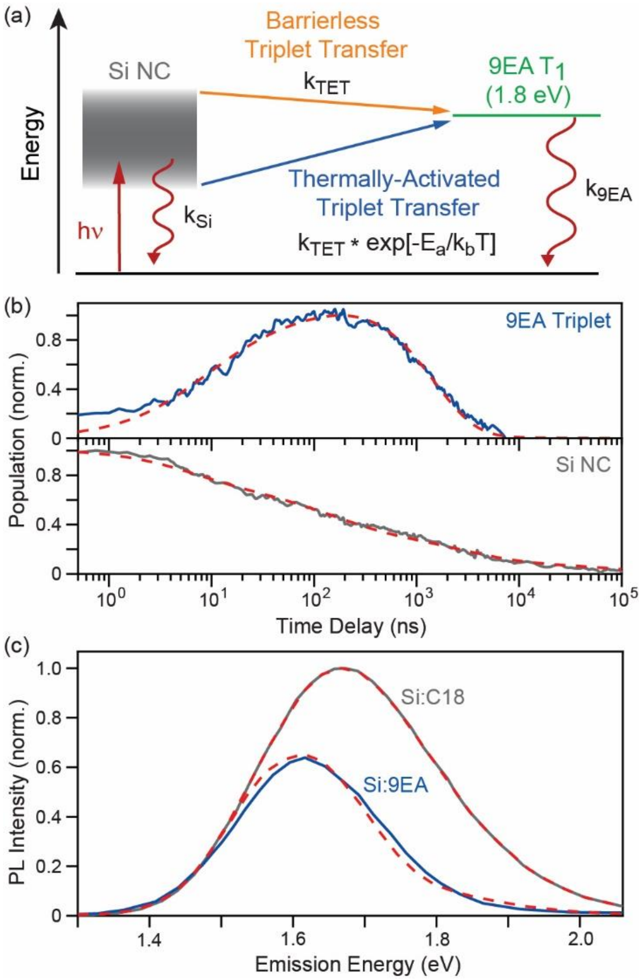

Fig. 3.4 Modeling Si:9EA dynamics. (a) Kinetic model of triplet energy transfer and decay, including heterogeneity in the bandgap of Si NCs and resultant energetic barrier to triplet transfer. (b) Fits to time-dependent populations of 9EA triplet excitons and excited Si NCs that faithfully reproduce kinetics over 5 decades in time. We note there is some discrepancy with the model at short time delays in the triplet population, which is an artifact of the background normalization used to extract this population. (c) The same model from panel (a) reproduces the energy- dependent quenching of Si NC populations after functionalization with 9EA.

Fig. 3.4a outlines a kinetic model that explains our transient results by accounting for two sources of heterogeneity that impact triplet energy transfer from Si to 9EA. This model assumes our NC ensemble is comprised of a distribution of NCs with exciton energies described by the ensemble Si NC emission linewidth. Energy transfer from NCs with an exciton energy smaller than 9EA's triplet energy are taken to experience an Arrhenius activation barrier. Members of this ensemble are further taken to bind different numbers of 9EA molecules in accordance to a Poisson distribution with $\langle N_{9EA} \rangle = 2$. Solutions to kinetic equations given by this model and a description of our fitting procedure are given in the SI. Decay parameters governing the intrinsic relaxation of Si:C18 NCs are assumed to be unchanged by 9EA functionalization, which leaves only two key free parameters to fit the growth and decay of 9EA triplet population, the forward transfer rate, k_{TET}, and 9EA decay rate, k_{9EA}. Fig. 3.4b shows the result of this fitting process overlaid on the triplet and Si NC populations extracted from Si:9EA TA data. Overall, we find very good agreement with our data over 5 decades in time despite the model's limited number of free parameters. This model also reproduces the energy-dependent quenching of Si NC emission upon 9EA functionalization (Fig. 3.4) first highlighted in Fig. 3.2b.

With these fits in hand, we can examine the overall yield for triplet energy transfer from Si NCs to 9EA. We find the intrinsic timescale of forward transfer is quite rapid, 15 ns, which implies the slower rise of 9EA triplet population in Fig. 3.4b in part arises from thermal activation of the transfer. For these samples, we find 48% of excited NCs successfully transfer energy to 9EA. Of the remaining non-transferred excitations, we estimate they result from NCs with no 9EA attached, larger NCs with exciton energies too low to effectively transfer to the 9EA triplet state, and intrinsic decay pathways within the Si NCs. Importantly, improvements in synthetic methods that either stabilize smaller Si NCs, increase 9EA loading, or replace 9EA with acceptors with lower triplet exciton energies can be straightforwardly used to address the first two of these three loss pathways, which, if eliminated, could be used to achieve transfer yields as high as 91% according to our model. Assuming a proportional gain in upconversion efficiency, this would suggest we can nearly double this value.

While our data demonstrates Si NCs can efficiently fuel triplet fusion-based photon upconversion, biological applications require Si NCs to function in aqueous, oxygen-containing environments. Using methods adapted from Sanders et al,[44] we have prepared micelles based on Poloxamer 188 (P188), a tri-block co-polymer comprised of a hydrophobic core flanked by two hydrophilic poly(ethyleneglycol) chains. P188 is a USFDA approved surfactant currently used in many over-the-counter products including toothpaste, cosmetics, and pharmaceuticals. Within the core of these micelles, Si:9EA NCs are dispersed in a small volume of o-dichlorobenzene along with DPA triplet fusion photon upconverters (Fig. 3.5a). Dynamic light scattering experiments indicate these micelles display an average diameter of 220 nm with a polydispersity index of 0.140 (Fig. 3.5b). This size is sufficiently small that these micelles are suitable for a range of biological applications.

Upon illumination under an inert argon atmosphere at either 488 nm or 512 nm, we observe upconverted emission from DPA molecules (Fig. 3.5c), confirming that Si NCs within the micelles are capable of transferring triplet excitons to surface-bound 9EA molecules followed by transfer to DPA. We find the upconverted emission tracks linearly with the input excitation power, indicating diffusion of molecules within the micelles does not limit upconversion (Fig. 3.5d). Importantly, we find when micelles are stored under inert atmosphere, they show exceptional stability. Fig. 3.5c displays emission spectra of upconverting micelles recorded 4 hours and 17 hours after preparation. These two spectra are nearly identical, highlighting their stability under anaerobic conditions.

Remarkably, when these micelles are exposed to oxygen, a notorious triplet quencher, we find photon upconversion continues over 25 minutes (Fig. 3.5e & 3.5f). In this time frame, we find the Si NC bandedge emission drops in intensity by half and undergoes a blue-shift, which is expected for NCs undergoing surface oxidation, suggesting the decay of upconversion under

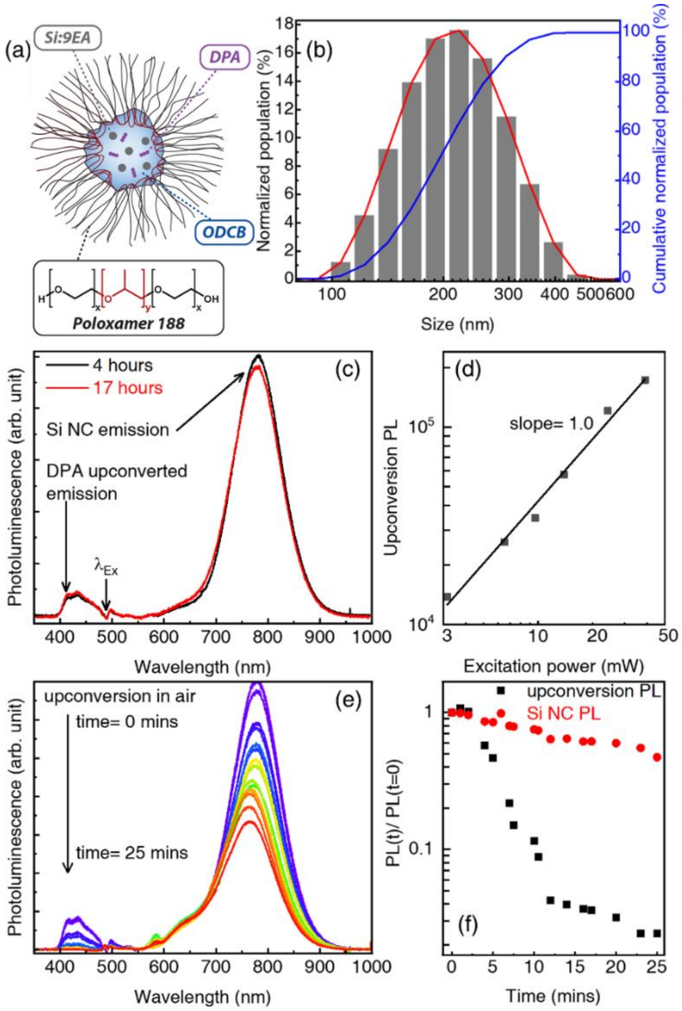

Fig. 3.5. Si NC upconversion in aqueous environments. (a) Schematic of aqueous photon upconverting micelles. (b) Micelle size distribution determined by dynamic light scattering. (c) Stability of photon upconversion in aqueous micelles under argon (λ_{ex} = 488 nm). Particles are stable over multiple days with no observed degradation of upconversion emission. (d) Upconversion emission in micelles shows a linear dependence on excitation power. (e) Stability of photon upconversion in aqueous micelles under exposure to ambient air (λ_{ex} = 488 nm). Air exposure starts at time = 0 mins. (f) As air exposure time increases, upconverted photoluminescence (PL) decreases due to oxygen quenching of triplet states (black squares). Si NC emission also decreases, suggesting some oxidation of NC surfaces (red circles).

aerobic conditions partially stems from oxidation of Si in addition to direct triplet quenching by oxygen. However, we note that in forming our micelles we have taken no explicit steps to block oxygen from reaching micelle interiors other than initially preparing them under argon. Replacement of P188 by other surfactants containing larger regions of saturated carbons that can more densely pack[45,46] and the addition of oxygen scavengers to micelle interiors[47] can each be used to improve photon upconversion longevity in aerobic, aqueous environments, increasing the promise of this system for biological applications.

3.3 Conclusion

We have demonstrated for the first-time photon upconversion employing Si NCs paired with triplet-accepting molecules. Upon excitation, triplet energy transfer occurs over a few tens of nanoseconds via a single Dexter energy transfer step, producing molecular triplet states that can be extracted to fuel upconversion between diffusing molecules in solution. This scheme upconverts green and red light with 7.0% ± 0.9% efficiency. Losses in this system stem in part from heterogeneity in NC synthesis and molecular functionalization that can be reduced with further improvements in synthetic methodology. When incorporated into aqueous micelles, our upconversion system functions indefinitely under anaerobic conditions and for 10s of minutes under oxygen exposure. These results stand out among other molecular and NC based triplet fusion upconversion systems, which are typically incompatible with aqueous conditions and exhibit triplet quenching within a few seconds upon oxygen exposure. Given numerous potential handles for improving our system, we believe Si NC-based photon upconversion can meet the demands of a number of biological applications.[3,4,48] Of even greater importance, our results definitely show Si-to-molecule spin-triplet energy transfer is indeed possible, which opens the door for many applications that extend beyond biocompatible upconversion systems.

By virtue of its inherent sustainability and environmental compatibility, our silicon-centered approach is highly relevant for quantum information science,[25] singlet fission driven solar cells,[24,49,50] and upconversion photocatalytic systems.[1]

3.4 Notes and references

1. Ravetz, B. D. et al. Photoredox catalysis using infrared light via triplet fusion upconversion. *Nature* 565, 343–346 (2019).

2. Tayebjee, M. J. Y., McCamey, D. R. & Schmidt, T. W. Beyond Shockley–Queisser: Molecular Approaches to High-Efficiency Photovoltaics. *J. Phys. Chem. Lett*. 6, 2367–2378 (2015).

3. Chen, S. et al. Near-infrared deep brain stimulation via upconversion nanoparticle–mediated optogenetics. *Science* 359, 679–684 (2018).

4. Lin, X. et al. Core–Shell–Shell Upconversion Nanoparticles with Enhanced Emission for Wireless Optogenetic Inhibition. *Nano Lett.* 18, 948–956 (2018).

5. Wu, M. et al. Solid-state infrared-to-visible upconversion sensitized by colloidal nanocrystals. *Nat. Photonics* 10, 31–34 (2015).

6. Huang, Z. et al. Hybrid Molecule–Nanocrystal Photon Upconversion Across the Visible and Near-Infrared. *Nano Lett*. 15, 5552–5557 (2015).

7. Mongin, C., Garakyaraghi, S., Razgoniaeva, N., Zamkov, M. & Castellano, F. N. Direct observation of triplet energy transfer from semiconductor nanocrystals. *Science* 351, 369–372 (2016).

8. Li, X., Fast, A., Huang, Z., Fishman, D. A. & Tang, M. L. Complementary Lock-and-Key Ligand Binding of a Triplet Transmitter to a Nanocrystal Photosensitizer. *Angew. Chem. Int. Ed.* 56, 5598–5602 (2017).

9. Li, X., Huang, Z., Zavala, R. & Tang, M. L. Distance-Dependent Triplet Energy Transfer between CdSe Nanocrystals and Surface Bound Anthracene. *J. Phys. Chem. Lett.* 7, 1955–1959 (2016).

10. Garakyaraghi, S. & Castellano, F. N. Nanocrystals for Triplet Sensitization: Molecular Behavior from Quantum-Confined Materials. Inorg. Chem. 57, 2351–2359 (2018).

11. Mangolini, L., Thimsen, E. & Kortshagen, U. High-Yield Plasma Synthesis of Luminescent Silicon Nanocrystals. *Nano Lett*. 5, 655–659 (2005).

12. Limpens, R., Pach, G. F. & Neale, N. R. Nonthermal Plasma-Synthesized Phosphorus–

Boron co-Doped Si Nanocrystals: A New Approach to Nontoxic NIR-Emitters. *Chem. Mater.* 31, 4426–4435 (2019).

13. Hessel, C. M. et al. Synthesis of Ligand-Stabilized Silicon Nanocrystals with Size-Dependent Photoluminescence Spanning Visible to Near-Infrared Wavelengths. *Chem. Mater.* 24, 393–401 (2012).

14. Wilson, M. W. B. et al. Ultrafast dynamics of exciton fission in polycrystalline pentacene. *J. Am. Chem. Soc*. 133, 11830–11833 (2011).

15. Burdett, J. J., Müller, A. M., Gosztola, D. & Bardeen, C. J. Excited state dynamics in solid and monomeric tetracene: The roles of superradiance and exciton fission. J. Chem. Phys. 133, 144506 (2010).

16. Sanders, S. N. et al. Quantitative Intramolecular Singlet Fission in Bipentacenes. *J. Am. Chem. Soc*. 137, 8965–8972 (2015).

17. Zirzlmeier, J. et al. Singlet fission in pentacene dimers. Proc. Natl. Acad. Sci. 112, 5325–5330 (2015).

18. Eaton, S. W. et al. Singlet exciton fission in polycrystalline thin films of a slip-stacked perylenediimide. *J. Am. Chem. Soc*. 135, 14701–12 (2013).

19. Le, A. K. et al. Singlet Fission Involves an Interplay between Energetic Driving Force and Electronic Coupling in Perylenediimide Films. *J. Am. Chem. Soc*. 140, 814–826 (2018).

20. Johnson, J. C., Nozik, A. J. & Michl, J. High triplet yield from singlet fission in a thin film of 1,3-diphenylisobenzofuran. *J. Am. Chem. Soc*. 132, 16302–16303 (2010).

21. Wang, C. & Tauber, M. J. High-yield singlet fission in a zeaxanthin aggregate observed by picosecond resonance Raman spectroscopy. *J. Am. Chem. Soc*. 132, 13988–13991 (2010).

22. Lukman, S. et al. Efficient Singlet Fission and Triplet-Pair Emission in a Family of Zethrene Diradicaloids. *J. Am. Chem. Soc*. 139, 18376–18385 (2017).

23. Hanna, M. C. & Nozik, A. J. Solar conversion efficiency of photovoltaic and photoelectrolysis cells with carrier multiplication absorbers. J. Appl. Phys. 100, 74510 (2006).

24. Futscher, M. H., Rao, A. & Ehrler, B. The Potential of Singlet Fission Photon Multipliers as an Alternative to Silicon-Based Tandem Solar Cells. ACS Energy Lett. 3, 2587–2592 (2018).

25. Weiss, L. R. et al. Strongly exchange-coupled triplet pairs in an organic semiconductor. Nat. Phys. 13, 176–181 (2017).

26. Einzinger, M. et al. Sensitization of silicon by singlet exciton fission in tetracene. Nature 571, 90–94 (2019).

27. Han, Y. et al. Visible-Light-Driven Sensitization of Naphthalene Triplets Using Quantum-Confined CsPbBr 3 Nanocrystals. *J. Phys. Chem. Lett.* 10, 1457–1463 (2019).

28. Huang, Z. et al. Enhanced Near-Infrared-to-Visible Upconversion by Synthetic Control of PbS Nanocrystal Triplet Photosensitizers. *J. Am. Chem. Soc*. 141, 9769–9772 (2019).

29. Mahboub, M., Huang, Z. & Tang, M. L. Efficient Infrared-to-Visible Upconversion with Subsolar Irradiance. *Nano Lett*. 16, 7169–7175 (2016).

30. Huang, Z. & Tang, M. L. Designing Transmitter Ligands That Mediate Energy Transfer between Semiconductor Nanocrystals and Molecules. *J. Am. Chem. Soc*. 139, 9412–9418 (2017).

31. Okumura, K., Mase, K., Yanai, N. & Kimizuka, N. Employing Core-Shell Quantum Dots as Triplet Sensitizers for Photon Upconversion. Chem. - Eur. J. 22, 7721–7726 (2016).

32. Yanai, N. & Kimizuka, N. New Triplet Sensitization Routes for Photon Upconversion: Thermally Activated Delayed Fluorescence Molecules, Inorganic Nanocrystals, and Singlet-to-Triplet Absorption. Acc. Chem. Res. 50, 2487–2495 (2017).

33. Wheeler, L. M. et al. Silyl Radical Abstraction in the Functionalization of Plasma-Synthesized Silicon Nanocrystals. *Chem. Mater.* 27, 6869–6878 (2015).

34. Kroupa, D. M. et al. Control of Energy Flow Dynamics between Tetracene Ligands and PbS Quantum Dots by Size Tuning and Ligand Coverage. *Nano Lett*. 18, 865–873 (2018).

35. Bender, J. A. et al. Surface States Mediate Triplet Energy Transfer in Nanocrystal–Acene Composite Systems. *J. Am. Chem. Soc*. 140, 7543–7553 (2018).

36. Davis, N. J. L. K. et al. Singlet Fission and Triplet Transfer to PbS Quantum Dots in TIPS-Tetracene Carboxylic Acid Ligands. *J. Phys. Chem. Lett.* 9, 1454–1460 (2018).

37. Carroll, G. M., Limpens, R. & Neale, N. R. Tuning Confinement in Colloidal Silicon Nanocrystals with Saturated Surface Ligands. *Nano Lett*. 18, 3118–3124 (2018).

38. Montalti, M., Credi, A., Prodi, L. & Gandolfi, M. T. Handbook of Photochemistry. (CRC Press/Taylor and Francis, 2006).

39. Evans, D. F. Perturbation of Singlet Triplet Transitions of Aromatic Molecules by Oxygen under Pressure. *J. Chem. Soc.* 1351–1357 (1957).

40. Dexter, D. L. A Theory of Sensitized Luminescence in Solids. J. Chem. Phys. 21, 836–836 (1953).

41. Yu, Y. et al. Size-Dependent Photoluminescence Efficiency of Silicon Nanocrystal Quantum Dots. *J. Phys. Chem. C* 121, 23240–23248 (2017).

42. Stolle, C. J., Lu, X., Yu, Y., Schaller, R. D. & Korgel, B. A. Efficient Carrier Multiplication in Colloidal Silicon Nanorods. *Nano Lett*. 17, 5580–5586 (2017).

43. Garakyaraghi, S., Mongin, C., Granger, D. B., Anthony, J. E. & Castellano, F. N. Delayed Molecular Triplet Generation from Energized Lead Sulfide Quantum Dots. *J. Phys. Chem. Lett.* 8, 1458–1463 (2017).

44. Sanders, S. N., Gangishetty, M. K., Sfeir, M. Y. & Congreve, D. N. Photon Upconversion in Aqueous Nanodroplets. *J. Am. Chem. Soc*. 141, 9180–9184 (2019).

45. Kouno, H., Sasaki, Y., Yanai, N. & Kimizuka, N. Supramolecular Crowding Can Avoid Oxygen Quenching of Photon Upconversion in Water. Chem. – Eur. J. 25, 6124–6130 (2019).

46. Kim, J.-H. & Kim, J.-H. Encapsulated Triplet–Triplet Annihilation-Based Upconversion in the Aqueous Phase for Sub-Band-Gap Semiconductor Photocatalysis. *J. Am. Chem. Soc*. 134, 17478–17481 (2012).

47. Marsico, F. et al. Hyperbranched Unsaturated Polyphosphates as a Protective Matrix for Long-Term Photon Upconversion in Air. *J. Am. Chem. Soc*. 136, 11057–11064 (2014).

48. Weissleder, R. A clearer vision for in vivo imaging. Nat. Biotechnol. 19, 316–317 (2001).

49. Dexter, D. L. Two ideas on energy transfer phenomena: Ion-pair effects involving the OH stretching mode, and sensitization of photovoltaic cells. J. Lumin. 18, 779–784 (1979).

50. MacQueen, R. W. et al. Crystalline silicon solar cells with tetracene interlayers: the path to silicon-singlet fission heterojunction devices. Mater. Horiz. 5, 1065–1075 (2018).

4 Chapter 4 surface fluorination for controlling pbs quantum dot bandgap and band offset

4.1 Introduction

The ability to tune the energy levels in semiconductor nanocrystals or QDs is critical for high performing and cost-effective photovoltaic cells. While synthetic control of the size and dimensions of semiconductor nanostructures allow their bandgap to be tuned, it is much more challenging to shift band offsets. Doping strategies used for bulk semiconductors typically fail because QDs expel impurities in a self-purification process, especially at the high temperatures necessary for synthesis.[1] While transition metal ions like Mn^{2+} have been successfully incorporated into the QD lattice, there is little perturbation to the band offsets.[2] The ability to adjust QD energy levels with the different ligand treatments potentially provides an inexpensive way to increase the depletion layer in QD solar cells. A depletion layer on the order of the absorption depth would improve charge extraction and ultimately increase the power conversion efficiency. [3-6]

Here, we show for the first time that the electron-withdrawing nature of fluorine containing ligands can be used to lower the band offsets of PbS QDs and modify their bandgap. In addition, the sterics and oleophobic nature of perfluorocarbons modify QD ligand shell permeability in organic solvent. This work builds on the vast literature showing fluorination is effective for controlling molecular and material properties. For example, the electronegativity of fluorine has been used to switch organic semiconductors from p-type to n-type;[7-9] quadrapolar interactions in perfluorobenzene induce an edge to face stacking unobserved in benzene,[10, 11] small molecule drugs display vastly improved potency and biological compatibility when C-H bonds are replaced with C-F bonds, etc.[12] More recently, fluorinated perovskite solar cells have shown enhanced stability.[13] Indeed, artificial molecules like quantum confined semiconductor nanocrystals, with their inorganic core and organic shell, should respond to strategies for molecular engineering.

In this work, the novel physical and electronic properties of trifluoromethane thiolate (-SCF_3) and perfluorohexadecanoic acid (pFA) functionalized PbS QDs are reported. As a control, we examine methanethiolate (-SCH_3) capped QDs and the original oleic acid (OA) capped QDs. This allows the effects of sterics and electronegativity to be deconvoluted, because pFA and OA are long chain carbon containing ligands of approximately the same length with the same carboxylic acid functional group. Similarly, both -SCF_3 and -SCH_3 bind to the QD surface with the thiol group. Complete replacement of the original OA ligands was confirmed by attenuated total reflection-infrared (ATR-IR) spectroscopy for pFA and SCF_3 functionalized QDs. Since these completely perfluorinated QDs are only soluble in fluorous solvents and insoluble in most organic solvents (hydrocarbons, ethers, alcohols, aliphatic nitriles, etc.), we chose to work with partially functionalized QDs, colloidally stable in common solvents for cyclic voltammetry (CV) and photo-induced electron transfer experiments. Steady-state and time-resolved Stern-Volmer quenching experiments allowed the permeability and reducing potential of the partially fluorinated QDs to be studied in combination with CV and nuclear magnetic resonance (NMR) spectroscopy. We show that replacement of a third of the original OA with perfluorinated ligands decreases the PbS QD's reducing potential up to 0.18 eV. The short thiolate ligands increase the permeability of the ligand shell, enhancing PET by a factor of 7.

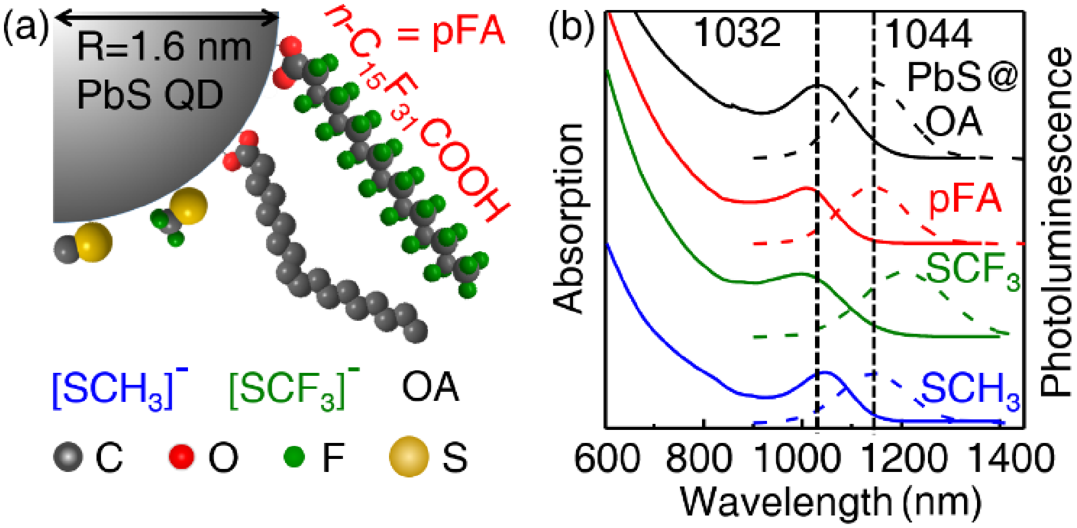

Fig. 4.1 (a) PbS QDs (diameter = 3.3 nm) with perfluorohexadecanoic acid (pFA), trifluoromethane thiolate (-SCF$_3$), methanethiolate, (-SCH$_3$), and oleic acid (OA) ligands. (b) Absorbance and photoluminescence spectra of 0.244 µM PbS QDs with the ligands in (a), photoexcited at 532 nm. All spectra are in toluene at RT except for PbS@pFA, measured in trifluorotoluene.

4.2 Experiments

Ligand exchange was performed on 3.3 nm diameter OA capped PbS QDs, i.e. PbS@OA, synthesized by the hot injection method,[14, 15] with the first absorption maxima, λ_{abs}, at 1032 nm. The incoming ligands were dissolved in polar solvents like ethanol, THF or acetonitrile, and mixed with the as-synthesized OA-capped PbS QDs in toluene under argon (See Table 7.3 for the details on ligand exchange). The functionalized PbS QDs after ligand exchange are denoted as PbS@ligand, e.g. PbS@pFA, PbS@SCF$_3$ and PbS@SCH$_3$ (Fig. 4.1a). The absorption and photoluminescence (PL) spectra of colloidal QDs with partial replacement of OA are in Fig. 4.1b.

Table 4.1 Optical properties and energy levels of PbS@ligand QDs, including the first absorption maxima, λ_{abs}; photoluminescence (PL) maxima, λ_{em}; PL quantum yield, PLQY (%); optical band gap, E_{gap}; conduction band, CB; valence band, VB; radiative decay and nonradiative decay rates, k_r and k_{nr}.

QD	λ_{abs}/nm	λ_{em}/nm	PLQY(%)	E_{gap}/eV	CB^a/eV	VB^b/eV	k_r/ns^{-1}	k_{nr}/ns^{-1}
PbS@OA	1032	1141	8.0	1.20	-3.75	-4.95	23.5	271
PbS@pFA^c	1022	1142	2.4	1.21	-3.93	-5.14	6.12	249
PbS@SCH_3	1043	1146	6.0	1.19	-3.71	-4.90	12.7	235
PbS@SCF_3	1008	1207	5.1	1.23	-3.67	-4.90	17.3	272

[a]CB measured with cyclic voltammetry. [b]VB calculated from optical gap. [c]All measurements in toluene other than PbS@pFA in trifluorotoluene, $PhCF_3$.

The fluorinated ligands, $-SCF_3$ and pFA, blue shift the λ_{abs} of the PbS QDs by 35 nm and 10 nm respectively when compared to the $-SCH_3$ and OA capped QDs (Table 4.1). On the other hand, PbS@SCH_3 shows an 11-nm red shift compared to PbS@OA. This is easily explained by a decrease in quantum confinement due to deposition of the thiolate on the PbS surface, mirroring the bathochromic shift observed when a monolayer of sulfide is deposited on PbS nanocrystals.[16] Since the PL of PbS@pFA and PbS@SCH_3 did not change much compared to PbS@OA, and the transmission electron micrographs show that QD size is conserved (Fig. 7.19), we ruled out ligand induced etching of the QDs. The unprecedented blue shift of the QDs with the perfluorinated ligands is due to the changes in the dielectric environment of the ligand shell that affect the energetics of the ground and excited states. According to the Lippert-Mataga equation[17-19], applicable in the aprotic solvents used here where the polarizability of the fluorophore is neglected, a larger Stokes shift is expected for solvents with larger dielectric constants, ε, and a hypsochromic shift is expected in the absorption when the refractive index, n, decreases. The proximity of the CF_3 group to the PbS surface when bound by the $-SCF_3$

ligand, and the larger dielectric constant of CF_4 (n =1.0005[20], ε =1.287[21]) results in a 96 nm larger Stokes shift of PbS@SCF_3 compared to PbS@SCH_3 (n =1.0004[22], ε =1.064[23] for CH_4). For PbS@pFA, $C_{15}F_{32}$ has a lower refractive index (n =1.27-1.33[24], ε = 2.04[25]) that is lower than that of $C_{15}H_{32}$ (n = 1.43[26]; ε = 1.814[27]), resulting in 10 nm blue shift in absorption compared to PbS@OA. A related blue shift is observed in molecular systems, e.g. in coumarin dyes when perfluoroheptyl groups are substituted at the 7-position.[28] In contrast, a bathochromic shift is observed when Weinberg et al. partially functionalized PbS QDs with perfluorodecanethiol, $CF_3(CF_2)_7(CH_2)_2SH$, because the C-F bonds are separated from the QD core by 2 carbon spacers.[29]

The QD PL becomes broader after ligand exchange with the thiolate ligands. The PL quantum yields (PLQY), radiative and non-radiative decay rates, k_r and k_{nr}, of the four QD samples are listed in Table 4.1. As can be seen, there is a slight drop in PLQYs after ligand exchange, but k_r and k_{nr} remain on the same order of magnitude, typical of PbS QDs.[30]

ATR-IR confirms binding of -SCF_3, -SCH_3 and pFA on PbS QDs after ligand exchange. ATR-IR spectra for QD samples with complete ligand exchange are shown in Fig. 4.2a. As can be seen, the surface bound ligands register peak positions blue shifted compared to the free ligands (Fig. 7.2), indicating successful ligand exchange. In the blue trace for PbS@SCF_3, OA is completely displaced (see black curve for PbS@OA), as observed by the missing C-H stretches at 2948 and 2918 cm^{-1}, 1523 cm^{-1} for ν (C-O) and 1394 cm^{-1} of δ (C-O). Instead, the ATR-IR spectra for PbS@SCF_3 shows new peaks at 1488 cm^{-1}, 1045 cm^{-1} and 955 cm^{-1}, which correspond to the bending of C-H bonds from the [NMe_4] group, δ(C-O), and the asymmetric and symmetric stretching of CF_3 bonds[31, 32], $\nu_{as}CF_3$ and ν_sCF_3, respectively. Coupled with the blue shift of $\nu_{as}CF_3$ and ν_sCF_3 in PbS@SCF_3, this indicates that the -SCF_3 fully replaces OA and binds on the surface of PbS QD. For PbS@pFA, a blue shift of the asymmetric and symmetric CF_2 stretch at 1209 cm^{-1} and 1151 cm^{-1} is observed. Replacement of the C-O stretch at 1623 cm^{-1} with the C=O at 1754 cm^{-1} suggests pFA binds on the PbS QD surface[33] in a bidentate geometry, as reported by Luther et al. for OA on PbSe QDs.[34] For PbS@SCH_3, the big blue shift of the CH_3 bend from 1435 cm^{-1} to 1445 cm^{-1} verifies that SCH_3 is bound to the QD surface.[35] The band around 3400 cm^{-1} is probably due to O-H stretching vibrations from the adsorption of moisture by hygroscopic $NaSCH_3$. The ATR-IR peak positions are in Table 7.11. QDs with approximately one third of surface ligands perfluorinated were still colloidally stable and thus allowed analysis of ligand composition by NMR. Fig. 3.2b shows the ^1H NMR spectra of PbS@ligand complexes with ferrocene serving as the internal standard (see Table 7.5 for details). The resonance at 5.50 ppm from the alkene protons of OA was used to estimate the amount of OA for a known concentration of QDs. Assuming that the original OA was replaced by the new ligands, the remaining OA allows the lower bound of newly installed ligands on the QD surface to be estimated at 0.32, 0.28 and 0.35 for pFA, $-SCF_3$ and $-SCH_3$ respectively (see details of calculation in Table 7.5). Ligand exchange is further validated by the ^{19}F NMR spectra in Fig. 4.2c. The original $\ominus SCF_3$ anion's sharp resonance at -7.8 ppm is no longer observed when this ligand is bound to the PbS QD, and a new peak appears at 43.2 ppm. The same surface bound $-SCF_3$ shows ^{19}F NMR resonances at 43.9 ppm and 44.1 ppm on CdSe and CdS QDs respectively in mixtures of $CDCl_3$ and acetonitrile (Fig. 7.2c). Considering that $(SCF_3)_2C{=}S$ has its ^{19}F NMR chemical shift at 42.0 ppm,[36] neutral $(SCF_3)_xPbS_y$ complexes might be formed on the QD surface (x and y are integer ratios as Pb^{2+} on QDs surface is bound to sulfide). In Fig. 4.2d, the broad signals in the fluorine NMR for PbS@pFA confirm that pFA is bound on the QD surface.

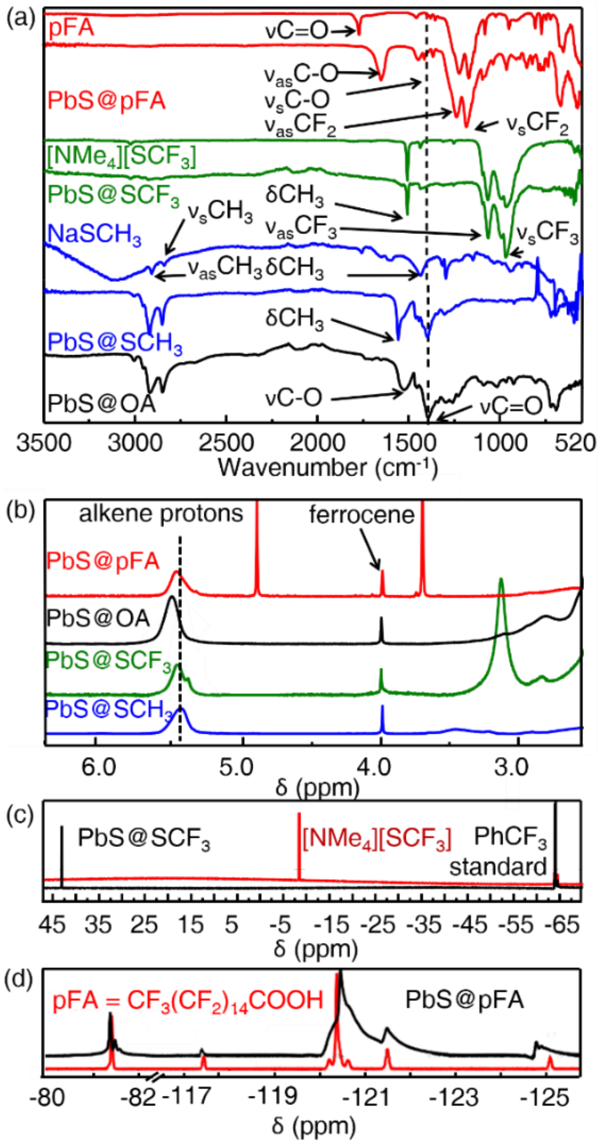

Fig. 4.2. (a) ATR-IR spectra of pure pFA, $[NMe_4][SCF_3]$ and $NaSCH_3$ ligands and PbS@ligand complexes with PbS@OA (black); pFA and PbS@pFA (red); $[NMe_4][SCF_3]$ and PbS@SCF_3 (green); $NaSCH_3$ and PbS@SCH_3 (blue). (b) ^1H NMR spectra of PbS@ligand, normalized with the ferrocene peak. (c) ^{19}F NMR of $[NMe_4][SCF_3]$ (red) and PbS@SCF_3 (black) in toluene-d8: acetonitrile= 5:1 with $PhCF_3$ as the internal standard. (d) ^{19}F NMR of pFA (red) & PbS@pFA (black) in toluene-d_8: acetone= 5:1 with $PhCF_3$ as the internal standard.

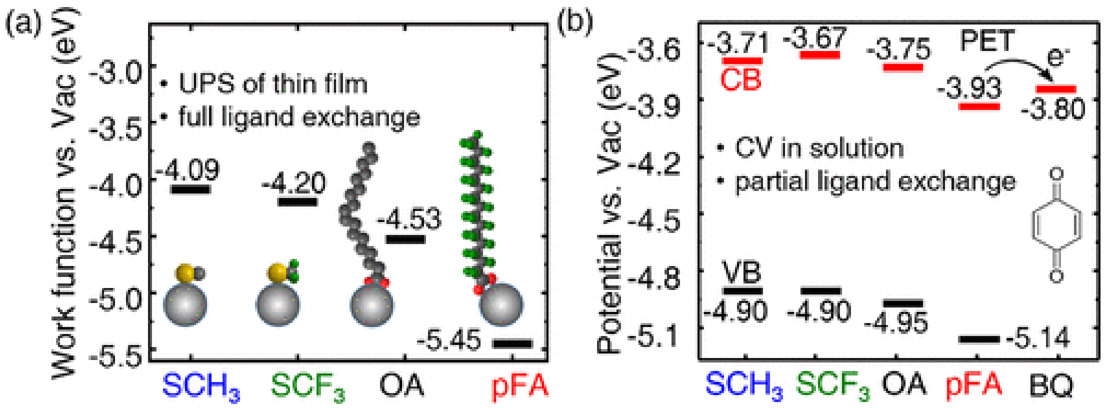

Fig. 4.3. Energy diagram of the PbS@ligand. (a) Work function of the thin films after complete ligand exchange of PbS QDs (λ_{max} = 1053 nm) measured by UPS. (b) In solution with partial ligand exchange of PbS QDs (λ_{max} = 1032 nm), in comparison with the lowest unoccupied molecular orbital (LUMO) of benzoquinone (BQ)[37]. The conduction bands (CBs) of the PbS@ligand complexes were measured by CV in a 2:1 dichloromethane (DCM)/toluene mixture or 2:1 DCM/PhCF$_3$ mixture for PbS@pFA at −40 °C.

Cyclic voltammetry (CV) and ultra-violet photoelectron spectroscopy (UPS) [38]were used to quantify the change in the energy levels induced by the new ligands. The electron-withdrawing pFA ligand decreases the band offsets of the PbS QDs by 1.0 eV when it fully replaces OA (Fig. 4.3a), and 0.18 eV when pFA makes up 32% of surface ligands (Fig. 4.3b). Although it was difficult to accurately define the valence band maxima from UPS measurements of PbS QD films because of the low density of states at the valence band maximum,[39] the energy level shifts in the valence bands of the fully ligand exchanged films observed with UPS were in qualitative agreement with the trend in the VB values measured by CV of the partially ligand exchanged QDs.

In comparison, when all the OA ligands are replaced by the electron-donating SCF$_3$, the conduction band (CB) of PbS QDs was increased by ~0.35 eV in thin film, and 0.1 eV in solution with 28 % replacement. While it has been shown that ligand dipole moment can shift the absolute energy levels of the QDs[30,40], this is the first time that ligand electronegativity is used to modify QD band offsets, resulting in such a large shift of electronic energy levels, which is larger than Brown's et al. report.[30] Molecular dipole moments have been used to shift the energy levels in PbS QD thin films by up to 0.9 eV with different organic (e.g. cinnamate[15]) and ionic surface treatments.[30] The Lewis basic character of the -SCH_3 and –COOH binding groups introduce an interface dipole when bound to the Pb^{2+} ions on the QD surface. Based on the change in work function of metal substrates,[41,42] when functionalized with -SCF_3 and -SCH_3 (e.g. on gold, silver and copper surfaces[43,44]) the thiolate group should result in a net positive dipole. Experimentally, the thiolates resulted in 0.44 and 0.33 eV decreases in the work function for PbS@SCH_3 and PbS@SCF_3, respectively, with respect to that of PbS@OA. The reduced work function for PbS@SCF_3 relative to that of PbS@OA was a result of the competition between the electron-donating sulfur and electron-withdrawing CF_3 group.

PET was performed to quantify changes in the reduction potential of the QD. In the presence of a benzoquinone (BQ), acceptor, the steady-state PL of the PbS QD donor is quenched, and its lifetime decreased due to electron transfer.[45] Here, PbS@OA, PbS@SCF_3 and PbS@SCH_3 QDs in toluene and PbS@pFA QDs in $PhCF_3$ were prepared with different concentrations of BQ. The time-dependent and steady-state PL quenching data for PbS@pFA when excited with 480 nm and 532 nm respectively are shown in Fig. 4.4a and Fig. 4.4b. (PL quenching data for the other three samples are in Fig. 7.20). Time correlated single photon counting (TCSPC) experiments revealed that the QDs have two decay components: one fast decay (0.1-0.6 μs) and one slow decay (2.8-4.0 μs) (Table 7.8), similar to the values Caram et al. reported for the PL decay of single PbS QDs.[46] All of the experiments were conducted in the linear regime with excitation energy as low as 100 nJ.

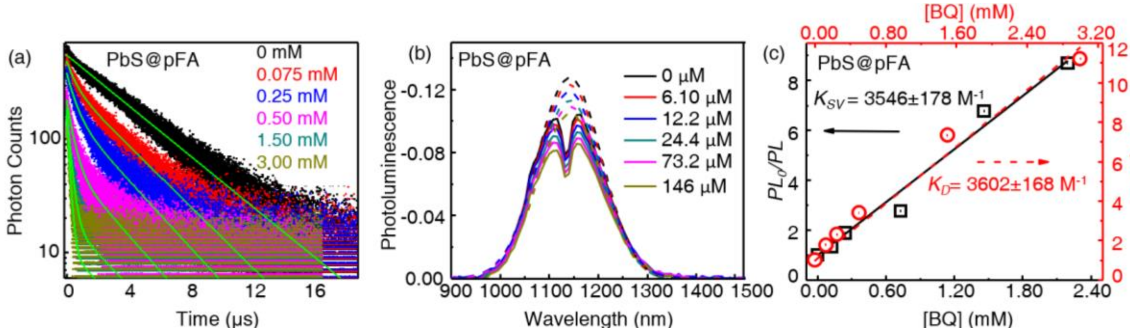

Fig. 4.4 (a) Time-resolved photoluminescence (PL) of 5 µM PbS@pFA in $\mathrm{PhCF_3}$ in the absence (black) and presence of different concentrations of BQ, [BQ]. The green solid line is the fit with a bi-exponential decay. (b) Steady-state PL of 0.244 µM PbS@pFA with different [BQ] in $\mathrm{PhCF_3}$. The solid line is the as-obtained experimental data and the dashed line is the PL spectra after correction for solvent absorption. (c) PL_0/PL vs. [BQ] and $<\tau_0>/<\tau>$ vs. [BQ]. PL_0 and $<\tau_0>$ are the steady-state PL and intrinsic amplitude averaged lifetime of PbS@pFA in the absence of BQ, while PL and $<\tau>$ are the corresponding values in the presence of BQ. K_D and K_{SV} are the Stern-Volmer quenching constants obtained from a linear fit to the changes in QD amplitude average lifetime and steady-state PL respectively.

The PbS QDs here are dynamically quenched by BQ, with both the thiolate capped QDs being more effective PET donors. The fact that dynamic quenching occurs is reflected in the similar values obtained for steady-state and dynamic Stern-Volmer quenching constants, K_{sv} and K_D, respectively, provided independently by linear and ultra-fast PL measurements (Table 4.2 . Key parameters of photo-induced electron transfer (PET) from PbS QDs to benzoquinone, BQ, including the intensity averaged lifetime, $\bar{\tau}_0$; Stern-Volmer quenching constants, KSV and KD; bimolecular quenching rate, kq; quenching efficiency, fQ and driving force, ΔG.). It is also reflected in the linear relationship between PL_0/PL vs BQ concentration, [BQ], in Fig. 4.4c. PL_0 and PL are the PL intensities of QD samples in the absence and presence of BQ respectively, and PL_0/PL is the ratio at different [BQ]. The steady-state quenching data, PL_0/PL vs. [BQ] for other ligands are in Fig. 7.20. The Stern-Volmer equation (eq. 4.1) is applied to calculate the quenching constants K_{sv} and K_D from the data in Fig. 4.4c (eq. 4.1 and eq. 4.2), while the bimolecular quenching constant, k_q, is extracted from TCSPC measurements of the intrinsic lifetime of the PbS QDs, $<\tau_0>$ or $\bar{\tau}_0$, for each PbS@ligand complex (Table 4.2). $<\tau_0>/<\tau>$ is the ratio of amplitude averaged lifetimes of PbS@ligand in the absence and presence of BQ.

$$\mathrm{PL_0/PL} = 1 + \mathrm{K_{SV}[BQ]} = 1 + \mathrm{k_q}\bar{\tau}_0\mathrm{[BQ]} \qquad \text{eq. 4.1}$$

$$\langle\tau_0\rangle/\langle\tau\rangle = 1 + \mathrm{K_D[BQ]} \qquad \text{eq. 4.2}$$

Table 4.2 . Key parameters of photo-induced electron transfer (PET) from PbS QDs to benzoquinone, BQ, including the intensity averaged lifetime, $\bar{\tau}_0$; Stern-Volmer quenching constants, K_{SV} and K_D; bimolecular quenching rate, k_q; quenching efficiency, f_Q and driving force, ΔG.

Complex	$K_{SV}{}^a$/mM^{-1}	$K_D{}^a$/mM^{-1}	$\bar{\tau}_0{}^b$/μs	k_q/M^{-1}·ns^{-1}	k_0/ns^{-1}	f_Q(%)^c	ΔG^d/eV
PbS@OA	4.00	4.00	3.40	1.18	65.2	1.80	-0.05
PbS@pFA	3.55	3.60	3.92	0.91	75.7	1.20	+0.13
PbS@SCF_3	32.10	30.70	4.03	7.97	65.2	12.2	-0.13
PbS@SCH_3	13.10	13.10	3.46	3.79	65.2	5.81	-0.09

a K_{SV} and K_D are the Stern-Volmer quenching constants obtained from steady-state and time-resolved PL experiments. Error bars are the standard error of linear fits.
b $\bar{\tau}_0$ is the intensity averaged lifetime from a bi-exponential fit to the intrinsic lifetime of the PbS QDs given by TCSPC measurements;
c f_Q is being calculated from eq. 4.3.
d ΔG for PET is the difference between the CB of PbS@ligand and LUMO of BQ.

4.3 Discussions

The $-SCF_3$ capping ligand greatly enhances PET from PbS QDs. For both the short $-SCF_3$ and $-SCH_3$ ligands, K_{sv} and K_D are an order of magnitude larger (~31.4 mM^{-1} and 13.1 mM^{-1} respectively) than the long OA and pFA ligands. Compared to the native OA-capped QDs, PbS QDs with a third of the surface $-SCH_3$ and $-SCF_3$ ligands have 2.5 and 7 times larger quenching constants, k_q. This is due to the increased reduction potential of the electron-donating thiolates and the increase in ligand shell permeability. Comparing both short-chain thiolates, we find there is no significant difference in the CB of PbS QDs after partial ligand exchange in solution. Thus, the larger K_{SV} for SCF_3 here is attributed to the change in ligand shell permeability, which is affected by the oleophobicity and increased size of the CF_3 group compared to CH_3. For QD donors with long aliphatic ligands, K_{SV} for PbS@OA and PbS@pFA are 4.00 mM^{-1} and 3.60 mM^{-1} respectively. K_{SV} for PbS@pFA is 10% lower than PbS@OA due to its CB being stabilized by the more electron-withdrawing pFA ligand shell.

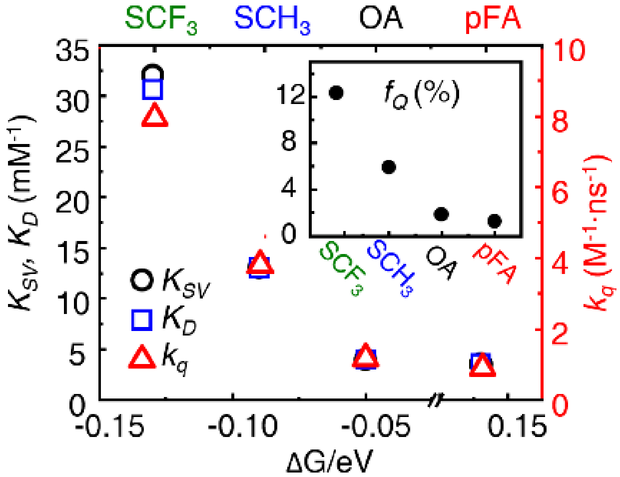

Fig. 4.5 Stern-Volmer constants from the quenching of PbS@ligand by benzoquinone (BQ) provide K_{SV} (red circle) and K_D (black square) from steady-state and TCSPC photoluminescence (PL) quenching experiments respectively. The bimolecular quenching constant, k_q (blue triangle) is also plotted vs. ΔG, the driving force for photoinduced electron transfer from the PbS@ligand QD donors. The inset plots the collisional quenching efficiency, f_Q vs. surface ligand.

To quantify the electron transfer, the bimolecular quenching rate constant, k_q, is calculated from eq. 4.1. Fig. 4.5 shows that the thermally activated k_q is proportional to the driving force, $-\Delta G$, for PET (Table 4.2), given by the difference between the conduction band of the QDs and the LUMO of BQ. However, to compare the permeabilities of the mixed monolayers here, it is useful to compare the collisional quenching efficiency, f_Q (inset Fig. 4.5 or Fig. 4.5) defined in eq. 4.3:

$$f_Q = k_q / k_0 \qquad \text{eq. 4.3}$$

Where k_0 is the diffusion-limited rate constant, calculated from the Smoluchowski equation (eq. 7.18).[37] f_Q takes into account the driving force for PET, the steric barrier posed by the QD's ligand shell, and the fact that the BQ acceptor and QD donor must collide in solution for PET to occur. After replacing 28% OA with -SCH_3 or -SCF_3, f_Q increases from 0.021 to 0.078 and 0.152 respectively, as these short ligands promote wavefunction overlap between the PbS QD and BQ. Comparing PbS@OA with PbS@pFA, f_Q = 0.018 and 0.012 respectively. This decrease of collisional quenching efficiency is partially due to the lower solubility of BQ in pFA compared to the OA ligand shell. In other words, the ligand shell is an effective dynamic barrier for charge transfer to the surrounding BQ quenchers in solution. Weinberg et al. also report a decrease in PET for PbS QD donors in the presence of partially fluorinated ligands.[47]

4.4 Conclusion

We have demonstrated that as artificial molecules, quantum confined semiconductor nanocrystals respond to the electronegativity and oleophobicity of fluorine in very much the same way that pure molecular systems would. The perfluorohexadecanoic ligand here stabilizes the band offsets of the PbS QDs, increasing its work function by ≤1.0 eV and thus decreasing its efficacy as a PET donor. The trifluoromethanethiolate ligand, -SCF_3, like its short methanethiolate -SCH_3 counterpart, enhances the ligand shell permeability of the QD to the benzoquinone quencher, resulting in Stern–Volmer quenching constants that are 1 order of magnitude higher. Both fluorinated ligands modify the energetics of the ground and excited dipoles, resulting in a larger Stokes shift compared to those of hydrocarbon-based ligands, and an unprecedented blue shift in the absorption maxima that can be explained by a change in the dielectric environment. This work illustrates that fluorination is a viable route for controlling the bandgap, band offsets, and ligand shell permeability of QDs. Complete replacement of the long, insulating, native OA ligands with shorter fluorinated ligands will allow the energy levels of QDs to be controlled via simple solution-based methods. Ligand length and oleophobicity will allow the interparticle distance and interactions to be modulated. These structural and electronic changes can potentially enhance electronic coupling in a thin film and may lead to QD-based optoelectronic devices with improved metrics.

4.5 Notes and References

1. Erwin SC, *et al.* Doping semiconductor nanocrystals. *Nature* 2005, 436(7047): 91-94.

2. Chakraborty P, *et al.* Kinetics of Isovalent (Cd2+) and Aliovalent (In3+) Cation Exchange in Cd1–xMnxSe Nanocrystals. *J Am Chem Soc* 2016, 138(39): 12885-12893.

3. Nag A, *et al.* Metal-free Inorganic Ligands for Colloidal Nanocrystals: S2–, HS–, Se2–, HSe–, Te2–, HTe–, TeS32–, OH–, and NH2– as Surface Ligands. *J Am Chem Soc* 2011, 133(27): 10612-10620.

4. Kramer IJ, *et al.* The Architecture of Colloidal Quantum Dot Solar Cells: Materials to Devices. *Chem Rev* 2014, 114(1): 863-882.

5. Greaney MJ, *et al.* Improving Open Circuit Potential in Hybrid P3HT:CdSe Bulk Heterojunction Solar Cells via Colloidal tert-Butylthiol Ligand Exchange. *ACS Nano* 2012, 6(5): 4222-4230.

6. Yaacobi-Gross N, *et al.* Molecular control of quantum-dot internal electric field and its application to CdSe-based solar cells. *Nat Mater* 2011, 10: 974.

7. Katz HE, *et al.* A soluble and air-stable organic semiconductor with high electron mobility. *Nature* 2000, 404: 478.

8. Tang ML, *et al.* Ambipolar, High Performance, Acene-Based Organic Thin Film Transistors. *J Am Chem Soc* . 2008, 130(19): 6064-6065.

9. Sakamoto Y, *et al.* Perfluoropentacene: High-Performance p−n Junctions and Complementary Circuits with Pentacene. *J Am Chem Soc* . 2004, 126(26): 8138-8140.

10. Williams JH. The molecular electric quadrupole moment and solid-state architecture. *Acc. Chem.* 1993, 26(11): 593-598.

11. Williams JH, *et al.* Structure of the Lowest Temperature Phase of the Solid Benzene–Hexafluorobenzene Adduct. *Angew Chem Int Ed Engl* 1992, 31(12): 1655-1657.
12. Liang T, *et al.* Introduction of fluorine and fluorine-containing functional groups. *Angew Chem Int Ed Engl* 2013, 52(32): 8214-8264.

13. Bella F, *et al.* Improving efficiency and stability of perovskite solar cells with photocurable fluoropolymers. *Science* 2016, 354(6309): 203-206.

14. Hines MA, *et al.* Colloidal PbS Nanocrystals with Size-Tunable Near-Infrared Emission: Observation of Post-Synthesis Self-Narrowing of the Particle Size Distribution. *Adv, Mater* 2003, 15(21): 1844-1849.

15. Mahboub M, *et al.* Triplet Energy Transfer from PbS (Se) Nanocrystals to Rubrene: the Relationship between the Upconversion Quantum Yield and Size. *Adv Funct Mater* 2016, 26(33): 6091-6097.

16. Sagar LK, *et al.* PbS/CdS Core/Shell Quantum Dots by Additive, Layer-by-Layer Shell Growth. *Chem Mater* 2016, 28(19): 6953-6959.

17. Albrecht C. Joseph R. Lakowicz: Principles of fluorescence spectroscopy, 3rd Edition. *Anal. Bioanal. Chem* 2008, 390(5): 1223-1224.

18. Lippert E. Spektroskopische Bestimmung des Dipolmomentes aromatischer Verbindungen im ersten angeregten Singulettzustand. *Zeitschrift für Elektrochemie, Berichte der Bunsengesellschaft für physikalische Chemie* 1957, 61(8): 962-975.

19. Mataga N, *et al.* Solvent Effects upon Fluorescence Spectra and the Dipolemoments of Excited Molecules. *Bull. Chem. Soc. Jpn.* 1956, 29(4): 465-470.

20. Abjean R, *et al.* Refractive index of carbon tetrafluoride (CF4) in the 300-140 nm wavelength range. *Nuclear Instruments and Methods in Physics Research Section A: Accelerators, Spectrometers, Detectors and Associated Equipment* 1990, 292(3): 593-594.

21. Gee N, *et al.* Relative permittivities of 10 organic liquids as functions of temperature. *J. Chem. Thermodyn.* 1993, 25(4): 549-554.

22. Rollefson R, *et al.* Index of Refraction of Methane in the Infra-Red and the Dipole Moment of the CH Bond. *Phys. Rev* 1940, 57(8): 710-717.

23. Straty G, *et al.* Dielectric constant and polarizability of saturated and compressed fluid methane. *Cryogenics* 1973, 13(12): 712-715.

24. Banus J, *et al.* 12. The heterolytic fission of the carbon-iodine bond in trifluoroiodomethane. *J. Chem. Soc. (Resumed)* 1951(0): 60-64.

25. Champion JV, *et al.* Electro-optic Kerr effect in n-alkane liquids. *J. Chem. Soc. Faraday Trans* 1970, 66(0): 2671-2680.

26. Haynes WM. *CRC Handbook of Chemistry and Physics, 95th*. CRC press: Boca Raton, 2014.

27. Lifanova N, *et al.* The molecular structure of certain perfluorocarbons based on their equilibrium dielectric properties. *Russ. J. Phys. Chem. A.*1992, 66(1): 125-126.

28. Liu X, *et al.* Molecular Origins of Optoelectronic Properties in Coumarin Dyes: Toward Designer Solar Cell and Laser Applications. *J. Phy. Chem. A* 2012, 116(1): 727-737.

29. Weinberg DJ, *et al.* Control of the Redox Activity of Quantum Dots through Introduction of Fluoroalkanethiolates into Their Ligand Shells. *J Am Chem Soc* . 2016, 138(7): 2319-2326.

30. Brown PR, *et al.* Energy Level Modification in Lead Sulfide Quantum Dot Thin Films through Ligand Exchange. *ACS Nano* 2014, 8(6): 5863-5872.

31. Tyrra W, *et al.* A new synthesis of trifluoromethanethiolates—characterization and properties of tetramethylammonium, cesium and di (benzo-15-crown-5) cesium trifluoromethanethiolates. *J. fluor. chem.* 2003, 119(1): 101-107.

32. Yin G, *et al.* Trifluoromethylthiolation of Aryl Iodides and Bromides Enabled by a Bench-Stable and Easy-To-Recover Dinuclear Palladium(I) Catalyst. *Angew Chem Int Ed* 2015, 54(23): 6809-6813.

33. O'Donnell A, *et al.* Particle−Particle Interactions and Chain Dynamics of Fluorocarbon and Hydrocarbon Functionalized ZrO2 Nanoparticles. *Langmuir* 2008, 24(6): 2465-2471.

34. Luther JM, *et al.* Structural, Optical, and Electrical Properties of Self-Assembled Films of PbSe Nanocrystals Treated with 1,2-Ethanedithiol. *ACS Nano* 2008, 2(2): 271-280.

35. Hudson RL. Infrared spectra and band strengths of CH3SH, an interstellar molecule. *Phys. Chem. Chem. Phys.* 2016, 18(36): 25756-25763.

36. Haas A, *et al.* Darstellung neuer fluorierter Sulfenylhalogenide und Sulfenylpseudohalogenide. *Chem. Ber.* 1968, 101(8): 2609-2616.

37. Aruda KO, *et al.* Temperature-Dependent Permeability of the Ligand Shell of PbS Quantum Dots Probed by Electron Transfer to Benzoquinone. *J Phys Chem Lett.* 2015, 6(14): 2841-2846.

38. Boehm AM, *et al.* A new photon source for ultraviolet photoelectron spectroscopy of organic and other damage-prone materials. *Org Electron* 2017, 41: 9-16.

39. Miller EM, *et al.* Revisiting the Valence and Conduction Band Size Dependence of PbS Quantum Dot Thin Films. *ACS Nano* 2016, 10(3): 3302-3311.

40. Kroupa DM, *et al.* Tuning colloidal quantum dot band edge positions through solution-phase surface chemistry modification. *Nat Commun* 2017, 8: 15257.

41. Kim G-H, *et al.* High-Efficiency Colloidal Quantum Dot Photovoltaics via Robust Self-Assembled Monolayers. *Nano Letters* 2015, 15(11): 7691-7696.

42. Alloway DM, *et al.* Interface Dipoles Arising from Self-Assembled Monolayers on Gold: UV−Photoemission Studies of Alkanethiols and Partially Fluorinated Alkanethiols. *J Phys Chem B* 2003, 107(42): 11690-11699.

43. Rusu PC, *et al.* Dipole Formation at Interfaces of Alkanethiolate Self-assembled Monolayers and Ag(111). *J Phys Chem C* 2007, 111(39): 14448-14456.

44. Rusu PC, *et al.* Surface Dipoles and Work Functions of Alkylthiolates and Fluorinated Alkylthiolates on Au(111). *J Phys Chem B* 2006, 110(45): 22628-22634.

45. Knowles KE, *et al.* Dual-Time Scale Photoinduced Electron Transfer from PbS Quantum Dots to a Molecular Acceptor. *J Am Chem Soc* 2012, 134(30): 12470-12473.

46. Caram JR, *et al.* PbS Nanocrystal Emission Is Governed by Multiple Emissive States. *Nano Letters* 2016, 16(10): 6070-6077.

47. Lian S, *et al.* Sub-Picosecond Photoinduced Hole Transfer from a CdS Quantum Dot to a Molecular Acceptor Bound Through an Exciton-Delocalizing Ligand. *ACS nano* 2016, 10(6): 6372-6382.

5 Chapter 5 Spin-coated fluorinated PbS QD superlattice thin film with high hole mobility

5.1 Introduction

The large surface area intrinsic to semiconductor quantum dots (QDs), where approximately one-third of the atoms/ ions are on its exterior, makes the prospect of tuning the ligand shell to modify its physical and electronic properties appealing. Ideally, short ligands that can promote electronic coupling between particles in thin film would be used to engineer the surface energetics and electronic energy levels of QDs to induce mesoscale order. Furthermore, in terms of ligand selection, these short ligands should not compromise the colloidal stability of QD solutions that allow solution processed thin films to be fabricated.

Various ligand treatments on QD thin films have been performed to promote electronic coupling and passivate trap states. Treatments include elemental indium[1, 2], organic halides[3-6], metal halides[7-9] and pseudohalides[10-12]. Benzenedithiol or other aliphatic thiols like mercaptopropionic acid (MPA) are routinely used to cross-link QD thin films because of their natural affinity with the QD chalcogenide lattice[13-17]. Thiols are necessary because QDs are synthesized with long-chain, aliphatic chains that confer colloidal stability at the expense of conductivity. Thiol treatment results in a thin film that allows charge to percolate, typically via a hopping mechanism. A variable range hopping model was used by Law et al to explain the lack of correlation between transistor mobility and sample polydispersity. Law et al postulate that holes or electrons hop through states on the largest QDs in the thin film[18]. Others have used halides or pseudohalides[6, 10, 19] to draw the QDs closer together. In 2012, the Sargent group used $CdCl_2$ to minimize mid-gap states for record QD solar cell PCEs of 7%[16]; in 2016, they used methyl ammonium iodide for the current record of 10.6% certified PCE[4]. Last year in 2018, they showed that a PbI_2 matrix improved the the PCE to 12%[20]. Two reports of QD TFTs, one from the Kagan group using thiocyanate[2], and one from the Talapin group using $In_2Se_4^{2-}$ ligands[21], show increasing mobility with decreasing temperature, observations associated with band transport[22]. However, the high mobilities measured were shown in the context of Marcus theory to be due to phonon-assisted hoping because the calculated electronic coupling energy was much smaller than the reorganization energy[23].

Notwithstanding the fact that the QD-organic interface is complicated by dangling bonds, unpassivated surface sites, curvature induced strain, etc., we chose perfluorocarbons as the short ligands. Here, the compact fluorinated ligands are expected to facilitate wavefunction overlap between the QDs for efficient energy and charge transfer by replacing the original long insulating ligands. In addition, the electron withdrawing CF_3 group may be able to tune the band edges of the QDs to introduce a depletion region to promote the drift of charge carriers under short circuit conditions in a solar cell. The resultant band alignment might minimize recombination of photo-generated electrons at the anode. Both these factors should increase the photocurrent of the QD solar cell. This was the basis of a 2013 report by the Bawendi group where a combination of iodide and ethanethiol were used to control the band alignment in a PbS QD solar cell[24].

5.2 Data and Discussion

5.2.1 Fabrication and characterization of conducting PbS superlattice film

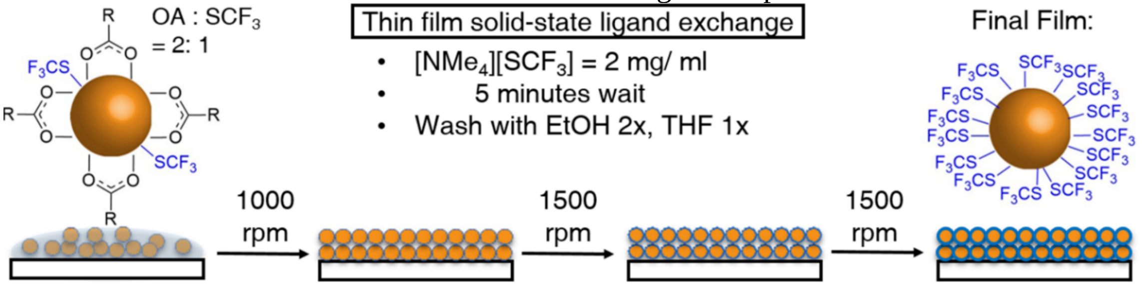

Fig. 5.1 Partially ligand exchanged PbS QDs were spin-coated on bottom contact transistor substrates. Ligand exchanges were performed on the resultant thin film to completely install the SCF$_3$ ligand and induce long range order. OA = oleic acid.

Here, we report a spincoating method to fabricate electronically coupled PbS QD superlattice thin films with the trifluoromethanethiolate ligand ($\ominus$SCF$_3$).[25] $\ominus$SCF$_3$ was chosen because it is a short ligand (<0.2 nm) that could potentially induce electronic wavefunction overlap in thin film. As shown in Fig 5.1, partially ligand-exchanged colloidal PbS QDs with a ratio of native oleic acid (OA) to $\ominus$SCF$_3$ ligands of 2:1 were spin coated in air-free conditions on bottom contact patterned substrates coated with self-assembled monolayers (SAMs) 3-mercaptopropyl trimethoxysilane (3-MPTMS) or 1H,1H,2H,2H-perfluorodecyltriethoxysilane. Two consecutive ligand exchanges on this spin-coated thin film were performed by soaking the existing thin film in an acetonitrile solution of the [NMe$_4$][SCF$_3$] salt. Excess ligand was removed by spin-coating, followed by three washing steps: twice with ethanol and finally with tetrahydrofuran. ATR-IR measurements of PbS–SCF$_3$ verify the complete removal of OA after two cycles of ligand exchange in thin film.[25]

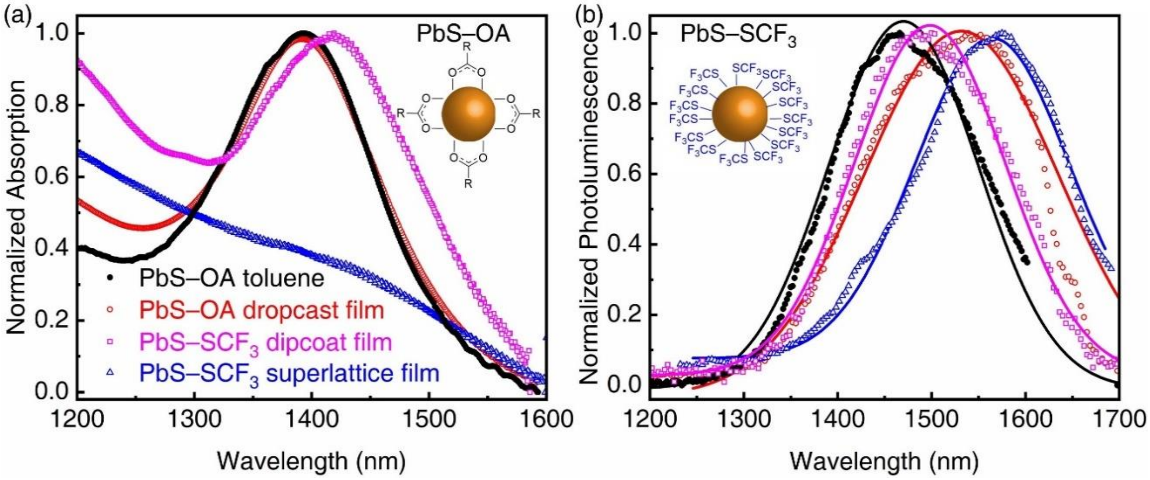

Fig. 5.2 The absorption and photoluminescence (PL) of the PbS QDs. The original oleic acid capped PbS QDs in toluene (black filled circles) were either dropcast to make a thin film (red open circle), or were first partially ligand exchanged, then spin-coated on bottom contact substrates for dipcoating in $[\mathrm{NMe_4}][\mathrm{SCF_3}]$ solution (magenta squares) or completely ligand exchanged with $\ominus\mathrm{SCF_3}$ as described in Fig 5.1 (blue triangle).

The PbS–$\mathrm{SCF_3}$ thin film fabricated as illustrated in Fig 5.1 has improved ensemble homogeneity compared to the original OA capped PbS QDs, PbS–OA, as reflected by the width in their photoluminescence (PL) peaks. When PbS–OA QDs in toluene (filled black circles, Fig 5.2), are dropcast to make a thin film (open red circles, Fig 5.2), no change in the absorption maxima was observed since the dielectric environment created by oleic acid is similar to toluene. However, a red shift of 60 nm in the PL of the thin film compared to toluene was observed. This was previously observed by Kagan et al and explained as Forster energy transfer from small QDs to larger QDs within the ensemble.[26] In contrast, the PL of superlattice thin film (blue triangles, Fig 5.2) is even more red-shifted than the PbS–OA dropcast film, likely due to the fact that the QD has an additional layer of thiolate from the $\ominus\mathrm{SCF_3}$ ligand, and as we will show, enhanced electronic coupling. No absorption maxima was observed in this superlattice thin film, perhaps due to the low optical density of the 40 nm thin film.

Alternatively, Loi et al propose that a decreased oscillator strength in PbS QD thin films stem from an altered dielectric environment or a broadening due to inhomogeneous electronic coupling.[27] As a control, we dip-coated a spincoated PbS–OA QD thin film in [NMe$_4$][SCF$_3$] in acetonitrile solution to completely replace OA with $\ominus$SCF$_3$. From previous work, this dipcoating should give an amorphous thin films due to an isotropic contraction as the long OA are replaced with the short $\ominus$SCF$_3$ ligands.[28-30] To our surprise, from GISAXS data, this dipcoated film also shows long range order, albeit with reduced crystallinity. The absorption maxima of this dipcoated PbS–SCF$_3$ film (magenta squares, Fig 5.2) red-shifted more than 20 nm compared to PbS–OA due to the extra layer of thiolate from $\ominus$SCF$_3$ on QD surface. However, compared to the PL of the dropcast PbS–OA film, the PL of dropcast PbS–SCF$_3$ film is blue shifted. Most noticeably, the full width of half maximum (FWHM) of both PbS–SCF$_3$ thin films are 160 ± 2nm, smaller than the 207± 4nm FWHM of the PL of the dropcast PbS−OA. We assign this narrow FWHM to an improved homogeneity of QDs where the $\ominus$SCF$_3$ ligand narrows the size and shape distribution in the original PbS QDs. A similar argument has been put forth by the Sargent group when PbI$_2$ monolayers on PbS QDs were used to fabricate state-of-the-art QD solar cells.[20] In their work, the PbI$_2$ matrix increases the carrier diffusion length by decreasing the spread in energy levels between QDs via increasing particle homogeneity.

In order to characterize the long-range order in the PbS–SCF$_3$ thin films, GISAXS was performed. To determine the unit cell parameters, diffraction patterns were simulated using GIXSGUI[31] and were fit iteratively to achieve agreement between simulated and experimental peaks. The experimentally obtained diffraction pattern overlaid with simulated is shown in Fig. 7.26. Through this procedure, we determined a cubic lattice with a lattice constant of 5.8 nm. We note that the specific space group and symmetry cannot be determined due to the limited number of peaks. The peak indexing results are shown in Fig 5.3a, from which we can infer there are two orientations of the cubic lattice. The dominant orientation occurs with the (101) plane parallel to the substrate is indexed in white. A second orientation with the (111) plane parallel to the substrate is indexed in red and exhibits weaker intensity indicating this orientation occurs less frequently within the sample. Seen in Fig 5.3b, annealed samples appear to have the same cubic structure, though the weaker peaks from the (111) orientation seem to have disappeared. At the same time, the peak widths were reduced. Both observations indicate increased out of plane alignment of the crystalline domains after annealing, which may contribute to enhanced charge transport discussed later. In comparison, the dipcoated samples exhibit a dominant (111) orientation (Fig 5.3c, e) instead of the (101) orientation seen from spincoating (Fig 5.3b, d). This becomes clear in Fig. 7.27 when comparing the fittings for both orientations shows close agreement with the (111) orientation. Further, we see from the normalized intensities in Fig. 7.28 there appears to be a reduction in crystallinity from the nonannealed spincoated to the dipcoated samples.

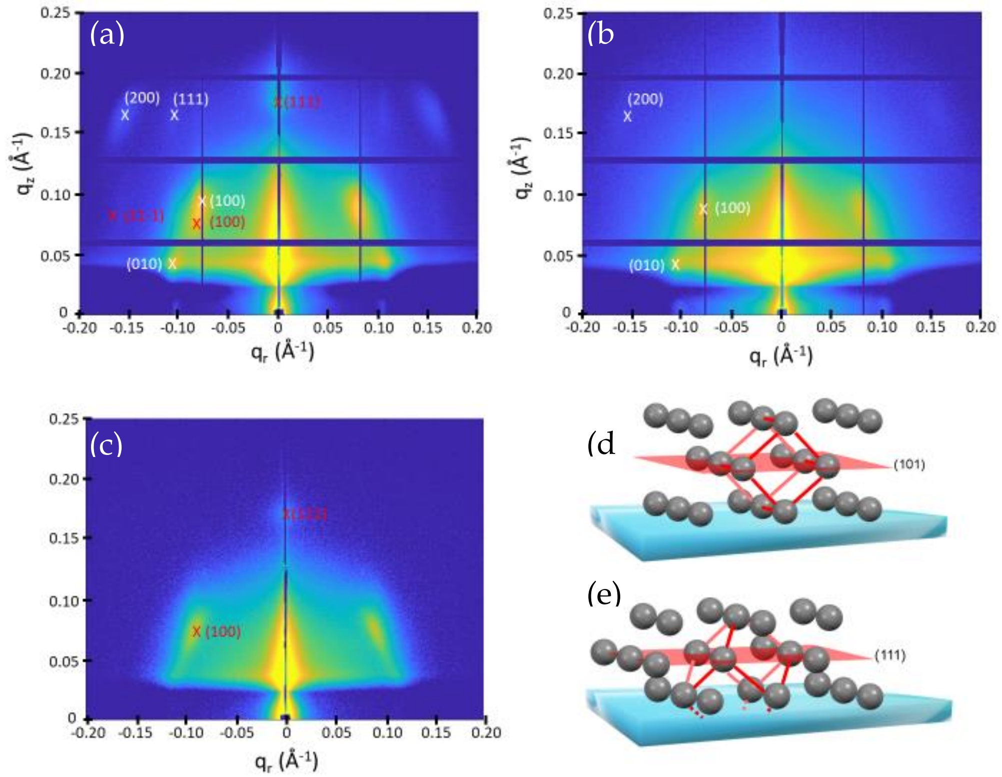

Fig. 5.3 GISAXS for nonannealed (a) and annealed (b) spincoated and nonannealed dipcoated (c) PbS–SCF_3 thin films fabricated as illustrated in Fig 5.1 shows a cubic lattice with a lattice constant = 5.8 nm. The diffraction peaks from the orientation with (101) parallel to the substrate are indexed in white and the peaks from the orientation with (111) parallel to the substrate are indexed in red. Note that for the (111) orientation, the (100) peak also appears at a similar position as the case of (101) orientation (Fig. 7.25). All of the diffraction patterns shown were taken at X-ray incident angle of 0.2°. The (101) (d) and (111) (e) lattice orientations with respect to the substrate showing the packing and the unit cell orientation indicated in red.

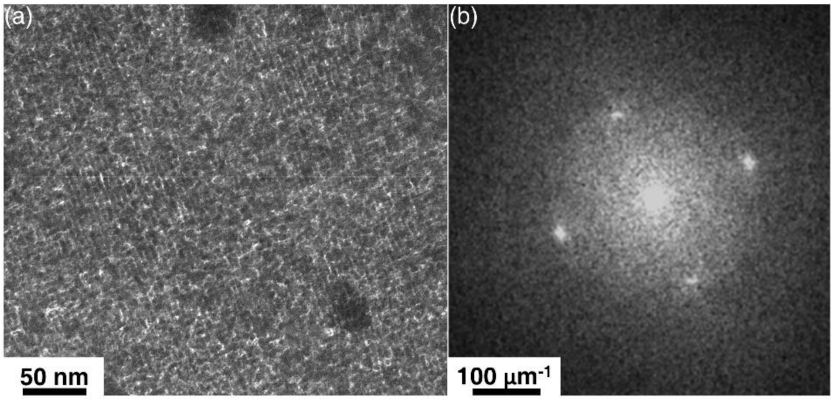

Fig. 5.4 (a) Transmission electron micrographs show a superlattice with distance between two QDs of 5.6 ± 0.5 nm. The fast-Fourier transfer (FFT) of the real space image gives two pairs of peaks with ratio of the distances between the peaks ~1.5, close to the expected 1.41 for the (101) plane perpendicular to the substrate. More TEM images with their FFTs are in the supporting information (Fig. 7.30 and Fig. 7.29)

Transmission electron microscopy (Fig 5.4) confirms the superlattice structure of this PbS–SCF_3 thin film. To recreate the same PbS superlattice for TEM, the PbS QD thin film was fabricated on silica terminated TEM grids as illustrated in Fig 5.1. The 50 × 50 μm silica windows are approximately similar in dimensions as the channel lengths in the bottom-contact transistors used here. Fig 5.4 shows the real space TEM image on the left and its associated FFT on the right. Alignment of the PbS QDs can be directly seen in Fig 5.4a. The interparticle distance given by TEM is 5.6 ± 0.5 nm, close to the 5.8 nm given by GISAXS, slightly larger than the original diameter of the PbS QDs given by their electronic absorption maxima of 5.1 nm. Atomic force microscopy (AFM, Fig. 7.31) shows the resultant thin films have thicknesses around 25 – 30 nm, corresponding to 4 – 5 layers of PbS QDs.

5.2.2 Electronic properties of superlattice film

The superlattice formation here is unexpected, especially since the thin film was spin-coated. In fact, dipcoating typically produces amorphous QD films[28-30]. While both showed long range order, in contrast to the spin-coated thin films, the dip-coated sample showed a lot of cracks

(Fig. 7.31) in the PbS–SCF$_3$ film since the original long OA ligand of QDs are abruptly removed during ligand exchange. Here, the oleophobic –CF$_3$ shell, in combination with our thin-film based ligand exchange facilitates close packing of QDs by inducing long-range order. Since the PbS QDs have a fluorinated shell, we hypothesized that they would preferentially wet a perfluoro-capped surface. Interestingly, under the same spin-coating conditions, a slightly thicker PbS–SCF$_3$ thin film was deposited on the perfluoro SAM (~50 nm compared to 40 nm) with hole mobilities as high as 0.085 cm^2/ Vs. Moreover, there is no significant change in the hole mobility of this superlattice TFT with storage in a nitrogen glovebox for 7 months.

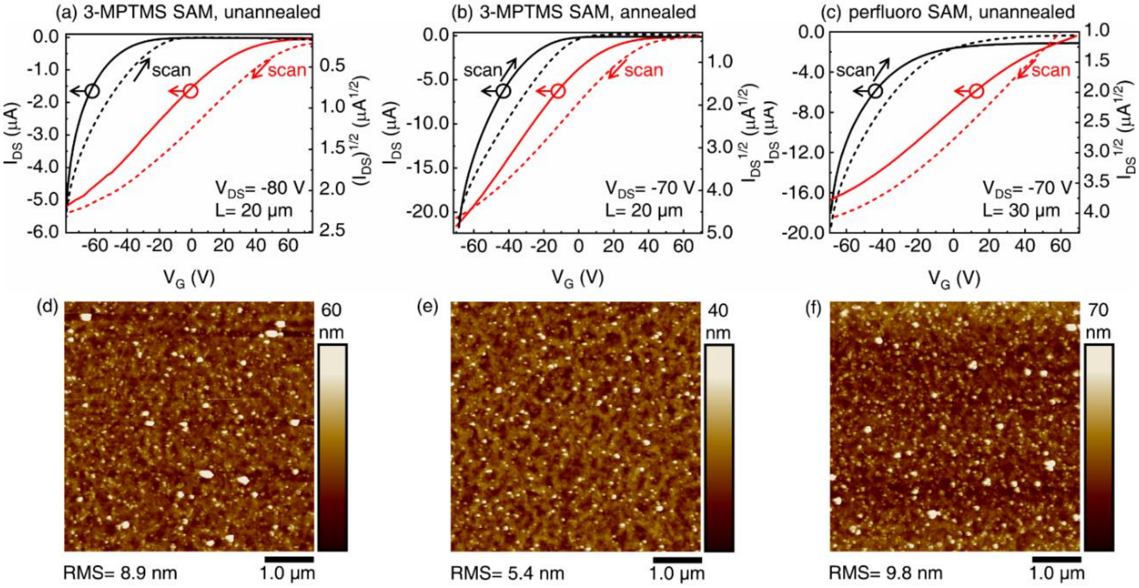

Fig. 5.5 (a–c) Representative transfer curves from PbS–SCF$_3$ QD superlattice thin films. The red and black traces represent scanning towards negative and positive gate voltages (V_G) respectively. (d–f) Corresponding atomic force microscope (AFM) images. (a, b, d and e) represent TFTs with dielectric modified with 3-MPTMS, while (c and f) have the dielectric modified with a perfluoro SAM. Samples b and e have been annealed at 60ºC.

To investigate the effect of long-range order on the transport properties of this PbS–SCF$_3$ thin film, current-voltage transistor measurements were performed in air-free conditions. The bottom contact devices were treated with the thiol-based 3-MPTMS SAM and 1H,1H,2H,2H-Perfluorodecyltriethoxysilane (see experimental section for details). PbS–SCF$_3$ thin films give only p-type transistors with hole mobilities averaging between 0.002–0.040 cm^2/Vs. On one hand, the PbX (X=S, Se) QDs functionalized with insulating, long-chain carbons show no charge transport in thin film; on the other extreme, PbX (X=S, Se) QDs functionalized with EDT or short-chain linear amines (e.g. butylamine) give thin films where the particles are fused together[27, 32,33]. This particle necking has been captured by TEM and give mobilities similar or slightly lower than those reported here. TFT mobilities were extracted from transfer curves (Fig. 5.5, a – c) and summarized in Table 5.1. The on/ off ratios, I_{ON} / I_{OFF} were low ~10^2. With the 3-MPTMS SAM, we introduced an annealing step at 60ºC. Corresponding to the observation that GISAXS indicates a larger proportion of crystallites oriented out-of-plane after annealing, AFM shows that annealing decreases the RMS roughness of the thin film from 8.9 nm to 5.4 nm, as shown in Fig. 5.5d and Fig. 5.5e. This is accompanied by an increased ideality in the transfer curves. As can be seen, the square root of the source-drain current, I_{DS}, (black dotted line) has only one slope in Fig 5b, compared to the rest of the transfer curves where at least two slopes are observed (Fig. 7.36).

Table 5.1 Summary of transistor performance, including the maximum and average mobilities, μ_{MAX} and μ_{AVE}, the threshold voltage, V_T, and the on/ off ratios, I_{ON} / I_{OFF} corresponding to PbS QD TFTs in Fig. 5.5.

Pretreatment	3-MPTMS SAM				perfluoro SAM	
Posttreatment	unannealed		annealed		unannealed	
Channel length/ μm	20		20		30	
Scan towards	+V_G	-V_G	+V_G	-V_G	+V_G	-V_G
μ_{MAX} [cm^2/ Vs]	0.080	0.002	0.079	0.012	0.085	0.012
μ_{AVE} [cm^2/ Vs]	0.042	0.002	0.035	0.010	0.018	0.004
V_T [V]	–10	+60	–10	+50	+10	+70
I_{ON} / I_{OFF}	400	100	200	200	20	40

The presence of hole trap states below the valence band, outside the bandgap of the QDs, possibly induced by charge transfer from the highest occupied molecular orbital (HOMO) of the thiolate ligands may explain the non-ideality in these TFT curves. Fig 5.6a shows the conduction and valence bands of the PbS–SCF_3 superlattice thin film measured by UPS in comparison with the HOMO of the [NMe_4][SCF_3] precursor given by cyclic voltammetry. The UPS data was used to determine the valence band energy by fitting the leading edge of the spectra with a parabola and taking the intersection of this parabola with the background as the valence band energy. This procedure was used owing to the low density of states (DOS) at the band edge, which can lead to inaccurate valence band energies when the data is fit on a linear scale.[34] The energy of the conduction band (CB), E_C is approximated by adding the electronic transport gap, E_G of the material to the valence band maximum. E_G is calculated based on the optical absorption and Coulombic stabilization energy (Table 7.15 and Fig. 7.32).[30] The alignment of these energy levels suggests that hole traps in the PbS–SCF_3 thin film might very well be introduced by the thiolates anchoring the CF_3 ligands to the QD surface. As shown in Fig 5.6b, bias stress measurements indicate the presence of hole traps in this thin film. Fig 5.6 shows representative data from the annealed PbS–SCF_3 thin film on 3-MPTMS (Fig. 5.5b/ e). In Fig 5.6b, with fixed source-drain voltage, V_{DS}= –70 V, the hole current decreases with time as the gate voltage, V_G, is varied between –30 to –70 V. At positive V_G, the source-drain current, I_{DS}, appears to increase. This suggests that holes are thermally promoted from traps below the valence band, as drawn in Fig 5.6a. These hole traps also explain the hysteresis in the TFT curves. Both Fig. 5.5 a – c show that starting the transfer curve from negative V_G towards positive V_G results in more ideal TFTs. Similarly, Fig 5.6 c-d show that saturation only occurs when sweeping the output curve from negative V_{DS} towards positive V_{DS}, not when V_{DS} is swept in the opposite direction. Bias stress curves for other TFTs are in the SI. The bias stress curves reveal that the dielectric treatment has no effect on the evolution of the current over time (see Fig. 7.33). The fact that the dielectric treatment does not affect the general shape of the transfer, output or bias stress curves supports our hypothesis that the most detrimental traps are intrinsic to the QDs and introduced by the ligand exchange process.

As a comparison, we also investigated the mobility of the dipcoated PbS–SCF_3 thin film. The dipcoated PbS–SCF_3 TFTs have hole mobilities as high as 0.025 cm^2/ Vs, average mobilities ranging from 0.002–0.007 cm^2/ Vs, and on and off ratio, I_{ON}/I_{OFF} ~10^2. The lower maximum mobility correlates with the macroscopic cracks and decreased crystallinity of the superlattice film compared to the spin-coated sample. The hole mobilities of both the dipcoated and spin-coated PbS–SCF_3 thin films confirm that $\ominus$$SCF_3$, like other widely investigated short ligands, EDT[28] or formic acid[35] greatly improve PbS QD thin film transport. Electronic coupling between the QDs is enhanced after replacing the insulating OA ligands on the QD surface as the interparticle distances are decreased to less than 1 nm.

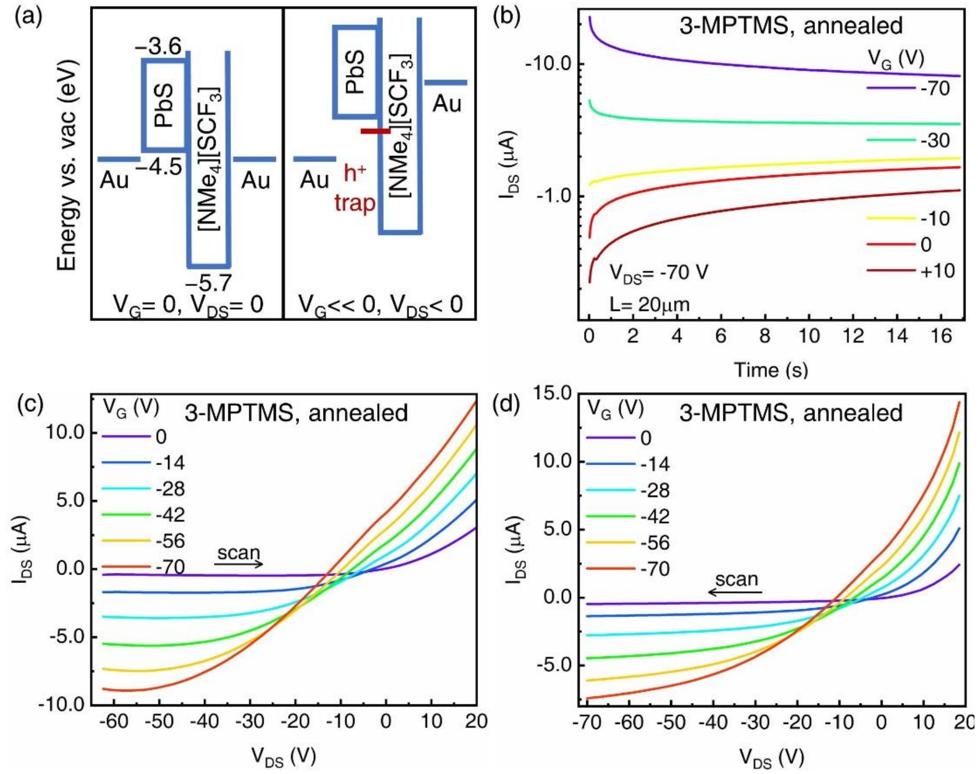

Fig. 5.6 (a) Energy diagram of the PbS−SCF_3 QD thin film compared to the highest occupied molecular orbital (HOMO) of $[NMe_4][SCF_3]$. The valence band (VB) was obtained by ultraviolet photoelectron spectroscopy (UPS) while the HOMO of $[NMe_4][SCF_3]$ was obtained in acetonitrile by cyclic voltammetry (Fig. 7.23). (b) Bias stress curves for annealed PbS–SCF_3 QD thin films spin-coated on 3-MPTMS treated dielectric where $V_{DS} = -70$ V is held as the gate voltage, V_G is varied. L = 20 µm. (c) and (d) Typical output curves of annealed PbS–SCF_3 QD TFT with 3-MPTMS treatment on the thermal oxide dielectric. Output curves for unannealed PbS–SCF_3 QD TFT with 3-MPTMS treatment or with perfluoro SAM are in the supporting information (Fig. 7.34).

5.3 Conclusion

We show for the first time that a simple spincoating method can be used to fabricate fluorinated PbS QD superlattice thin films with high hole mobility. The PbS–SCF_3 TFTs form p-type transistors with mobility as high as 0.085 cm^2/ Vs and on/ off ratios, I_{ON} / I_{OFF} ~10^2. Photoluminescence of these thin films indicates the ⊖SCF_3 shell narrows the ensemble QD size and shape distribution while preserving quantum confinement. Long-range order is confirmed with GISAXS and TEM measurements. Superlattice formation suggests that this short-fluorinated shell facilitates close-packing of the PbS QDs and induces long-range order. Unfortunately, the thiolate ligands introduce traps below the valence band edge which are detrimental to charge transport. Alternative methods to fluorinate QDs without introducing such trap states may create the physical conditions for necessary for electronic mini-bands.

5.4 Future Plans: [NMe$_4$][CF$_3$COO] and CF$_3$COONa applied as capping ligands

As previous work indicates that -CF$_3$ help PbS QDs with periodical alignment in thin film with simple spincoating method, while the carrier mobility is not as large as we expected. Serious hole trap is one reason, which sterns from the QDs itself. We assign the big hole trap to hole trapping group '-S'. Moreover, photon upconversion experiment with different ligand loading on PbS QDs surface indicates that -COOH gives less defects after ligand exchange. Here, we tried [NMe$_4$][CF$_3$COO] as short ligand to functionalize PbS QDs and test the electronic properties. Ambipolar properties have been shown as

With COO- anchoring group, on and off ratio increase to 1000. Moreover, the hole carrier mobilities are as high as 0.8 cm^2/Vs and electron mobility are as high as 1.5 cm2/Vs. The binding groups effect are still under investigation.

5.5 Notes and References

1. Straus DB, *et al.* Increased Carrier Mobility and Lifetime in CdSe Quantum Dot Thin Films through Surface Trap Passivation and Doping. *J Phys Chem Lett.* 2015, 6(22): 4605-4609.

2. Choi JH, *et al.* Bandlike Transport in Strongly Coupled and Doped Quantum Dot Solids: A Route to High-Performance Thin-Film Electronics. *Nano Lett* 2012, 12(5): 2631-2638.

3. Crisp RW, *et al.* Metal Halide Solid-State Surface Treatment for High Efficiency PbS and PbSe QD Solar Cells. *Scientific Reports* 2015, 5.

4. Lan XZ, *et al.* 10.6% Certified Colloidal Quantum Dot Solar Cells via Solvent Polarity-Engineered Halide Passivation. *Nano Lett* 2016, 16(7): 4630-4634.

5. Mongin F, *et al.* Cross-coupling reactions of phenylmagnesium halides with fluoroazines and fluorodiazines. *J. Org. Chem.* 2002, 67(25): 8991-8994.

6. Zhang H, *et al.* Colloidal Nanocrystals with Inorganic Halide, Pseudohalide, and Halometallate Ligands. *Acs Nano* 2014, 8(7): 7359-7369.

7. Tang J, *et al.* Colloidal-quantum-dot photovoltaics using atomic-ligand passivation. *Nat Mater* 2011, 10(10): 765-771.

8. Ip AH, *et al.* Hybrid passivated colloidal quantum dot solids. *Nat Nano* 2012, 7(9): 577-582.

9. Kim GH, *et al.* High-Efficiency Colloidal Quantum Dot Photovoltaics via Robust Self-Assembled Mono layers. *Nano Lett* 2015, 15(11): 7691-7696.

10. Fafarman AT, *et al.* Thiocyanate-Capped Nanocrystal Colloids: Vibrational Reporter of Surface Chemistry and Solution-Based Route to Enhanced Coupling in Nanocrystal Solids. *J Am Chem Soc* 2011, 133(39): 15753-15761.

11. Kovalenko MV, *et al.* Colloidal Nanocrystals with Molecular Metal Chalcogenide Surface Ligands. *Science* 2009, 324(5933): 1417-1420.

12. Nag A, *et al.* Metal-free Inorganic Ligands for Colloidal Nanocrystals: S2-, HS-, Se2-, HSe-, Te2-, HTe-, TeS32-, OH-, and NH2- as Surface Ligands. *J Am Chem Soc* 2011, 133(27): 10612-10620.

13. Fafarman AT, *et al.* Chemically Tailored Dielectric-to-Metal Transition for the Design of Metamaterials from Nanoimprinted Colloidal Nanocrystals. *Nano Lett* 2013, 13(2): 350-357.

14. Ning ZJ, *et al.* Solar Cells Based on Inks of n-Type Colloidal Quantum Dots. *Acs Nano* 2014, 8(10): 10321-10327.

15. Ip AH, *et al.* Infrared Colloidal Quantum Dot Photovoltaics via Coupling Enhancement and Agglomeration Suppression. *Acs Nano* 2015, 9(9): 8833-8842.

16. Ip AH, *et al.* Hybrid passivated colloidal quantum dot solids. *Nat Nanotechnol* 2012, 7(9): 577-582.

17. Kagan CR, *et al.* Building devices from colloidal quantum dots. *Science* 2016, 353(6302).

18. Liu Y, *et al.* Dependence of Carrier Mobility on Nanocrystal Size and Ligand Length in PbSe Nanocrystal Solids. *Nano Lett* 2010, 10(5): 1960-1969.

19. Zhang H, *et al.* Solution-Processed, Ultrathin Solar Cells from CdCl3--Capped CdTe Nanocrystals: The Multiple Roles of CdCl3- Ligands. *J Am Chem Soc* 2016, 138(24): 7464-7467.

20. Xu J, *et al.* 2D matrix engineering for homogeneous quantum dot coupling in photovoltaic solids. *Nat Nanotechnol* 2018, 13(6): 456-462.

21. Lee JS, *et al.* Band-like transport, high electron mobility and high photoconductivity in all-inorganic nanocrystal arrays. *Nat Nanotechnol* 2011, 6(6): 348-352.

22. Talgorn E, *et al.* Unity quantum yield of photogenerated charges and band-like transport in quantum-dot solids. *Nat Nanotechnol* 2011, 6(11): 733-739.

23. Chu IH, *et al.* Charge Transport in a Quantum Dot Supercrystal. *J Phys Chem C* 2011, 115(43): 21409-21415.

24. Chuang CHM, *et al.* Improved performance and stability in quantum dot solar cells through band alignment engineering. *Nat Mater* 2014, 13(8): 796-801.

25. Xia P, *et al.* Surface Fluorination for Controlling the PbS Quantum Dot Bandgap and Band Offset. *Chem Mater* 2018, 30(15): 4943-4948.

26. Kagan CR, *et al.* Electronic Energy Transfer in CdSe Quantum Dot Solids. *Phys Rev Lett* 1996, 76(9): 1517-1520.

27. Balazs DM, *et al.* Electron Mobility of 24 cm(2) V(-1) s(-1) in PbSe Colloidal-Quantum-Dot Superlattices. *Adv Mater* 2018, 30(38): 1802265.

28. Osedach TP, *et al.* Bias-Stress Effect in 1,2-Ethanedithiol-Treated PbS Quantum Dot Field-Effect Transistors. *ACS Nano* 2012, 6(4): 3121-3127.

29. Koleilat GI, *et al.* Efficient, Stable Infrared Photovoltaics Based on Solution-Cast Colloidal Quantum Dots. *ACS Nano* 2008, 2(5): 833-840.

30. Brown PR, *et al.* Energy Level Modification in Lead Sulfide Quantum Dot Thin Films through Ligand Exchange. *ACS Nano* 2014, 8(6): 5863-5872.

31. Jiang Z. GIXSGUI: a MATLAB toolbox for grazing-incidence X-ray scattering data visualization and reduction, and indexing of buried three-dimensional periodic nanostructured films. *J Appl Cryst* 2015, 48(3): 917-926.

32. Moayed MMR, *et al.* High-Performance n- and p-Type Field-Effect Transistors Based on Hybridly Surface-Passivated Colloidal PbS Nanosheets. *Adv Funct Mater* 2018, 28(19): 1706815.

33. Whitham K, *et al.* Charge transport and localization in atomically coherent quantum dot solids. *Nat Mater* 2016, 15(5): 557-563.

34. Miller EM, *et al.* Revisiting the Valence and Conduction Band Size Dependence of PbS Quantum Dot Thin Films. *ACS Nano* 2016, 10(3): 3302-3311.

35. Zarghami MH, *et al.* p-Type PbSe and PbS quantum dot solids prepared with short-chain acids and diacids. *ACS Nano* 2010, 4(4): 2475-2485.

6 Chapter 6 applying [NMe_4][SCF_3] and perfluoro ligands on CdSe NCs surface to tune band offsets

6.1 Introduction

semiconductor nanocrystals is treated as a building block in nanotechnology area due to size-selective and shape selective in synthetic step and also optoelectronic properties arising from quantum confinement. In particular, colloidal CdSe NCs outstand as a candidate in photosensitization applications and light emitting devices as CdSe NC is air-stable and lots of well-practiced synthesis schemes to give unit photoluminescence quantum yield.[1] Chemical modification of CdSe NC surfaces plays important role to its electrical and optical properties, and greatly impacts photoluminescence, band offsets, charge transfer and assembly in solid state. Moreover, we have perfluoro ligands (pFA) and short trifluoromethanethiolate (-SCF_3) could tune band offset of PbS QDs[2] and assist PbS QDs self-assembly to form conducting superlattice film.[3] Here, fluoro-coanting ligands are applied to functionalize CdSe NCs via solution ligand exchange and thin film ligand exchange. The optical properties and solubility of partial ligand-exchanged CdSe NC in solution and completely ligand-exchanged CdSe NC in thin film have been investigated.

6.2 Data and Discussion

6.2.1 Ligand exchange of CdSe NCs with in acetonitrile/ toluene

Initially, both octadecylphosphonic acid (ODPA) capped wurtzite CdSe NCs and zinc blende oleic acid capped CdSe NCs were investigated. However, due to the relatively small synthetic scale of ODPA CdSe NCs compared to the oleic acid CdSe NCs, most experiments were performed with the latter. We saw no significant difference in the surface chemistry during ligand exchange between both kinds of CdSe NCs, even though ODPA binds more strongly to

CdSe than oleic acid. Here, in this work, four batches of zinc-blende oleic acid capped CdSe nanocrystals (NCs) were investigated: 1). CdSe-small: absorption λ_{abs} = 495 nm; diameter= 2.3 nm, abbreviated as CdSe-495; 2). CdSe-medium: absorption λ_{abs} = 548 nm; half-width half maximum (HWHM) of first exciton maxima= 16 nm; diameter= 3.2 nm; PLQY= 3.4%, abbreviated as CdSe-548; 3). CdSe-medium/ large: absorption λ_{abs} = 587 nm, abbreviated as CdSe-587; 4). CdSe-large: absorption λ_{abs} = 596 nm; HWHM of first exciton maxima= 19 nm; diameter= 4.4 nm, abbreviated as CdSe-596

Table 6.1 CdSe-medium ligand exchange with $[NMe_4][SCF_3]$

NC = CdSe-548		L = $[NMe_4][SCF_3]$		[L]/[NC]	Toluene/ μl	λ_{abs} (nm)			
[NC]/mM	Vol/μl	[L]/(mg/ml)	vol/μl			0	8	18	Time (hrs)
0.087 toluene	45	1.58 acetonitrile	100	100	200	548	557	564	Abs. (nm)
			200	200	100	561	570	583	PL. (nm)

Table 6.2 CdSe-large ligand exchange with $[NMe_4][SCF_3]$ conditions

NC = CdSe-596		L = $[NMe_4][SCF_3]$		[L]/[NC]	Toluene /μl	λabs (nm)			
[NC]/mM	Vol/μl	[L]/(mg/ml)	vol/μl			0	8	18	Time (hrs)
0.506 in toluene	7.7	1.58 in acetonitrile	100	100	237.2	596	605	614	Abs. (nm)
			200	200	137.2	615	617	622	PL. (nm)

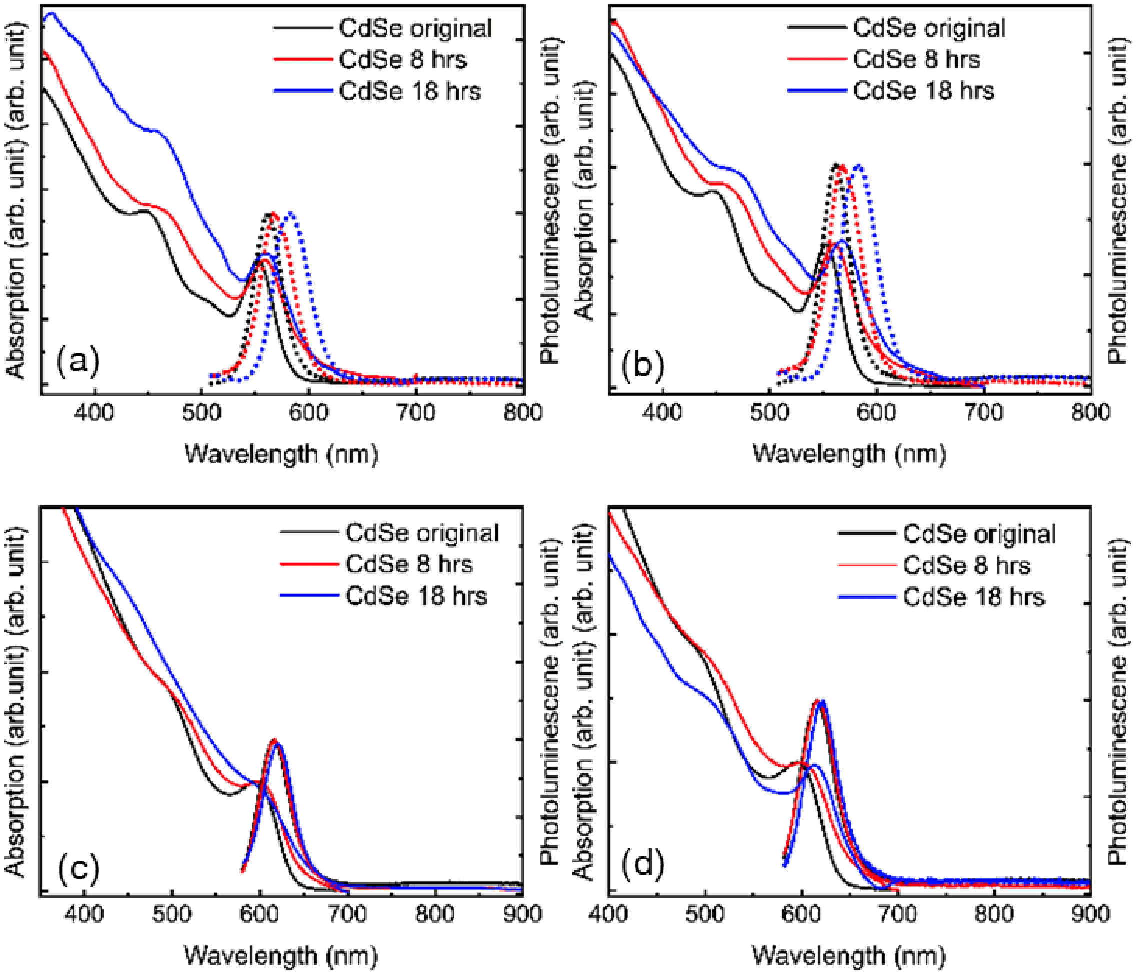

Fig. 6.1 Absorption and photoluminescence of partially ligand- exchanged CdSe NCs with –SCF_3 in mixture of toluene and acetonitrile for different time control. From top left to bottom right are (a) CdSe NCs with the first exciton peak at 548 nm ligand exchange with the concentration of ligand to nanocrystals in solution, [L]/[NC]=100 and (b) [L]/[NC]=200; (c) CdSe NCs with the first exciton peak at 596 nm ligand exchange with the concentration of ligand to nanocrystals in solution, [L]/[NC]=100; (d) [L]/[NC]=200. CdSe original is the CdSe NC being capped with OA before solution ligand exchange. 8 hrs and 18 hrs are the ligand exchange time.

After replacing the oleic acid ligands with SCF_3, all the CdSe NCs had their absorption and photoluminescence (PL) maxima red shift. For example, the smallest CdSe NC registered a bathochromic shift of 15 nm. The same trend is observed for the medium and large CdSe NCs, accompanied by broadening of their first exciton absorption maxima, as summarized in the tables above. After 18 hours ligand exchange, the CdSe NCs were no longer colloidally stable in toluene. However, no solvent was able to redisperse the CdSe@SCF_3 NCs, despite trying out alcohols (methanol, ethanol, isopropanol), dimethylformamide, dimethylsulfoxide, acetonitrile, tetrahydrofuran, etc. CdSe@SCF_3 NCs could not be dissolved in fully fluorinated solvents like perfluorodecalin (PFD) or perfluorotripropylamine (PFTPA) either.

6.2.2 Ligand exchange in solution and solid to form CdSe@SCF_3 thin films

Experiments details of fabrication of CdSe-medium/ CdSe-548@SCF_3 film: 1) Employing a ligand exchange time of 1 hour using conditions in 100× [L]/[NC] in Table 1, ethanol was used as a bad solvent to isolate the partially functionalized CdSe@OA+SCF_3 NCs. This decreased the PLQY of the CdSe NCs from 3.4% to 1.5%. Acetone could not be used as the resultant pellet could not be redispersed in toluene. 2) CdSe@OA+SCF_3 NCs in toluene was filtered with a 220 nm PTFE syringe filter. This solution is not stable. The NCs start crashing out the second day and completely crash out after 4 days. 3) Spin-coated [200μM] CdSe-medium@SCF_3 on substrate. 4) Soaked in 5 mg/ml [NMe_4][SCF_3] in acetonitrile for 2 hours. 5) Spin-coated away remaining solution. 6) Washed substrate with ethanol twice and THF once by spinning away solvent each time.

Experiments details of fabrication of CdSe-large/ CdSe-596@SCF_3 film: CdSe-large@OA was directly spin-coated on the substrate and dipped into 5 mg/ml [NMe_4][SCF_3] in acetonitrile for 2 hrs. Employing a ligand exchange time of 40 minutes using conditions in 100× [L]/[NC] in Table 6.2, resulted in NCs that could not be redispersed in toluene with most particles stuck on the 220 nm PTFE syringe filter. This method was abandoned.

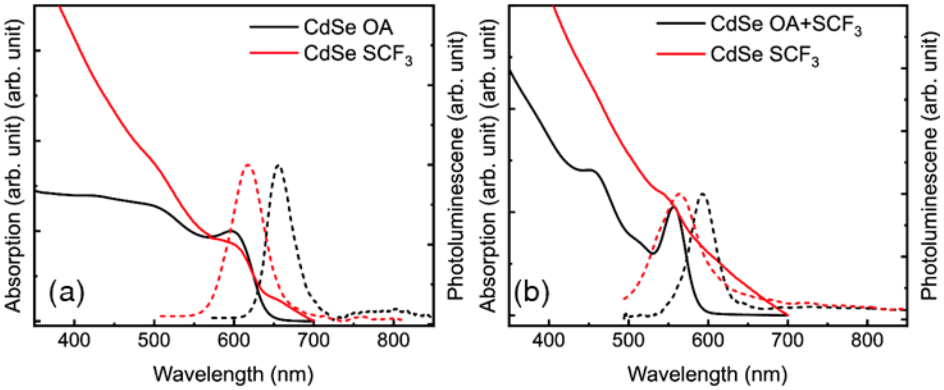

Fig. 6.2 Absorption and photoluminescence of CdSe NC: SCF_3 thin film after solution and solid ligand exchange.

Table 6.3 CdSe-548@SCF_3 was fabricated through a thin-film based ligand exchange (see above)

CdSe-548 λ_{abs}	Abs. (nm)	PL. (nm)
OA+SCF_3 soln.	556	569
OA+SCF_3 film (black)	557	592
SCF_3 film (red)	not defined	565

Table 6.4 CdSe-596@SCF_3 was fabricated by dip-coating (see above)

CdSe-596 λ_{abs}	Abs. (nm)	PL. (nm)
OA film (black)	597	653
SCF_3 film (red)	604	616

It is very interesting to observe that like for the PbS@SCF_3 thin films, a red shift in absorption and blue shift in PL is observed after ligand exchange of CdSe NCs. Fourier-transform infrared spectroscopy (FTIR) show complete ligand exchange as all oleic acid has been removed. It appears that the thin-film ligand exchange procedure we used for PbS@SCF_3 [2]is not directly transferrable. For example, normally [60μM] PbS@OA:SCF_3=2:1 when spin-coated would give a 30 nm thin film, but here, even though the same volume of [100μM] CdSe was used, the thin film thickness of 10 nm given by AFM was much lower. This is due to the difference of surface chemistry of PbS QDs and CdSe QDs even though with the same surface capping ligand, OA. Atomic Force Microscopy (AFM) images of CdSe-548@SCF_3 and Grazing

Incidence Small Angle X-ray Scattering (GISAXS) of CdSe-548@SCF_3 and CdSe-596@SCF_3 thin film are obtained in

Fig. 6.3 and Fig. 6.4. AFM images show a low roughness compared to the PbS@SCF_3 thin films. Only reflections off the beamstop were observed in GISAXS images. This leads us to conclude that these thin films have no long-range order, unlike the PbS@SCF_3 thin films fabricated under the same conditions. Thin-film Transistor current-voltage measurements on the following gave only 10^{-10} A of current: All three CdSe NC films: Dip-coated CdSe-596@SCF_3, dip-coated CdSe-548@SCF_3 and thin-film ligand exchanged CdSe-548@SCF_3. Moreover, annealing thin films at 60°C did not improve the mobility.

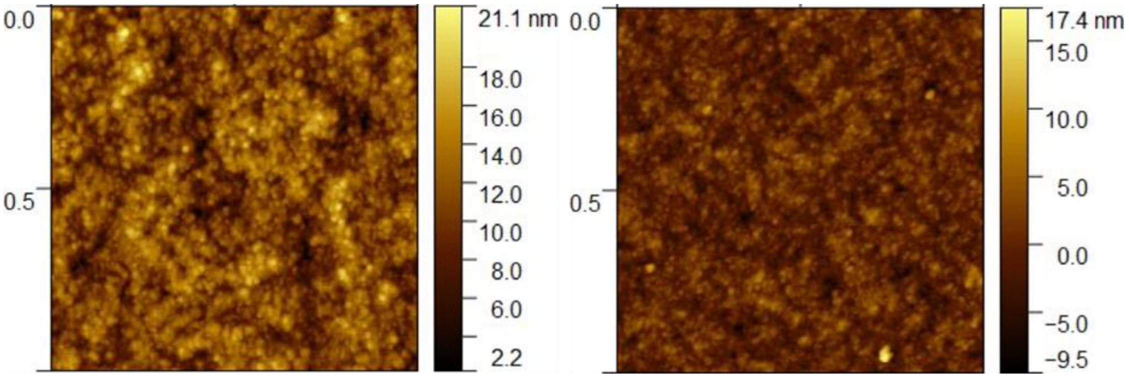

(a) RMS=2.2 nm (b) RMS=2.7 nm

Fig. 6.3 1×1 μm of Atomic Force Microscopy (AFM) images of the dipcoated CdSe-596@SCF_3 thin films on thermal oxide silicon wafer. AFM images show a low roughness compared to the PbS@SCF_3 thin films.

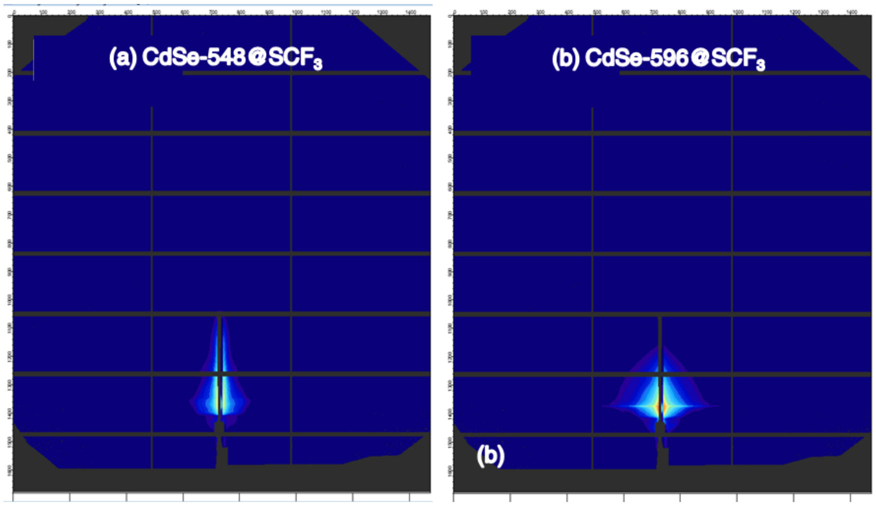

Fig. 6.4 Grazing Incidence Small Angle X-ray Scattering (GISAXS) images of CdSe-548@SCF$_3$ (a) and CdSe-596@SCF$_3$ (b) thin films were performed at beamline 12-ID-B at Argonne National Lab. Samples were kept air-free until 5 minutes before the measurement. Details of measurement is seen in chapter 7.2 instruments section.

6.2.3 Ligand exchange of CdSe NCs with pFA in solutions

Table 6.5 Ligand exchange of CdSe NCs with pFA in solutions in glovebox (<0.2ppm oxygen; <0.5ppm water)

CdSe 526		pFA in THF				THF /ml	[NC] in LX /mM	Observations
[NC]/mM	μL	pFA	[L]/[NC]	[pFA] (mg/ml)	Vol/ml			
0.85	15	C9	3000	90.0	0.20	0.00	6.3	[1]Partial sol: PhCF$_3$
	10		500	26.33	0.07	0.15	37	[2]Pellet insoluble
			1500	26.33	0.23	0.00	37	
		C16	500	15.75	0.22	0.44	13	
			1500	15.75	0.66	0.00	13	
			1345	3.33	2.0	0.00	4.2	[3]Partial sol: PhCF$_3$

A lot of trials of ligand exchange of CdSe NC with pFA ligands showed after 12 hours ligand exchange, 0.40 ml of bad solvent acetone was used to isolate a pellet. However, the CdSe NCs couldn't be redispersed in toluene, acetone, PFD, PFO and PFMeCyH. The pellet is partially soluble in trifluorotoluene, PhCF$_3$. Photoluminescence of CdSe NC after ligand exchange blue shifts comparing with CdSe@OA. A lot of solvents have been tried to dissolve CdSe NCs after 12 hours ligand exchange. However, the CdSe NCs couldn't be redispersed in toluene, THF, trifluorotoluene, dimethyl sulfoxide and dimethylformamide. FTIR confirmed that partial ligand exchange occurred as C-H bonds could still be observed. This ligand exchange is irreversible.

As the PFAs like to dissolve in THF compared to toluene, we further increased the amount of THF in ligand exchange to further increase concentration of CdSe NCs in solution to 37 mM to increase ligand exchange rate. After 15 hours ligand exchange in solution, 0.50 ml of bad solvent acetone was used to isolate a pellet. However, the CdSe NCs couldn't be redispersed in toluene, THF, dimethyl sulfoxide and dimethylformamide. The pellet is partially soluble in trifluorotoluene, $PhCF_3$. PL indicates trap state emission has been markedly increased relative to band edge emission, indicating failure of the ligand exchange.

Among all the ligand exchange of CdSe NCs with pFA ligands, one successful CdSe@pFA ligand exchanges in details are 1) CdSe-512 was crashed out with twice the volume of methanol and redissolved in $PhCF_3$. 2) 0.0645 μmols of CdSe was combined with 5.676 μmols pFA-C9 and $PhCF_3$ to a total volume of 1mL. 3) The solution was stirred for 4 hours. 4) 2 mL of acetone was added and the mixture centrifuged for 10 minutes at 7830 rpm. 5) The pellet was redissolved in 1 mL $PhCF_3$ or 7:3 PFD:PFTPA. The solubility of CdSe@pFA-C9 was low in both $PhCF_3$ and 7:3 PFD:PFTPA as fine particles were seen throughout solution. However, solubility was better in $PhCF_3$ than in 7:3 PFD:PFTPA.

As $-SCF_3$ as capping ligands assists periodic PbS nanocrystals alignment, sodium trifluoroacetate is applied to ligand exchange with CdSe@OA ligands. Interestingly, blue shift of the first absorption exciton peak, from 526 nm (oleic acid) to 521 nm (trifluoroacetate), is observed for CdSe-526 NC. Moreover, pure trifluoroacetic acid dissolves CdSe NCs after ligand exchange. This work is still under investigation.

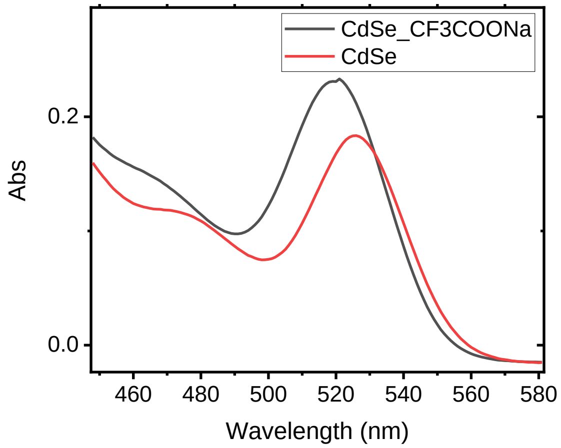

Fig. 6.5 Absorption of CdSe NCs before (red curve) and after ligand exchange (dark curve) with CF_3COONa. Ligand exchange conditions: [CdSe-526] in ligand exchange solution= 21.25 mM, [CF3COONa]/[NC]= 5500.

6.2.4 Lists of Chemical abbreviations

CdSe-512: Zinc-blende oleic acid CdSe NCs with absorption maxima = 512 nm in hexanes; 2.5 nm diameter. CdSe-526: Zinc-blende oleic acid CdSe NCs with absorption maxima = 526 nm in toluene, 2.6 nm diameter

Perfluorinated chemicals:

$PhCF_3$:	Trifluorotoluene
PFD:	Perfluorodecalin
PFO:	Perfluorooctane
PFMeCyH:	Perfluoro(methyl)cyclohexane
PFTPA:	Perfluorotripropylamine
pFA-C16:	Perfluorohexanoic acid (linear); MW= 814.13 g/mol; 23 mg/ ml solubility in THF

pFA-C9: Perfluorononanoic acid (linear); MW= 464.08 g/mol; 90 mg/ ml solubility in THF

6.3 Conclusions

Zinc-blende oleic acid (OA) capped CdSe nanocrystals (NCs) were functionalized with perfluorocarboxylic acids (pFAs) and trifluoromethylthiolate (-SCF_3). CdSe@SCF_3 nanocrystal thin films did not show long range order/ superlattice structure, nor any current in transistor current-voltage measurements (Section I). Under certain ligand exchange conditions, CdSe@pFA could be redispersed in fluorinated solvents.

6.4 Notes and References

1. Gao Y*, et al.* Photogenerated Excitons in Plain Core CdSe Nanocrystals with Unity Radiative Decay in Single Channel: The Effects of Surface and Ligands. *J Am Chem Soc* . 2015, 137(12): 4230-4235.

2. Chen S*, et al.* Near-infrared deep brain stimulation via upconversion nanoparticle–mediated optogenetics. 2018, 359(6376): 679-684.

3. Pan Xia DWD, Bijal B. Patel, Maotong Qin, Zhiming Liang, Kenneth R. Graham, Ying Diao, and Ming Lee Tang. Spin-coated fluorinated PbS QD superlattice thin film with high hole mobility. In: Riverside UoC, editor.; 2019.

7 Chapter 7 Supporting Information

7.1 Chemicals

7.1.1 Chemicals of CdSe: anthracene derivative

Chemical reagents were purchased from Sigma-Aldrich, TCI America, Alfa Aesar and were used without further purification. As for nanocrystal synthesis, cadmium oxide was purchased from Alfa Aesar, and trioctylphosphine oxide (90%) (TOPO), trioctylphosphine (97%) (TOP), octadecylphosphonic acid (97%) (ODPA) were purchased from Strem Chemicals. 9, 10-diphenylanthracene (>93%) (DPA) 9-anthracenecarboxylic acid (97%) (9-ACA), 2-anthracenecarboxylic acid (98%) (2-ACA) and 1-anthracenecarboxylic acid (99%) (1-ACA) were obtained from TCI America. 9-nitroanthrancene (97%); 2-aminoanthracene (98%); 1-aminoanthracene (90%); N-methyl-pyrrolidone (99%) (NMP); rhodamine 6G (99%), hexane (99%), methoxybenzene, poly(4-bromostyrene) (Mw ~65,000) (4BrPS) and carbon disulfide (99%) were purchased from Sigma-Aldrich. Triethylamine (99.7%) (NEt3) and tetra-n-butylammonium hexafluorophosphate (98%) were from Acros. Glacial acetic acid (99.9985%) was from Alfa Aesar. Dry and degassed acetone, toluene, tetrahydrofuran (THF) and dichloromethane were obtained from JC Meyer's solvent purification system.

7.1.2 Chemicals of silicon nanocrystals with 9 ethyl anthracene

9-vinyl anthracene (9VA, 97%) and 9,10-diphenylanthracene (DPA, 98%) were purchased from TCI America. 1-octadecene (ODE, tech., 90%) and 1,2-dichlorobenzene (o-DCB, 99.5%, extra dry) are from Acros Organics and were heated to 120 °C under vacuum to remove low boiling point impurities. Indocyanine green (95%) is from Chem-Impex Int'l. Inc. 9-methlyanthracene (9MA, 98%) and platinum octaethylporphyrin (PtOEP, 98%) used for triplet sensitization experiments were obtained from Sigma Aldrich. Deuterated chloroform ($CDCl_3$, 99.8%) is from Cambridge Isotope Laboratories, Inc. Poloxamer 188 (M. W. = 8400) is from Spectrum Chemical. Dry acetone, dichloromethane (DCM) and toluene were purchased from Alfa Aesar and degassed with a JC Meyer solvent purification system. Dried methanol and dimethyl sulfoxide (DMSO) are from Sigma Aldrich and were brought into a glove box after degassing. Mesitylene (98%) is from Sigma Aldrich and was dried with molecular sieves. All other chemicals were used as received.

7.1.3 Chemicals for PbS or CdSe @SCF_3, SCH_3 and pFA complexes

Chemical reagents were purchased from Sigma-Aldrich, TCI America, Alfa Aesar, Acros Organics and Matrix Scientific, and were used without further purification unless otherwise mentioned. Lead oxide was purchased from Alfa Aesar. Oleylamine, oleic acid (OA), octadecene (ODE), bis(trimethylsilyl) sulfide, $(TMS)_2S$, tetramethylammonium fluoride, $[NMe_4]F$, trifluoromethyl trimethylsilane, $TMSCF_3$, sodium methoxide (95%), carbon disulfide (CS_2), CdO (≥99.99%) and selenium powder (99.99%) are from Sigma-Aldrich. Perfluorohexadecanoic acid (95%), pFA is from Matrix Scientific. Dry ethanol is from Acros Organics. Toluene-d8, acetonitrile-d6, acetone-d6 and dimethyl sulfoxide-d6 (DMSO-d6) are from Cambridge Isotope Laboratories and dried with 3 Å molecular sieves. Trifluorotoluene (Sigma Aldrich, denoted as PhCF3) was dried with magnesium sulfate before use. Sulfur (Sigma Aldrich, 98%) is purified by recrystallization in benzene. Benzoquinone (Sigma Aldrich, 98%, BQ) is purified by recrystallization in acetic acid once. Dry and degassed acetone, acetonitrile, dichloromethane (DCM), toluene and tetrahydrofuran (THF) were obtained from JC Meyer's solvent purification system.

7.1.4 Chemicals for fabrication of PbS@SCF_3 thin film transistor

Lead (II) oxide (99.9995%) and silver nitrate ($AgNO_3$, 99.9995%) are from Alfa Aesar.

dodecylamine (98%), 1,2-ethanedithiol (EDT) (>98%), ethanol (anhydrous, ≤0.005% water), 3-mercaptopropyl trimethoxysilane (3-MPTMS, 95%), 1H,1H,2H,2H-Perfluorodecyltriethoxysilane (PFDTEOS, 97%), phenyl isothiocyanate (98%), oleic acid (OA, 90%), 1-octadecene (ODE, 90%) and tetrabutylammonium hexafluorophosphate (TBA-PF6, ≥99.0%), were purchased from Sigma-Aldrich and used as received. Hexanes is purchased from Fisher Scientific and dried with MgSO4 before use. Toluene and acetonitrile are purified and dried with JC Meyer Solvent purification system. [NMe4][SCF3] is synthesized as our previous report.1 Syntheses and cleaning of quantum dots (QDs) and fabrication and measurement of TFT were carried out in nitrogen filled gloveboxes.

7.2 Instruments

7.2.1 Instruments of CdSe: anthracene derivatives

Proton NMR (^{1}H) spectra was recorded on Varian Inova-300 MHz or 400 MHz spectrometers; carbon NMR (^{13}C) spectra were recorded on a Varian Inova-600 MHz spectrometer at room temperature. The ^{1}H and ^{13}C chemical shifts (δ) are reported in parts per million and the residual solvent peak was used as an internal standard. Absorption spectra were recorded on a Jasco-V670 UV-Vis absorption spectrophotometer. Upconversion samples were prepared in the glove box with air-free cuvettes and measurements were performed as described earlier [1]. Infrared absorption spectra were obtained from ALPHA FTIR Spectrometer (Bruker Corporation). Samples for transient absorption measurements were prepared in toluene in a 2 mm air-tight quartz cuvettes, which the optical density of CdSe NCs around 0.4-0.5 at 465 nm. Ground state absorption was taken before and after the transient absorption experiment to show there is no decomposition. Details of the setup are described in previous work[1]. Fluorescence spectra and phosphorescence spectra was measured with steady-state fluorimeter (Fluoromax-3, Horiba scientific).

7.2.2 Instruments for silicon nanocrystals with 9 ethyl anthracene

Absorption spectra were recorded on a Jasco-V670 UV-Vis absorption spectrophotometer. Ensemble photoluminescence (e.g. fluorescence, photon upconversion, power dependence, etc.) spectra were recorded on a Maya 2000-Pro Spectrometer (Ocean Optics Inc.) with continuous wave (CW) solid-state lasers (488 nm: OBIS LX 75 mW, Coherent Inc.; 532 nm: Sapphire SF 532, Coherent Inc.; 640 nm: OBIS LX 40mW, Coherent Inc.). Neutral density filters (Thorlabs) were used to tune the power of excitation light without changing the beam size. Semrock notch filters were used to remove the excitation light. Laser power was measured using a benchtop optical power and energy meter (2936R, Newport Corp.) and Si wand detector head (818-ST2/DB, Newport Corp.).

Nuclear magnetic resonance (NMR) spectra were recorded on a Bruker AVANCE NEO 400 MHz NMR spectrometer at room temperature. ^{1}H chemical shifts (δ) are reported in parts per million with a residual solvent ($CDCl_3$) peak as an internal standard. All infrared spectra (IR) were obtained with an attenuated total reflectance (ATR) spectrometer (Thermo Fisher Scientific Nicolet iS10 with Smart iTX XR Diamond Crystal Accessory) except for fresh hydrogen-terminated Si nanocrystals, Si:H. ATR on Si:H was performed using a Newport-Oriel modular spectrometer equipped with a deuterated triglycine sulfate (DTGS) detector. Spectra are recorded in the 500 –5000 cm^{-1} range. IR samples are prepared by dispersing Si NC powder in chloroform with sonication followed by drop-casting onto a zinc selenide ATR crystal.

XRD analysis was performed by drop-casting the nanoparticles onto a zero background substrate. The measurements have been performed on a Panalytical Empyrean with a Cu Kα source. Further structural characterization was performed via TEM by drop-casting the nanoparticles onto a lacey carbon grid. A FEI Titan Themis with 300 kV accelerating voltage was used for TEM characterization. A LaB6 standard has been used to correct for instrumental broadening.

Excitation pulses for transient absorption (TA) measurements were provided by a frequency-doubled Q-switched Nd:YAG laser operating at 532 nm (Alphalas Pulselas-A, < 1 ns, 8.7 □J) while supercontinuum probe pulses were generated by focusing the output of a Ti:sapphire amplifier operating at 804 nm (Coherent Duo Legend Elite, 3 kHz, 4.5 mJ) into a flowing water cell (Starna). Electronic synchronization and scanning of the time delay between the pump and probe lasers were achieved using a digital delay generator (Stanford Research Systems DG535). Pump induced changes in the probe pulse spectrum were readout using a 500 mm Czerny-Turner spectrometer (Acton Instruments Spectra Pro 2556) operating in series with a silicon CCD camera (Princeton Instruments PyLoN 100-BR). Si NC samples were housed in a nitrogen glove box prior to TA measurements, placed into sealed cuvettes for TA experiments, and continuously stirred during data collection. Oxidation of NC samples was periodically checked by measuring changes in sample absorption spectra, which show a loss of 9EA absorption features upon sample oxidation.

The hydrodynamic diameters of micelle samples were measured by dynamic light scattering (DLS) using a Malvern Zetasizer NanoZS90 at room temperature. The bulk emulsion solution was diluted in MilliQ H_2O (20 µL emulsions in 1 mL MilliQ H_2O) in a polystyrene cuvette (1 cm pathlength). Each DLS measurement was obtained at scattering angle of 90°. The size of micelles is the z-average diameter, which is the intensity-based harmonic mean of the light-scattering particles. SOP parameters: 10 runs, 10 seconds/run, four measurements, no delay between measurements, 22 °C with 10 seconds equilibration time.

7.2.3 Instruments of PbS or CdSe @SCF_3, SCH_3 and pFA complexes

Proton NMR (^1H) spectra was recorded on Bruker Advance NEO 400 MHz and Bruker Advance 600 MHz spectrometers; Fluorine NMR (^{19}F) spectra were recorded on a Bruker Advance 600 MHz spectrometer. The ^1H and ^{19}F chemical shifts (δ) are reported in parts per million and the residual solvent peak or ferrocene was used as an internal standard at room temperature. Absorption spectra were recorded on a Jasco-V670 UV-Vis absorption spectrophotometer. Photoluminescence of quantum dots and dyes are obtained with a Horiba PTI Quanta Master 400 using a PMT detector in the UV-vis range and an InGaAs detector for the NIR range. A correction curve provided by the manufacturer was applied to correct for the differing sensitivities of these two detectors. Samples were prepared in the glove box with air-free cuvettes. Transmission electron microscopy (TEM) images are obtained using a FEI Tecnai12 TEM (Thermo Fisher Scientific Inc.) using LaB_6 at 120 kV. Infrared absorption (IR) spectra were obtained on a Nicolet 6700 FTIR Spectrometer (Thermo Electron Corporation). Cyclic voltammetry (CV) electrochemical measurements were conducted on a WaveDriver 10 Potentiostat (Pine Instrument Company, WD10-BASIC) with a three-electrode system under argon (Ar). Ultraviolet photoelectron spectroscopy (UPS) measurements were performed using the Excitech H Lyman-α photon source (E-LUX™121, 10.2 eV) coupled with a 90° ellipsoidal mirror (E-LUX™ EEM Optical Module), as detailed in a previous publication.[2] All UPS measurements were performed in a PHI 5600 UHV system containing an 11-inch diameter hemispherical electron energy analyzer with a multichannel plate detector. Samples were negatively biased (−5 V) during UPS measurements and the pass energy was 5 eV.

Time correlated single photon counting (TCSPC): Photoluminescence lifetimes were recorded on a PicoHarp Time-Correlated Single Photon Counting setup (PicoHarp 300). Samples were excited by ultrafast pulses at a repetition rate of 35.7 kHz with a pulse picker and centered at 480 nm from a light source consisting of a femtosecond laser system (PHAROS, Light Conversion, tunable repetition rate 50 Hz - 250 kHz) pumping an optical parametric amplifier and second harmonic generator (ORPHEUS/LYRA, Light Conversion). The excitation intensity was controlled with neutral density filters and the excitation power was kept at less than 100 nJ for all measurements. For detection, InGaAs/InP Single-Photon Avalanche Diode (quasi free-running mode within the gated module, Micro Photon Devices S.r.l.) and the PicoHarp 300 (PicoQuant, 65536 channels) with 256 ps or 512 ps resolution was used and a count rate of <1% of the excitation rate was maintained. Fits were made to two exponential decays with a y-offset and the amplitude average lifetime was extracted from the fits.[3]

7.2.4 Instruments of fabrication of PbS@SCF$_3$ thin film transistor

Structural and Optical Characterization: The absorption spectra of solution were obtained with a Jasco/V670 UV/Vis absorption spectrophotometer. The absorption spectra of thin films were obtained with a Varian Cary 500 UV/Vis/NIR spectrophotometer. Photoluminescence of the QDs both in solution and thin film are obtained with a Bayspac SuperGamut^{TM} NIR Spectrometer using 488 nm laser (OBIS LS, Coherent) excitation. Thin film samples for absorption and emission are fabricated by spincoating the PbS QD solution on glass after 3-MPTMS treatment and sealed with epoxy to keep the sample air-free. The AFM images were obtained by a Dimension Icon XR (Bruker) in tapping mode. IR spectra were obtained on a Nicolet iS10 IR Spectrometer (Thermo Fisher Scientific) in transmission mode.

Long Range Ordering Characterization: GISAXS experiments were performed at beamline 12-

ID-B of the Advanced Photon Source at Argonne National Laboratory. The PbS QD solution was spincoated onto an atomically smooth silicon wafer with a native oxide treated with 3-MPTMS. Samples were sealed under an inert atmosphere during transit to the beamline and exposed to ambient air for several minutes prior to and during scanning. Spectra were collected on a Pilatus 2M, two-dimensional detector using an incident X-ray beam energy of 13.3 keV and a sample to detector distance of 3.6m, calibrated against a silver behenate standard. Spectra collected at incident angles ranging from 0.04° to 0.2° show qualitatively similar features. Quantitative peak fitting was performed on spectra obtained using an incident angle of 0.12°, below the estimated critical angle of PbS (0.24° at 13.3 keV). Analysis was done by simulating the diffraction pattern using the GIXSGUI package[4] for MATLAB by specifying the lattice parameters and orientation and performing iterative fitting to match the experimentally obtained scattering pattern.

Transmission electron microscopy (TEM): 40 nm thick SiO_2 films on silicon nitride TEM grids with 50 x 50μm/24 apertures are from Ted pella, Inc. (part no. 21530-10). The PbS QD solution prepared as above was spincoated on these TEM grids after 3-MPTMS treatment. TEM images were recorded on a FEI Titan Themis 300 with an X-FEG electron gun. The superlattice spacing were determined from multiple regions by analyzing the scattering peak positions extracted from the Fourier-transformed images.

Cyclic Voltammetry Measurement: Cyclic voltammetry (CV) electrochemical measurements were conducted on a WaveDriver 10 Potentiostat (WD10/BASIC, Pine Research Instrument). Measurements were performed under nitrogen in anhydrous acetonitrile with 0.1 M TBA-PF_6 as the supporting electrolyte. 0.5 mm platinum electrode (part no. RRPG257PT, Pine Research Instrument) served as the working electrode and counter electrode. An encased Silver (Ag) pseudo-reference electrode with ceramic frit on bottom filled with a 10 mM $AgNO_3$, 0.1 M TBA-PF_6, acetonitrile solution served as the reference electrode (part no. RREF0153, Pine Research Instrument). The concentration of $[NMe_4][SCF_3]$ in solution was approximately 3 mM. CV scans were performed at 100 mV/s, and half-peak potentials ($E_{p/2}$) were used to estimate the oxidation potential, $E^o_{1/2,}$ as the CV of $[NMe_4][SCF_3]$ is irreversible due to dimerization of the thiolate groups.[5] An internal standard, ferrocene is added to the electrochemical cell after CV was performed on $[NMe_4][SCF_3]$. The ferrocene/ferrocenium (Fc/Fc^+) redox couple with a value of 4.8 eV with respect to vacuum. The HOMO of $[NMe_4][SCF_3]$ is measured as $-(E_{1/2,\ [NMe4][SCF3]} - E_{1/2,\ ferrocene}) + 4.8$ eV.[6] The potential of this $Ag/AgNO_3$ standard electrode in 0.01 M acetonitrile vs. saturated calomel electrode (SCE) is +0.3 V.[7] Therefore the $E_{p/2}$ of $[NMe_4][SCF_3]$ is +0.69 V vs. SCE, which is lower than thiophenols and aryl disulfides reported by Nicewicz et al.[5]

Ultraviolet Photoelectron Spectroscopy: The substrates for the UPS measurement are on 1.5 cm × 1.5 cm native silicon wafer coated with a 60 nm Au layer formed by thermal evaporation. The PbS−SCF_3 QD thin film was fabricated as described above, resulting in a QD film thickness of ∼40–50 nm. The films were fabricated in a glovebox at UC Riverside, shipped in nitrogen filled sealed packages to the University of Kentucky, unpacked in a nitrogen-filled glovebox and inserted into the ultra-high vacuum system directly through the glovebox without ever being exposed to the atmosphere. An Excitech H Lyman-a photon source (E-LUX™121) coupled with a 90° ellipsoidal mirror (E-LUX™ EEM Optical Module) was used as the excitation source for UPS with an 8 Torr nitrogen purge of the beam path. The photoelectrons were detected with an 11-inch diameter hemispherical electron energy analyzer coupled with a multichannel plate detector using a 5 eV pass energy. A negative 5 V bias was applied to the samples during measurements. The SECO (ionization energy) of the samples was determined by the intersection of the background and a linear fit to the lower 50% of the SECO as we described in our previous publication.[8]

TFT Fabrication and Characterization: Current-voltage transistor measurements were performed in air-free conditions in bottom contact geometry with a common gate separated by a 200 nm dry thermal oxide patterned with 35 nm Au electrodes on a 5 nm Ti adhesion layer. The Keithley 2636B semiconductor parameter analyzer was used for all measurements with a Signatone probe station. The channel lengths, L are 10, 20, 30 and 100 µm. The ratio of channel width, W, to L, or W/L = 20 in all cases. The scan rate is 0.09-0.10 V/ms to minimize the influence of trap induced transient decays of the measured current. The annealed sample was heated on a KW-4A hotplate at 60°C for 3 hours in a nitrogen glovebox.

7.3 Nanocrystal synthesis

7.3.1 Synthesis of diameter=2.4 nm CdSe nanocrystals

CdSe nanocrystals (NCs) were synthesized and purified by the procedure reported by Carbone et al. [9]Trioctylphosphine oxide (TOPO) (3.0g), octadecylphosphonic acid (ODPA) (0.280g) and CdO (0.060g) were mixed in a 25mL three neck flask, heated to 150°C and exposed to vacuum for at least 1 hour. Then, under Ar (g), the solution was heated to 330°C to dissolve the CdO. At this point, 1.5 g of trioctylphosphine (TOP) was injected and the temperature was increased to 370°C. Then the Se:TOP solution (0.058g Se + 0.360g TOP) is injected. About 5-15 s after injection, the reaction flask was cooled down quickly with compressed air. Different cooling time after injection will result in different size of CdSe NC. After the synthesis, as-prepared CdSe NCs were transferred to the glove box and cleaned with methanol and toluene at least three times. The final pellet was dissolved in toluene and stored inside a nitrogen glove box for future use. The NC concentration and diameter was determined by measuring the absorbance at the first exciton absorption maxima and calculated according to Yu et. al. [10]The photoluminescence quantum yield of the 2.4 nm diameter particles was measured to be 13% using Rhodamine6G in anhydrous ethanol (quantum yield = 0.95[11]) as the standard. Other size of wurtzite CdSe nanocrystals with ODPA capped are also synthesized the similar ways except for injection temperature and nuclearation time.

7.3.2 Synthesis of d=3.2 nm PbS nanocrystals

PbO (0.45 g), oleic acid (OA, 10 mL), and 1-octadecene (ODE, 10 mL) were mixed in a 50 ml three neck flask and heated to 110 °C under vacuum for an hour. Pb oleate is formed, indicated by the discoloration of the reaction to a clear light-yellow solution. Then the reaction flask was backfilled with Ar (g), and heated to 150 °C. At 150 °C, the sulfide 95 precursor, containing 0.21 mL of bis(trimethylsilyl)sulfide in 10 mL of anhydrous ODE, was injected, and the temperature dropped to about 130 °C. The reaction flask could cool down to 100°C for 3 min by turning off the heater. Then the reaction flask was kept at 100 °C for 5 min. The PbS NCs were transferred to a glovebox and washed 3 times by adding 1:1 hexanes/ethanol mixture; followed by centrifuging at 7000 rpm for 5 min. The supernatant was discarded. The final pellet was dissolved in hexane and stored in the dark inside the glovebox for future use. The PbS NC size (3.1 nm diameter) was determined by measuring the energy of the first exciton peak. The concentration of the PbS NCs was determined from the absorption at 400 nm[3].

7.3.3 Synthesis of d=6.5 nm PbS nanocrystals

PbS QDs were synthesized and cleaned entirely in a glovebox, using a 1-dodecyl-3-phenylthiourea precursor in combination with lead oleate at 120ºC, according to procedures first outlined by Hendricks and Owen[12]. N-dodecyl-N’-phenylthiourea was prepared by adding n-dodecylamine (5.78 g, 31.2 mmol) in toluene (10 mL) and phenyl isothiocyanate (4.22 g, 31.2 mmol) in toluene (10 mL), producing a white powder. After vacuum filtration, the white solid is further dried under high vacuum for 4 hours. In a typical synthesis, lead oleate (1.41 g, 2.29 mmol) and ODE (14.75 ml) were mixed in 24 mL vials and heated to 120 °C in a nitrogen glovebox. 1-dodecyl-3-phenylthiourea (0.49 g, 1.53 mmol) and diglyme (0.5 ml) was mixed in 4 ml glass vials and is heated to 120 °C. Once the temperature is stable (15 minutes), the solution of thiourea was quickly added into the clear colorless solution. The reaction was quenched with a large amount of cold hexane after 10 minutes. The PbS QDs were thoroughly cleaned in glove box with three precipitation/redispersion steps using anhydrous ethanol as a bad solvent and anhydrous hexane as good solvent. Finally, QDs were dispersed in anhydrous toluene with a concentration of 72 µM, and optical absorption was performed to determine the QD size (5.1 nm according to the sizing curve of Moreels et al.[13]).

7.3.4 Synthesis of zinc blende CdSe with oleic acid as capping agent

CdSe QDs with first exciton peak at 495 nm: CdO (4 mmol, 0.512 g), 10 mmol OA (3.14 g) and 25 g ODE were heated at 260 ^{o}C for 20 min, then the solution was cooled to 240 ^{o}C (CdSe-496) for the injection of Se precursor. The Se precursor was made by dispersing 4 mmol Se powder in 10 mL ODE via sonication for 5 min, and 5 mL dispersion was used for each synthesis. Before the injection of Se precursor, the heating mantle was removed, and the solution was allowed to cool down to room temperature naturally.

CdSe QDs with first exciton peak at 587nm: CdO (4 mmol, 0.512 g), 20 mmol OA (6.28 g) and 25 g ODE were heated at 260 ^{o}C for 20 min. The Se precursor was injected at 260 ^{o}C and the solution was maintained at 240 ^{o}C. Wait 10 mins to 30 mins to get desirable size by taking some portion out and doing absorption spectra to decide whether stopping reaction. Here, the Se OD precursor is the same as previous recipe. While Zhang et al injects TOPSe (1M) being diluted in ODE to get large size CdSe NCs 1 min after injection of Se in ODE.[14] However, it's difficult for us to obtain large size CdSe with HWHM to be less than 15 nm. In our synthesis of large size CdSe NCs, injection of TOPSe destroyed the narrow size dependence of CdSe NCs.

7.4 Synthesis of surface ligands

7.4.1 Synthesis of anthracene dithiocarbamate acid (ADTC) derivatives

All the ADTC ligands were obtained from the corresponding aminoanthracene precursors by reaction with carbon disulfide (CS_2) and triethylamine at 45°C in acetone or THF under nitrogen, as shown in Scheme S1[15]. 1-ADTC (1) and 2-ADTC (2), precipitated from acetone or THF after 24 hours, resulting in ~90% yield. For 9-ADTC (4), we firstly synthesized its precursor, 9-aminoanthracene (3) from 9-nitroanthracene[16].

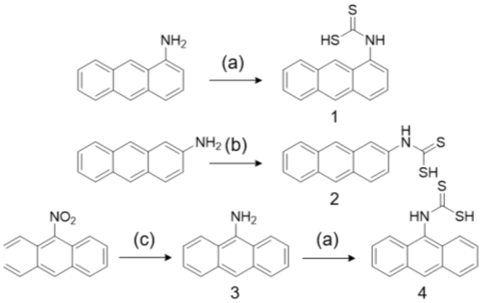

Scheme 7.1 Organic synthesis of anthracene dithiocarbamate acid (ADTC). Reagents and conditions: (a) CS_2, NEt_3, acetone, 45°C, 24h. (b) CS_2, NEt_3, THF, 45°C, 24h. (c) 1. AcOH, 80°C; 2. $SnCl_2$, HCl, 80°C.

Compound 1: 1-aminoanthracene was purified by silica gel based chromatography (1: 3 = hexane: DCM as eluent) before synthesis because the commercially available precursor contained 10% impurities. It is a yellow powder and forms brown solution in anhydrous acetone. A solution of purified 1-aminoanthracene (0.8 mmol, 154.5 mg) and NEt_3 (2.4 mmol, 0.69 ml) in 1 mL of acetone was stirred at ambient temperature for 10 min, after which 1.5 mL of CS_2 was added dropwise. The resulting solution was further stirred at 45°C for 24 h. The yellow solid was collected by filtration, washed with ether, acetone and dried under vacuum at RT for 5 h (90%, 200mg). The product was further purified by washing with hot THF twice. ^{1}H NMR (300 MHz, DMSO-d6): δ_H = 10.00 (s, 1H), 8.65 (s, 1H), 8.60 (s, 1H), 8.12(d, J=9 Hz, 1H), 8.06-7.99 (m, 2H), 7.64 (d, J= 6.0 Hz, 1H), 7.57-7.52 (m, 3H) ppm. ^{13}C NMR (600 MHz, DMSO-d6): δ_C =182.89, 131.58, 131.33, 130.82, 129.10, 128.12, 128.19, 127.82, 125.87, 125.73, 125.25, 125.29, 124.47, 124.43, 118.97 ppm. IR (ATR): 2937, 1628, 1535, 1487, 1384, 1316, 1269, 1243, 1171, 970, 897, 795, 743 cm^{-1}.

Compound 2 was obtained in the same way as compound 1 as a yellow solid (yield 90%, 200mg). ^{1}H NMR (400 MHz, DMSO-d6): δ_H = 10.30 (s, 1H), 8.55 (s, 1H), 8.51 (s, 1H), 8.22 (s, 1H), 8.09- 8.06 (m, 3H), 7.72 (dd, J=9 Hz, 3Hz, 1H), 7.51-7.49 (m, 2H) ppm. ^{13}C NMR (600 MHz, DMSO-d6): δ_C = 182.72, 135.21, 132.21, 129.95, 128.73, 128.33, 121.12, 121.06, 127.29, 126.60, 125.94, 125.86, 125.29, 125.21, 121.73 ppm. IR (ATR): 2965, 1633, 1588, 1534, 1486, 1314, 1291, 1176, 1013, 954, 904, 824, 875, 744, 700, 685, 659 cm^{-1}.

Compound 3 is a known compound[16]: 9-nitroanthracene (0.362 g, 1.625 mmol) was added to acetic acid (0.363 mL) and stirred at 80 °C for 1.5 h. This solution was allowed to cool down to room temperature and $SnCl_2$ (1.55 g, 8.16 mmol) in HCl (5.5 mL) was added slowly. The mixture was then heated for 30 min at 80 °C. After cooling down to room temperature, the reaction solution was filtered and washed by HCl three times to give yellow solid. The yellow solid was bascified with 150 mL 5% NaOH solution, stirred at room temperature for 15 min, filtered, and the filter cake was washed with DI water to pH=7, then dried to give a yellow solid which was recrystallized from benzene to obtain compound 3 (yield 72%, 500 mg). ^{1}H NMR (400 MHz, $CDCl_3$): δ_H =7.96(m, 4 H), 7.89 (s, 1 H), 7.43 (m, 4 H), 4.89 (broad, 2 H) ppm.

Compound 4 was synthesized from compound 3 in the same way as compound 1 and 2. A yellow solid was obtained (yield 91%, 400 mg). Then it was purified with silica gel chromatography (1:1 = hexane: DCM as eluent, yield 85%, 400 mg). ^{1}H NMR (400 MHz, $CDCl_3$): δ_H = 8.40 (s, 1H), 8.30 (dd, J= 8, 1 Hz, 2H), 8.03 (d, J= 8 Hz, 2H), 7.63 (td, J= 8.6, 1.2 Hz, 2H), 7.54 (td, J=8.0 Hz, 0.8 Hz, 2H) ppm. ^{13}C NMR (600 MHz, DMSO-d6): δ_C = 182.32, 130.95, 129.09, 128.23, 127.24, 127.21, 127.04, 126.49, 125.09 ppm. IR (ATR): 2965, 1775, 1730, 1621, 1531, 1442, 1479, 1409, 1347, 1262, 1163, 1108, 1016, 958, 891, 844, 781,733, 670 cm^{-1}.

7.4.2 Synthesis of tetramethylammonium trifluoromethanethiolate, $[NMe_4][SCF_3]$

$[NMe_4][SCF_3]$ was synthesized from previously reported methods[17, 18] as shown in Scheme S1. 0.900 g (25.0 mmol) sulfur and 0.900 ml (6.0 mmol) $TMSCF_3$ were added to 40.0 ml THF under Ar and cooled to -78 °C. Then 0.470 g $[NMe_4]F$ was added in one portion. The temperature was kept at less than -30 °C for the first 2 hours and allowed to recover slowly to room temperature in 6 hours. The color of the reaction mixture slowly changed from white to pale yellow as an orange-brown precipitate formed. A pink color in solution indicates a byproduct. The product is isolated by filtration and then rinsed with THF and CS_2 three times. Finally, a minimum amount of acetonitrile is added to the residue to dissolve it and then more than 20 ml of THF was used to precipitate the target. Finally, the pure $[NMe_4][SCF_3]$ was collected by filtration (yield: 87%).

$$TMSCF_3 + 1/8\ S_8 + [NMe_4]F \xrightarrow{\text{THF, -78°C}} [NMe_4][SCF_3] + TMS$$

Scheme 7.2 Synthesis of $[NMe_4][SCF_3]$ from tetramethylammonium fluoride at -78°C.

7.4.3 Synthesis $[NMe_4][CF_3COO]$ ligand

CF_3COOH (0.25ml, 3.2 mmol) and NMe_4OH (2.5 mL of a 0.1 M solution in H_2O) are added into a 20 vial. The mixture was stirred for 10 min at room temperature. H_2O was removed under reduced pressure (heating at 80 ºC). The product was further dried by heating at 70 ºC under vacuum for 15 hrs. Dissolve molecule in minimum amount of anhydrous acetonitrile and precipitated with anhydrous THF to remove extra acid. PH of $[NMe_4][CF_3COO]$ in acetonitrile is tested under argon as 6-8 indicating completely remove free acid.

7.5 Photophysical properties of anthracene derivatives

7.5.1 The fluorescence quantum yield (Φ_F) of ACA and ADTC isomers

With DPA in cyclohexane at room temperature as standard (λ_{ex}= 350 nm), Φ_F of all isomers were measured at room temperature in anhydrous THF. Firstly, 4 or 5 samples with optical densities ranging from 0.02, 0.04, 0.06, 0.08 to 0.10 at 350 nm for each molecule were made in an air- and water- free manner (including DPA); Then, the fluorescence spectrum (λ_{ex}= 350 nm) of these solutions in 10 mm path length cuvettes were recorded. The integrated fluorescence intensity was calculated. Lastly, the integrated fluorescence intensity vs absorbance was plotted, and the slope of this line recorded. eq. 7.1 was applied to calculate the Φ_F. Table 7.1 also lists the absorption and emission maxima (λ_{ex}=350 nm) in THF. As shown in Table 7.1, different isomers have different absorption maxima even though they share the same anthracene core.

$$\Phi_{\mathrm{F,sample}} = \Phi_{\mathrm{F,standard}} \cdot \left(\frac{\text{Gradient of sample}}{\text{Gradient ofstandard}}\right) \cdot \left(\frac{\eta_{\text{standard solvent}}}{\eta_{\text{sample solvent}}}\right)^2 \qquad \text{eq. 7.1}$$

Table 7.1 Fluorescence quantum yield of ACA and ADTC isomers in anhydrous tetrahydrofuran with DPA in cyclohexane as standard at room temperature. The absorption maxima, λ_{max}, and the corresponding extinction coefficients, ε_{max}, from experiment are listed, as well as the emission maxima, λ_{em}, of the six ligands in THF.

Transmitters	1-ACA		2-ACA		9-ACA		1-ADTC		2-ADTC		9-ADTC		DPA
Φ_F (%)	21.2		48.7		43.2		0.03		1.2		0.05		86^a
λ_{max}/nm & ε_{max}/ L•mol^{-1}•cm^{-1}	346	4040	338	4250	329	3090	330	16200	336	44814	353	1926	-
	361	5850	355	4780	345	6050	348	24808	353	33857	371	3632	-
	377	6450	373	5240	362	8870	366	36104	379	31274	391	3853	-
	395	5030	393	5340	382	7850	386	37134	401	37423	414	3429	-
λ_{em}/nm	423, 442		406, 428		451		425, 445		438, 481		423, 444		404, 425
a., reported Φ_F of DPA in cyclohexane. [19]													

7.5.2 Phosphorescence spectra of ACA and ADTC isomers

Following Reineke's work[20], phosphorescence spectra were measured at room temperature. All anthracene isomers were first dissolved in methoxybenzene (10 mg/L) and then mixed with the 10 mg/L 4BrPS in methoxybenzene to make a final solution with 2 wt% of anthracene (ACA isomers or ADTC isomers) in 4BrPS. A thick film was dropcast on a glass substrate and heated to 80°C until the solvent evaporated. It is probable that such thick films will introduce significant re-absorption of the fluorescence, owing to the small Stokes-shift. Thus, the high-energy side of the fluorescence spectra is artificially reduced in our measurements. In Table 7.2, the T_1 to S_0 and the T_2 to T_1 transitions of different anthracene derivatives are shown. For T_1 to S_0, these peak positions are in agreement with Kasha's report of 0, 0 vibrational frequencies of the T_1 to S_0 transition in various anthracenes at 77 K in a rigid glass solution. [21] The T_2 to T_1 transition in solid state is consistent with Kellogg's transient absorption measurements at 298 K in poly (methyl methacrylate) rods for anthracene crystals.[22]

Table 7.2 The S_1 to S_0 transition, T_1 to S_0 transition and T_2 to T_1 transition of anthracene and its derivatives when measured as thin film and embedded in 4-BrPS at 23°C.

Molecules	Peak of S_1 to S_0 /nm	Energy/eV	Peak of T_1 to S_0 /nm	Energy/eV	Peak of T_2 to T_1 /nm	Energy/eV
Anthracene	410	3.019	674	1.840	877	1.442
9-ACA	468	2.645	685	1.810	885	1.414
2-ACA	449	2.757	680	1.823	877	1.400
1-ACA	456	2.714	687	1.805	856	1.414
9-ADTC	453	2.732	664	1.868	915	1.378
2-ADTC	429	2.885	664	1.868	900	1.355
1-ADTC	464	2.668	668	1.856	T1-T2	1.448

7.6 ligand exchanges details and average number of functional ligands of CdSe+ anthracene derivatives

7.6.1 Ligand exchange 2.4 nm CdSe with ACA and ADTC isomers

Ligand exchange in the mixture of THF: toluene =1:1 (v/v) for 12 hours was performed for the ACA ligands. 12 hours is enough for ACA isomers to achieve equilibrium between the number of ligands on the CdSe NCs surface and number of free ligands in the solution. Ligand exchange requires 120 mins for 1-ADTC and 2-ADTC and 40 mins for 9-ADTC to get the highest $\Phi_{upconversion}$ in NMP. During ligand exchange, the concentration of CdSe NCs were kept at 57.5 µmol/L and the concentration of ligands varied to optimize the $\Phi_{upconversion}$.

7.6.2 N, the average number of ligands bound on a CdSe NCs.

The average numbers of bound anthracene ligands after ligand exchange was determined with UV-Vis absorption.[1] Fig. 7.1 shows that the ADTC isomers have more bound ligands than ACA isomers. 9-ADTC has up to 16 ligands on the CdSe surface, yet 9-ACA has only no more than 4 ligands on the CdSe NC surface. Interestingly, both ligands at 9- positions (red) shows that the ligands loading¸ N, is proportional to the concentration of ligands, whereas N at 1- and 2- positions at first increase to the maximum number of ligands and then decrease with a continued increase in the concentration of ligands. Moreover, we also found that the solubility of these ligands in THF is 9- > 1- > 2-. We hypothesize that 9-, 1- and 2- isomers bind on different types of Cd^{2+} sites on the CdSe NCs.

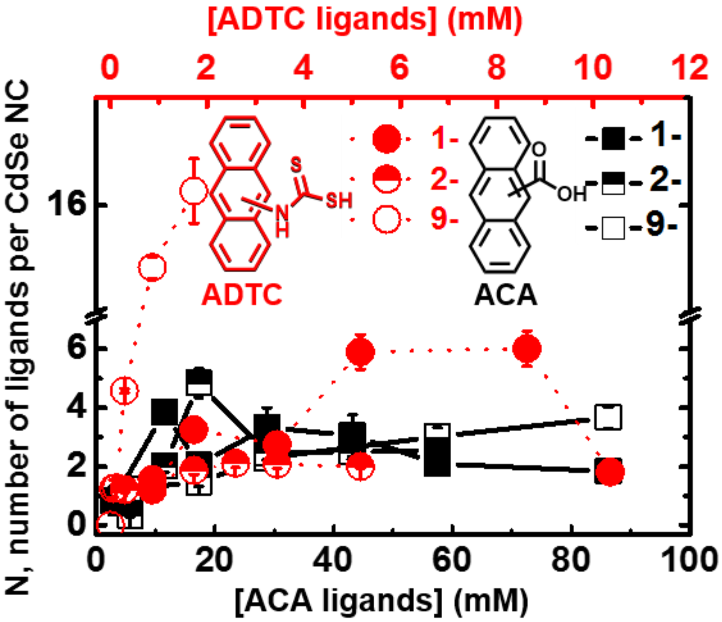

Fig. 7.1 The relationship between N, the average number of bound ligands per CdSe quantum dot against various concentrations of anthracenecarboxylic acid (ACA) (black square, solid line) and anthracene dithiocarbamate acid (ADTC) (red circle, dotted line) isomers.

7.7 Ligand exchange of 3.3 nm PbS QDs with pFA, $[NMe_4][SCF_3]$ and $NaSCF_3$ and characterization of surface ligand coverage

7.7.1 ligand exchange PbS QDs with short ligands conditions

For PbS@pFA, PbS in toluene (142.14 µM) and pFA in THF were mixed for a final concentration of [PbS] =38.26 µM and [pFA]e= 1.91 mM. The PbS QDs crash out after 40 mins of stirring without the addition of any bad solvent. The sample was centrifuged at 7830 rpm for 1 min, and the supernatant removed. The pellet was redispersed in $PhCF_3$ and kept under Ar(g) till further use. The PbS@pFA pellet cannot be redispersed in toluene, but easily redisolves in $PhCF_3$.

For $PbS@SCF_3$, PbS in toluene (142.14 µM) and $[NMe_4][SCF_3]$ in acetonitrile were mixed for a final concentration of [PbS] =38.26 µM and $[[NMe_4][SCF_3]$ = 1.53 mM. The mixture was stirred for 40 min. and kept under Ar(g) till further use.

For $PbS@SCH_3$, the procedure is the same as for $PbS@SCF_3$ except that the ligand exchange solution employed ethanol. Details are shown in Table S1.

Table 7.3 Details of ligand exchange of PbS QDs with different lgiands

Ligand exchange	[Ligand]/[QD]	ligand	[Ligand]	Solvent for ligand
PbS@pFA	50	pFA	4.09	THF
$PbS@SCF_3$	40	$[NMe_4][SCF_3]$	39.5	acetonitrile
$PbS@SCH_3$	40	$NaSCH_3$	49.4	ethanol

7.7.2 Dielectric constant of ligand shell affects absorption and emission of QDs

The absorption and emission spectra are shown in Fig 5.1b and the first absorption maximum and PL maximum are in Table 4.1. As we explained in the main paper, the dielectric constant affects the Stokes shift of the QD, which is explained with the Lippert-Mataga equation.[3]

Table 7.4 The dielectric constant, ε, and refractive index, n, of solvents corresponding to the newly installed ligands on the PbS QDs. For oleic acid, OA, $C_{15}H_{32}$ is similar to the main carbon chain on the ligand shell. As for pFA, the dielectric constant data of $C_{15}F_{32}$ is not available, so the values for C_8F_{18} were used in place. The Lippert-Mataga equation predicting the Stokes shift is $\Delta f(n)= (\varepsilon -1)/(2\cdot\varepsilon +1)-(n^2-1)/(2\cdot n^2+1)$. Here, Δf(n) is calculated considering that the native OA is completely replaced with the new ligand. The experimental Stokes shift and full width of half maximum (FWHM) of the PL of PbS@ligand complexes are shown here, with all samples measured in toluene at RT with photo-excitation at 532 nm, except for PbS@pFA measured in $PhCF_3$.

Solvent					PbS@Ligand		
	Condition	ε	n	Δf(n)	Ligand	Stokes shift/nm	FWHM[a]/ nm
CF_4	273 K, 10^5 Pa	1.287[23]	1.00049[24]	0.0800	$PbS@SCF_3$	199	199
CH_4	298 K, 8006 MPa	1.064[25]	1.00044[26]	0.0234	$PbS@SCH_3$	103	155
$C_{15}H_{32}$	298 K	2.04[27]	1.431[28]	0.0003	PbS@OA	89	67
C_8F_{18}	295 K	1.814[29]	1.282[30]	0.0550	PbS@pFA	120	64

7.7.3 NMR spectra of PbS@ligand complexes

^{1}H NMR and ^{19}F NMR spectra of the free ligand and PbS@ligand was obtained at room temperature. 20 μL of ferrocene solution (2.3 mg ferrocene in 0.3 ml toluene-d_8) was added to the NMR samples as an ^{1}H NMR internal standard. 2 μL $PhCF_3$ is added as an ^{19}F NMR internal reference. The ^{1}H NMR spectra of PbS@ligand complex are shown in Fig. 7.2, where the ferrocene reference peak is at 4.00 ppm. The solvent combinations used for NMR are in Table S5.

$[NMe_4][SCF_3]$ was also applied to functionalize CdS and CdSe QDs with native OA ligands. In Fig. 4.2 (c) and Fig. 7.2 below, SCF_3 capped CdS and CdSe QDs show chemical shifts at 43.9 ppm and 44.1 ppm respectively, which is very close to the chemical shift of $-SCF_3$, 43.3 ppm, when bound to PbS QDs. Moreover, ^{19}F NMR of CdS QDs after ligand exchange with $[NMe_4][SCF_3]$ shows both bound $-SCF_3$ (43.9 ppm) and free $-SCF_3$ (-10.3 ppm) in mol/mol $CDCl_3$: CD_3CN =5:1. In Fig. 4.2d, pFA binding to PbS QDs is seen in the broad molecular resonances at -81.7 ppm, -119.6 ppm, -122.4 ppm, -123.5 ppm and -126.95 ppm.

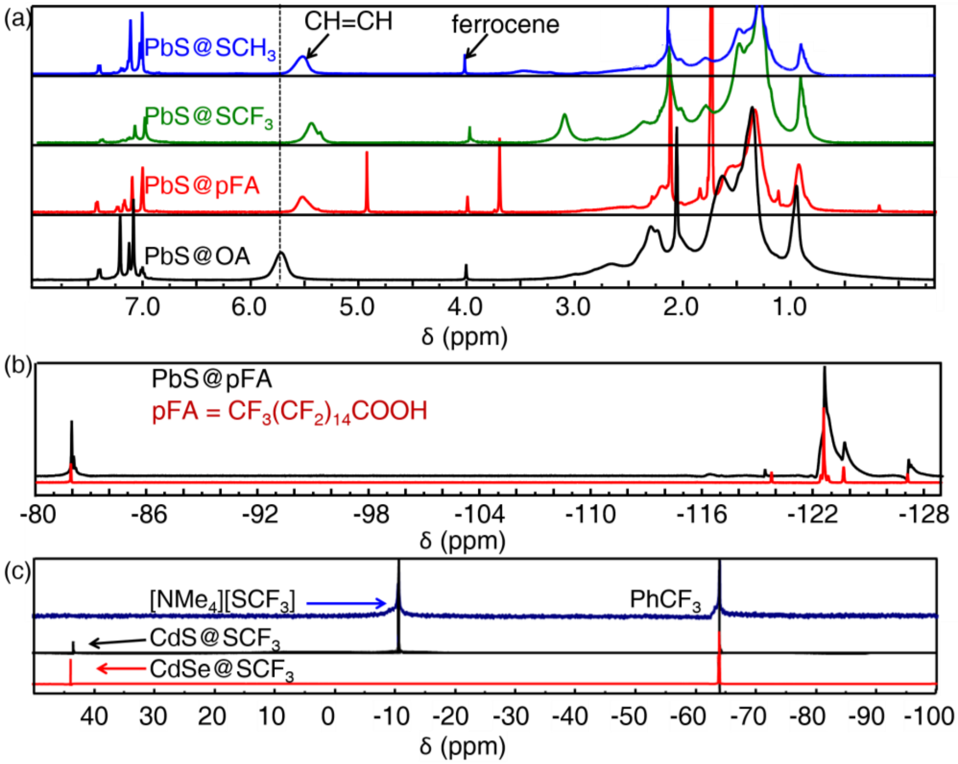

Fig. 7.2 (a) ^{1}H NMR spectra of PbS@ligand, normalized with the ferrocene internal standard. (b) ^{19}F NMR of pFA (red) and PbS@pFA (black) in deuterated toluene: acetone= 5:1 with $PhCF_3$ as the internal standard. The two sharp peaks at 3.70 ppm and 4.95 ppm are from impurities belonging to as-supplied pFA. (c) ^{19}F NMR of $[NMe_4][SCF_3]$ (violet), CdS@SCF$_3$ (black) and CdSe@SCF$_3$ (red) in deuterated chloroform: acetonitrile= 5:1 with $PhCF_3$ as the internal standard.

Table 7.5 Ligand composition for the PbS QDs used for cyclic voltammetry and photo-induced electron transfer measurements was measured by NMR. $I_{OA} = \frac{integration\ of\ the\ resonace\ peak\ at\ 5.6\ ppm}{integration\ of\ ferrocene\ resonance\ peak\ \ at\ 3.90\ ppm}$, in which the peak at 5.60 ppm is corresponding to the alkenes on OA and the peak at 4.00 ppm is ferrocene resonance. This allowed the ratio of OA with respect to QD to be calculated, and therefore the amount of OA replaced by ligand exchange.

Complex	Solvent	I_{OA}	OA/mol	Remaining OA (%)	[ligand]/[OA]
PbS@SCH$_3$	Toluene-d$_8$: DMSO-d$_6$=5:1	13.82	4.09E-03	67.5	0.325
PbS@SCF$_3$	Toluene-d$_8$: CD_3CN=5:1	14.82	4.38E-03	72.4	0.276
PbS@pFA	Toluene-d$_8$: acetone-d$_6$=5:1	13.28	3.93E-03	64.9	0.351
PbS@OA	Toluene-d$_8$	20.47	6.05E-03	100	0

7.8 Surface Functionalization of Si Nanocrystals (NCs)

7.8.1 Si:C18: Hydrosilylation of Si NCs with 1-octadecene (ODE)

Si NCs were synthesized by a non-thermal plasma.[1] After synthesis, as-prepared Si NC powder was transferred to a glove box and kept under nitrogen for future use. 1.0 mg Si NC powder, 10 mL mesitylene and 2.00 mL ODE (6.25 mmol) was added to a 50 mL single-neck air-free Schlenk tube (Chemglass Life Sciences) in a glovebox (water < 0.5 ppm, oxygen < 0.2 ppm) and sealed with a glass stopper. The Schlenk tube is transferred out of the glovebox and heated to 175 °C (under reflux) with an oil bath under a dynamic flow of dry Argon. The cloudy mixture turns clear in the first 10 – 20 mins indicating Si NCs are partially functionalized with ODE. After tuning clear, the reaction was continued another 3 hours. After completion, the clear yellow reaction mixture was taken back into the glovebox for cleaning. Toluene and methanol were added to the mixture (mixture: toluene: methanol = 1:1:2 by volume) to precipitate out the NCs by centrifuging at 7830 rpm for 30 mins. The precipitated NCs are then redispersed in 5 mL of toluene, followed by addition of 5 mL of methanol and centrifuged at 7830 rpm for 30 mins again. This cleaning procedure was repeated three times with a shorter centrifuge time, 15 mins, and the final pellet redispersed in toluene for future use. The average diameter of the Si NCs is calculated from the peak position of their photoluminescence (PL) maxima, denoted as λ_{ems}, using a sizing curve from Wheeler et al.[2]

7.8.2 Si:9EA: Hydrosilylation of Si NCs with ODE and 9VA

The same reaction as above was performed except that 9VA is added in addition to ODE. Si:9EA is synthesized with 1.00 mg Si NC, 10.0 mL mesitylene, 2.00 mL ODE (6.25 mmol) and 25.5 mg 9VA (0.125 mmol) (moles of 9VA/moles of (ODE+9VA) = 2%). The cleaning procedure is the same as before.

7.8.3 Absorption Spectra of Si:C18 and Si:9EA

Absorption spectra of Si:C18 and Si:9EA in toluene were measured (Fig. 7.3) and absorption by surface-bound 9VA isolated by removing contributions to the Si:9EA absorption spectrum from the Si NCs themselves. This was done by subtracting the absorption of Si:C18 (red dotted) from that of Si:9EA (black) following normalization of the two traces in a spectral region where 9EA does not absorb (550 - 700 nm). Peaks in the absorption profile of surface-bound 9EA (blue dashed dot) display a 55 meV red-shift relative to a reference anthracene compound, dilute 9-methylanthracene (9MA) in solution (green dashed).

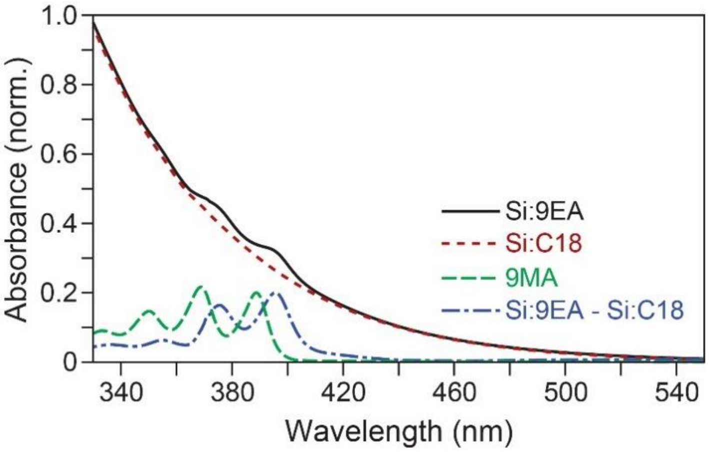

Fig. 7.3 Absorption spectra of Si:C18 (red dotted) and Si:9EA (black). Difference spectra (blue dashed dot) attributed to surface-bound 9EA show a 55 meV red-shift compared to dilute 9MA in solution (green dashed). All measurements were performed in toluene at room temperature.

7.8.4 Estimating the Average Number of 9-ethylanthracenes Bound to Each NC, $\langle N_{9EA} \rangle$

The concentration of 9EA molecules bound to Si NCs, [9EA], was calculated from the difference spectra Fig. 7.3) using the extinction coefficient of 9MA (denoted as ε_{9MA}) at 352, 369 and 389 nm in toluene. The extinction coefficient of 9MA in toluene was found to be 6305, 9345 and 8413 $M^{-1}cm^{-1}$ at 352, 369 and 389 nm respectively. The concentration of Si NCs, [Si NC], in toluene was calculated from the optical density (OD) at different wavelengths using extinction spectra from Carroll et al[3] reported for 6.5 nm diameter Si NCs, which were scaled for the smaller particles we investigate assuming a cubic dependence of NC extinction on their diameter (Table 7.6). Alternative methods considered for determining [Si NC] are discussed in Section 7B below. To estimate the extinction of 9VA in our Si:9VA samples, we need to first remove from their absorption spectrum contributions from Si NCs as they overlap with those of 9VA. This was done by normalizing a background absorption spectrum of unfunctionalized Si:C18 to that of Si:9VA over the range of 550 to 700 nm as the absorption of 9VA is negligible along this range. Subtraction of these two spectra provided a baseline from 600 – 800 nm that was exceptionally flat. We then used the extinction coefficient at 369 nm of free 9VA for the peak at 375 nm of Si-bound 9VA due to the red shift in absorption of 9VA upon binding to a NC surface (Fig. 7.3, blue dashed dot). The extinction coefficient of 3.1 nm diameter Si NCs at 488 nm, $\varepsilon_{\mathrm{NC,\ 488nm}} = 1.0 \times 10^4\ \mathrm{M^{-1}cm^{-1}}$,[3] is used to calculate the concentration of Si NCs as anthracene does not absorb at 488 nm.

$\langle \mathrm{N_{9EA}} \rangle$, the average number of NC-bound 9VA molecules within a Si:9EA sample was calculated as follows:

$$\langle N_{9EA} \rangle = \frac{[9EA]}{[Si\ NC]} = \frac{\left(abs_{Si:9EA,395nm} - abs_{Si:C18,\ 395nm} \dfrac{< abs_{Si:9EA} >}{< abs_{Si:C18} >} \right)}{\varepsilon_{9MA,389nm}} \Bigg/ \frac{abs_{Si:9EA,\ 488nm}}{\varepsilon_{Si\ NC,488nm}} \qquad \text{eq. 7.2}$$

Here, $\langle \mathrm{abs_{Si:C18}} \rangle$ and $\langle \mathrm{abs_{Si:9EA}} \rangle$ are the average OD of Si:C18 and Si:9EA from 550 nm to 700 nm respectively.

Table 7.6 Extinction coefficients of 6.5 nm Si NCs at various wavelengths were obtained from Carroll et al.[3] This allowed the corresponding values for the smaller particles used here to be calculated, assuming a cubic dependence of NC absorption on diameter.[4]

NC Diameter/nm	300 nm	488 nm	532 nm	640 nm
6.5	2.0×10^{6} (M·cm)$^{-1}$	8.8×10^{4} (M·cm)$^{-1}$	4.4×10^{4} (M·cm)$^{-1}$	8.5×10^{3} (M·cm)$^{-1}$
3.1	2.2×10^{5} (M·cm)$^{-1}$	1.0×10^{4} (M·cm)$^{-1}$	4.8×10^{3} (M·cm)$^{-1}$	9.2×10^{2} (M·cm)$^{-1}$

Table 7.7 $\langle N_{9EA}\rangle$, the average number of surface bound 9EA molecules per Si NC was obtained from absorption spectra. To determine this value, contributions to Si:9EA absorption spectra were first removed using the normalization scheme described above. This gives the OD at 395 nm, 374 nm and 356 nm stemming from 9EA which allows the ratio of [9EA]/[NC] to be calculated using these points. Our reported value of $\langle N_{9EA}\rangle$ represents the average value determined by comparing these three peaks to reported extinction spectra of 9VA. Samples used for TA and photon upconversion measurements were taken from the same Si:H batch, but subjected to different hydrosilylation reactions to attach 9EA. Despite this, they were found to bind similar numbers of 9EA molecules and experience similar levels of photoluminescence quenching upon 9EA attachment.

		Si:C18	Si:9EA TA sample	Si:9EA Upconversion sample
PLQY %		16.1 ± 2.2	9.2 ± 1.6	8.2 ± 1.2
[Si NC]/µM		3.12	2.47	1.70
[9EA]/µM	396 nm	-	6.10	4.53
	374 nm	-	5.15	3.90
	356 nm	-	4.34	4.76
N_{9EA}	396 nm	-	2.47	2.12
	374 nm	-	2.08	2.07
	356 nm	-	1.75	2.53
$\langle N_{9EA}\rangle$		-	2.1 ± 0.4	2.2 ± 0.3

7.8.5 Calculation of $\langle N_{exc}\rangle$, the Average Number of Times a NC is Excited per Second During Photon Upconversion under CW Illumination

Using experimentally determined parameters, e.g. the optical density of Si NCs at 488 nm: OD_{488nm}; the optical path length: d = 100 µm, etc., we first calculate the total number of photons absorbed by an ensemble of Si NCs per second under steady-state 488 nm illumination:

$$\frac{absorbed\ photons}{time} = \frac{power * \%\ photons\ absorbed}{energy\ per\ photon} = \frac{power * (1-10^{-OD_{488nm}})}{hc/\lambda}$$

$$= \frac{power * (1-10^{-OD_{488nm}})}{\left(6.626*10^{-34}\,J\bullet s\right)\left(3*10^{8}\,m/s\right)/\left(488\ nm\right)}$$

$$= \left(power\ \ in\ \ W\right) * (1-10^{-OD_{488nm}}) * \left(2.45*10^{18}\right)s^{-1} \qquad \text{eq. 7.3}$$

We calculate the number of NCs in the volume excited by the laser (beam radius, r, is ~110 μm) accounting for the 45° angle between the excitation beam and the cuvette:

$$N_{Si} = [Si\ NC] * Volume\ of\ cylinder * N_A$$

$$= \frac{OD_{488nm}}{\varepsilon_{488nm} * d} * \left(\pi * r^2 * \sqrt{2}\right) * d * N_A$$

$$= \frac{OD_{488nm}}{\left(1.0*10^{4}\,M^{-1}cm^{-1}\right)}\left(3.14\right)\left(110\,\mu m\right)^2\left(\sqrt{2}\right)\left(6.023*10^{23}\,mol^{-1}\right) \qquad \text{eq. 7.4}$$

$$= 3.2*10^{13} * OD_{488nm}$$

where N_A is Avogadro's number, N_{Si} is number of Si NCs in the excitation volume, and [Si NC] is the molar concentration of Si NCs in solution. Therefore, the average number of times a NC is excited per second, $\langle N_{exc} \rangle$, under 488 nm excitation is:

$$\left\langle N_{exc} \right\rangle = \frac{absorbed\ photons\ per\ unit\ time}{number\ of\ Si\ NCs\ in\ the\ excitation\ volume}$$

$$= \frac{\left(power\ \ in\ \ W\right) * (1-10^{-OD_{488nm}}) * \left(2.45*10^{18}\right)s^{-1}}{3.2*10^{13} * OD_{488nm}} \qquad \text{eq. 7.5}$$

$$= \left(\frac{1-10^{-OD_{488nm}}}{OD_{488nm}}\right) * \left(power\ \ in\ \ W\right) * \left(7.7*10^{4}\right)s^{-1}$$

These calculations are used to obtain values of $\langle N_{exc} \rangle$ shown in Fig 5.2c of the main text and Fig. 7.6a below.

7.9 PbS thin film fabrication via spin-coating and dip-coating

7.9.1 Superlattice Fabrication via spin-coating

OA and ⊖SCF$_3$ capped PbS QDs (molar ratio of OA: ⊖SCF$_3$= 2:1) (PbS–OA+SCF$_3$) are synthesized via solution partial ligand exchange with OA capped PbS QD with [NMe$_4$][SCF$_3$].[31] Briefly, 0.68 ml PbS QDs in toluene ([PbS]=0.072 mM] is mixed with 52 µL [NMe$_4$][SCF$_3$] acetonitrile solution (concentration of [NMe$_4$][SCF$_3$]=6.9 mg/ml). 0.65 ml toluene is added such that [PbS] = 0.035 mM in the mixture and molar ratio of [NMe$_4$][SCF$_3$] to PbS QD = 40. This is stirred for 40 mins at room temperature. Under these conditions, one third of OA is replaced with ⊖SCF$_3$ (ligand replacement was measured by NMR in our previous work[31]). The QDs were filtered with a Minisart SRP (Hydrophobic PTFE) syringe filter with 0.2 µm pore size. Then 1.5 ml acetone is added to precipitate the PbS QDs by centrifuging at 7830 rpm for 10 mins. The supernatant was removed, and 1.0 ml toluene used to redisperse the QDs such that [PbS] = 0.050 mM. These partially ligand-exchanged colloidal PbS QD were drop-cast in a nitrogen glovebox on substrates (like silicon wafers with either thermal or native oxides, glass and silicon dioxide TEM grids) coated with self-assembled monolayers (SAMs), e.g. 3-MPTMS. 3-MPTMS serves to promote the adhesion of the PbS QDs to silicon dioxide. The 3-MPTMS treatment or PFDTEOS treatment (denoted as perfluoro treatment) of substrate is described before. Two consecutive ligand exchanges were performed on this thin film, where 2 mg/ ml of [NMe$_4$][SCF$_3$] in acetonitrile was allowed to equilibrate for 5 minutes on the QD thin film. Excess ligand was removed by spin-coating, followed by three washing steps: twice with ethanol and finally with tetrahydrofuran. ATR-IR measurements of PbS–SCF$_3$ verify the complete removal of OA after two cycles of ligand exchange in thin film.

7.9.2 PbS–SCF_3 film fabricated via dipcoating

The PbS–OA QDs were either dropcast on glass (with 3-MPTMS treatment) for optical samples to get a thicker thin film or spincoated on silicon wafer to fabricate a homogenous thin film for transistor measurements. The film is soaked in 2 mg/ml $[NMe_4][SCF_3]$ acetonitrile solution for 15 mins to completely remove OA, then rinsed with acetonitrile twice. Acetonitrile is removed by spinning the substrate at 1500 rpm and cleaned twice with ethanol and once with tetrahydrofuran (removed by centrifugation).

7.10 Stern-Volmer quenching of PbS@ligand complexes by benzoquinone

Photoluminescence of PbS@ligand complex with different concentrations of benzoquinone, [BQ], from 0 to 300 μM, was obtained with samples being sealed in air-tight cuvettes. The concentration of PbS QD was kept at 0.244 μM. In Fig. 7.4, the PL of PbS@ligand complexes decreases due to photo-induced electron transfer from the PbS QDs to BQ.

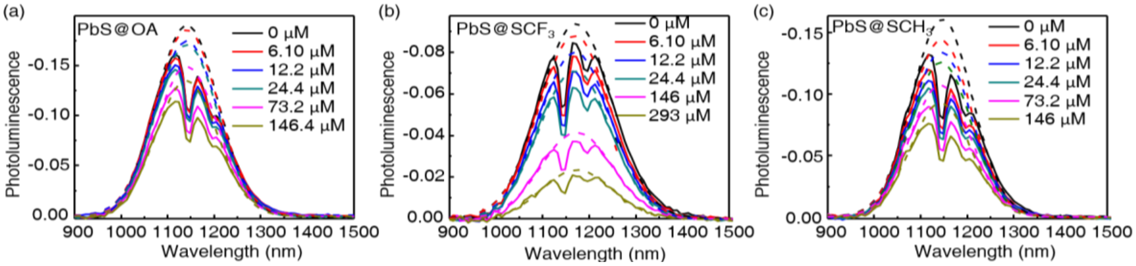

Fig. 7.4 . Steady-state PL spectra of a solution of the PbS QDs in the presence of various amounts of benzoquinone, [BQ] ranging from 6.10 μM to 300 μM in toluene. (a) PbS@OA, (b) PbS@SCF_3 and (c) PbS@SCH_3. Here, the concentration of PbS QD is fixed at 0.244 μM and with photoexcitation at 532 nm. The solid line is experimental data and the dips between 1100 nm to 1200 nm are due to the absorption of toluene. Here the dashed line is the corresponding PL after correcting for the absorption of toluene.

7.11 Steady states upconversion of quantum dots with transmitters

7.11.1 The upconversion emission spectra of various concentration of ligands in ligand exchange solution.

All upconversion experiments are conducted in hexane since it gives high $\Phi_{upconversion}$ compared to other solvents[32]. Fig. 7.5 shows the emission of DPA and CdSe NCs during photon upconversion as the concentration of ligands in the ligands exchange solution is increased.

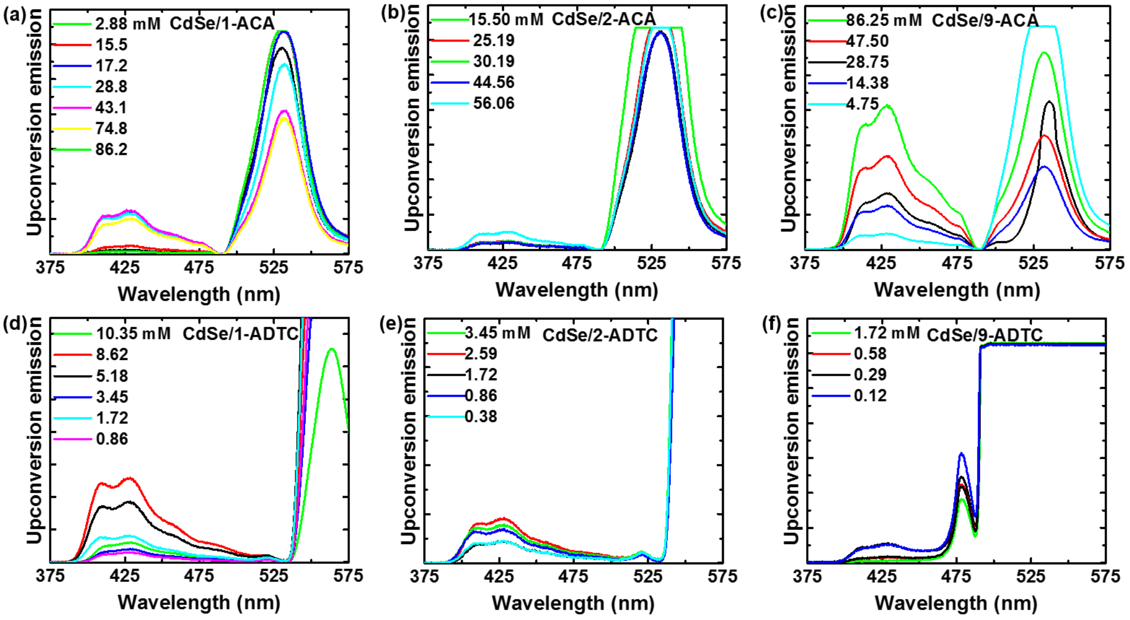

Fig. 7.5 The normalized emission of DPA and photoluminescence of CdSe nanocrystals (NCs) in this hybrid upconversion platform. CdSe NCs serve as sensitizers while DPA is the annihilator emitting the upconverted light. In general, the upconverted emission increases with the concentration of the ligand exchange solution (listed in mM). The different anthracene isomers are the (a) 1-anthracenecarboxylic acid (1-ACA); (b) 2-ACA; (c) 9-ACA; (d) 1-anthracene dithiocarbamate (1-ADTC); (e) 2-ADTC and (f) 9-ADTC. Upconversion sample was strictly air-free and excited with 12.7 W/cm^2 532 nm or 488 nm laser at room temperature. During ligand exchange, the concentration of CdSe was kept as 57.5 µmol/L while the concentration of ligands was varied as shown above to optimize the $\Phi_{upconversion}$.

7.11.2 Photon Upconversion with Si:9EA as a Triplet Photosensitizer

20 µL of 3.1 – 3.3 nm diameter Si NCs in toluene (with OD at 488 nm being 0.3) is added to 30 µL of DPA ([DPA] =8.7 mM in toluene) such that the OD at 488 nm of the Si NCs are in the range of 0.1 to 0.2 and [DPA] = 5.2 mM. Solutions are housed in a clean borosilicate capillary tube (0.1 mm × 2.0 mm, Friedrich & Dimmock, Inc., LRT-010-2-10), resulting in a

100 μm optical path length. Fig 5.2 of the main text describes photoluminescence (PL) detected under 488 and 532 nm excitation conditions. For completeness, Fig. 7.6 displays PL collected under 640 nm illumination from a Si:9EA sample with $\langle N_{9EA} \rangle = 2.2 \pm 0.3$ as the 640 nm excitation power is varied. PL from both from DPA and Si NCs are detected.

The quantum yield for photon upconversion (upconversion QY%, Φ) is given by

$$\begin{aligned} \Phi_{UC} &= 2 * \Phi_{reference} * \frac{photon\,aborbed\,by\,reference}{photon\,absorbed\,by\,upconversion} * \frac{PL\,of\,upconversion}{PL\,of\,reference} \\ &= 2 * \Phi_{R6G} * \frac{n_{DPA}^2}{n_{R6G}^2} * \frac{[Area]_{DPA}}{[Area]_{R6G}} * \frac{1-10^{-OD_{R6G}}}{1-10^{-OD_{\mathrm{Si}\,NC}}} \end{aligned} \qquad \text{eq. 7.6}$$

Our group has reported on the calculation of the upconversion QY% previously.[5] Here Rhodamine 6G (R6G) with 95% fluorescence quantum yield is used as a reference.

$$\begin{aligned} \Phi_{UC} &= 2 * \Phi_{reference} * \frac{photon\,aborbed\,by\,reference}{photon\,absorbed\,by\,upconversion} * \frac{PL\,of\,upconversion}{PL\,of\,reference} \\ &= 2 * \Phi_{R6G} * \frac{n_{DPA}^2}{n_{R6G}^2} * \frac{[Area]_{DPA}}{[Area]_{R6G}} * \frac{1-10^{-OD_{R6G}}}{1-10^{-OD_{\mathrm{Si}\,NC}}} \end{aligned} \qquad \text{eq. 7.6}$$

Where Φ_{RG6} is the fluorescence quantum yield of R6G, n_{DPA} and n_{RG6} represent the refractive indices of the solvents for the DPA upconversion sample and R6G, which are toluene and ethanol, respectively. $[Area]_{DPA}$ and $[Area]_{R6G}$ are the integrated areas of the fluorescence peaks of DPA and R6G. OD_{DPA} and OD_{R6G} denote the absorbance of Si NCs and R6G at the emission excitation wavelength.

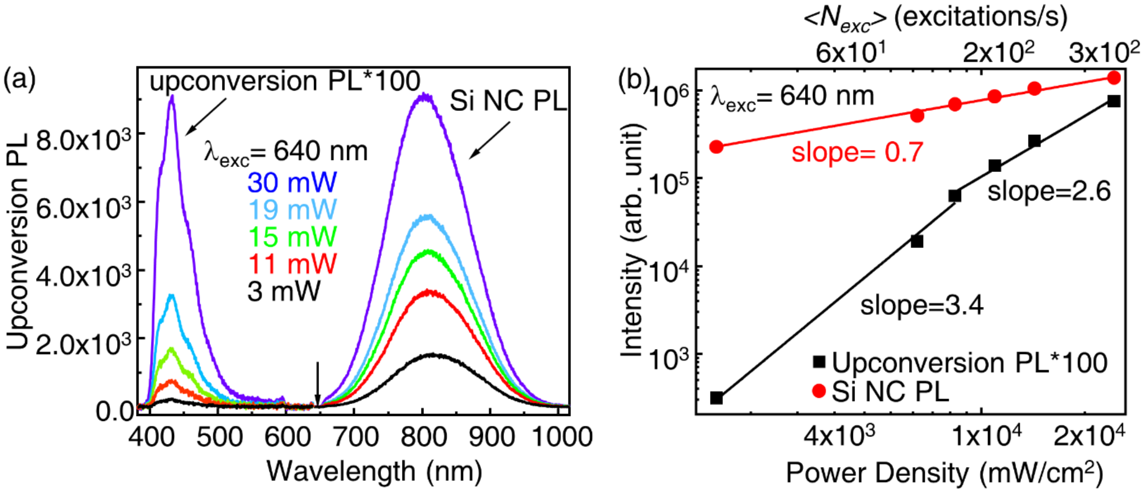

Fig. 7.6 (a) Photoluminescence spectra of Si:9EA under 640 nm excitation ([DPA] = 5.2 mM, $\langle N_{9EA}\rangle$ = 2.2 ± 0.3, 3.2 nm diameter Si NCs) in toluene at RT. The maximum upconversion QY% is 0.10 + 0.07%. (b) Power dependence of the DPA emission (black squares) and Si NC PL (red circles) during photon upconversion employing 640 nm photons. Here, we see no clear evidence of interconversion from a quadratic to a linear dependence of the upconversion intensity on the incident photon power density over the range measured due to the negligible absorption of Si:9EA at 640 nm (OD ~ 0.007 at 640 nm for the investigated sample), which prevents $\langle N_{exc}\rangle$ from achieving values where linear power dependence begins to emerge (Fig. 3.2c).

7.12 Time-correlated photoluminescence measurement of PbS@ligand photoluminescence (PL) in the presence of BQ

The PL decay of the PbS@ligand complexes in toluene (PbS@SCF_3 and PbS@SCH_3) and in $PhCF_3$ (PbS@pFA) with different concentrations of BQ, between 0 mM to 3 mM are shown here. Fig. 7.7 shows TCSPC data where QD lifetimes are shortened as the concentration of BQ increases. The PL decay is well described with a bi-exponential fit (eq. 7.7) from which the amplitude averaged lifetime, <τ>, is calculated from eq. 7.8. For eq. 7.7, eq. 7.8and eq. 7.9 , $\tau_{i, (i=1,2)}$ is the lifetime and $A_{i, (i=1,2)}$ is the corresponding amplitude. The parameters extracted from the bi-exponential fit are listed below in eq. 7.7.

$$f(t) = A_1 \cdot \exp\left(-\frac{t}{\tau_1}\right) + A_2 \cdot \exp\left(-\frac{t}{\tau_2}\right) \qquad \text{eq. 7.7}$$

$$\langle\tau\rangle = \sum A_i \cdot \tau_i / \sum A_i \qquad \text{eq. 7.8}$$

$$\bar{\tau} = \sum A_i \cdot \tau_i^2 / \sum A_i \cdot \tau_i \qquad \text{eq. 7.9}$$

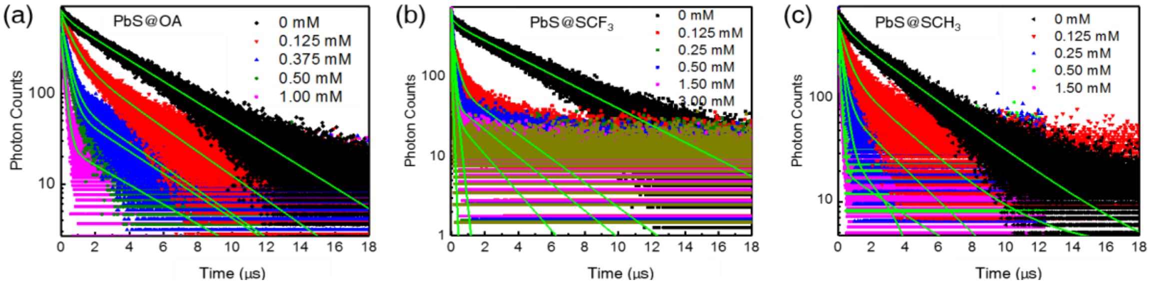

Fig. 7.7 Time-resolved photoluminescence (PL) decay of PbS@OA-(a), PbS@SCF$_3$-(b) and PbS@SCH$_3$-(c) in toluene with [PbS] =5 μM in the absence (black) and presence of different concentrations of BQ, [BQ]. The green solid line is the fit with a bi-exponential decay.

Table 7.8 Bi-exponential fits of the TCSPC data with equation of eq. 7.8. $\langle\tau_0\rangle$ is the intrinsic amplitude averaged lifetime of PbS@ligand complexes. $\langle\tau\rangle$ is the amplitude averaged lifetime of the QD with different concentrations of BQ, calculated from eq. 7.8. $\bar{\tau}_0$ is the intrinsic intensity averaged lifetime of PbS@ligand complex and $\bar{\tau}$ is the intensity averaged lifetime of the QD with different concentrations of BQ, calculated from eq. 7.9.

	[BQ]/mM^{-1}	A_1	τ_1/μs	A_2	τ_2/μs	$<\tau>$	$<\tau_0>/<\tau>$	$\bar{\tau}$	$\bar{\tau}_0/\bar{\tau}$
PbS@ OA	0	0.13	0.43	0.87	3.45	3.06	1.00	3.40	1.00
	0.125	0.54	0.69	0.68	3.50	2.74	1.12	3.12	1.09
	0.375	0.82	0.36	0.18	4.80	1.15	2.66	3.65	0.93
	0.5	0.86	0.31	0.14	5.31	0.99	3.10	3.95	0.86
	1	0.91	0.19	0.09	5.11	0.63	4.89	3.76	0.90
PbS@ pFA	0	0	0	1.00	3.92	3.92	1.00	3.92	1.00
	0.125	0.38	0.54	0.62	3.24	2.22	1.77	2.99	1.31
	0.25	0.55	0.53	0.45	2.93	1.60	2.45	2.49	1.57
	0.5	0.27	2.82	0.73	0.41	1.05	3.71	2.14	1.83
	1.5	0.10	3.07	0.90	0.25	0.54	7.31	1.89	2.07
	3	0.94	0.17	0.06	3.21	0.35	11.26	1.85	2.11
PbS@ SCF$_3$	0	0.14	0.33	0.86	4.07	3.55	1.00	4.03	1.00
	0.125	0.78	0.28	0.22	2.84	0.84	4.25	2.16	1.86
	0.25	0.88	0.14	0.12	1.82	0.34	10.39	1.21	3.33
	0.5	0.93	0.10	0.07	2.27	0.24	14.68	1.44	2.80
	1.5	0.34	0.19	0.66	0.03	0.09	41.13	0.16	25.90
	3	0.44	0.07	0.56	0.01	0.04	96.64	0.06	65.24
PbS@ SCH$_3$	0	0.25	0.53	0.75	3.60	2.84	1.25	3.46	1.00
	0.125	0.68	0.46	0.32	2.92	1.25	2.85	2.31	1.50
	0.25	0.74	0.24	0.26	2.16	0.74	4.82	1.70	2.04
	0.5	0.92	0.22	0.08	3.47	0.48	7.46	2.11	1.63
	1.5	0.93	0.08	0.08	1.34	0.17	20.72	0.82	4.24

Table 7.8 Bi-exponential fits of the TCSPC data with equation of eq. 7.7. $\langle \tau_0 \rangle$ is the intrinsic amplitude averaged lifetime of PbS@ligand complexes. $\langle \tau \rangle$ is the amplitude averaged lifetime of the QD with different concentrations of BQ, calculated from eq. 7.8. $\bar{\tau}_0$ is the intrinsic intensity averaged lifetime of PbS@ligand complex and $\bar{\tau}$ is the intensity averaged lifetime of the QD with different concentrations of BQ, calculated from eq. 7.7.

7.13 Transient absorption measurements and analysis for CdSe/An derivatives

7.13.1 Power dependence of TA measurement

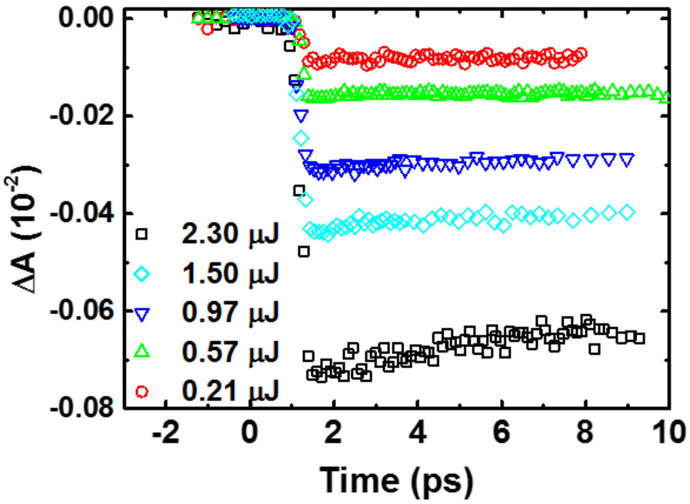

Fig. 7.8 The transient absorption kinetics (λ_{probe}= 505nm) of CdSe/ODPA dispersed in toluene at different excitation powers (λ_{ex}= 465nm): 0.21 μJ (red circle), 0.57 μJ (green triangle), 0.97 μJ (blue triangle), 1.5 μJ (cyan diamond) and 2.3 μJ (black square), verifying the power dependence in the amplitude of the sample. The TA spectra of the as-synthesized CdSe/ODPA (λ_{ex} = 465 nm) shows that there is a symmetrical decay at the first few picoseconds (Fig. 7.9) at high excitation densities. This observation can be explained by multi-exciton annihilation in the NCs. To avoid this, the pump power was kept as 0.3 μJ (> 30 fs full width at half maximum).

7.13.2 Femtosecond TA spectra were measured for all CdSe/ACA and ADTC complexes.

Femtosecond TA spectra were measured for all CdSe/ACA and CdSe/ADTC hybrid complexes as well as the native CdSe/ODPA NCs (Fig. 7.9 and Fig. 2.3a). Excitation was at 465 nm and the pump power was 300 nJ (>30 fs HWFM). In

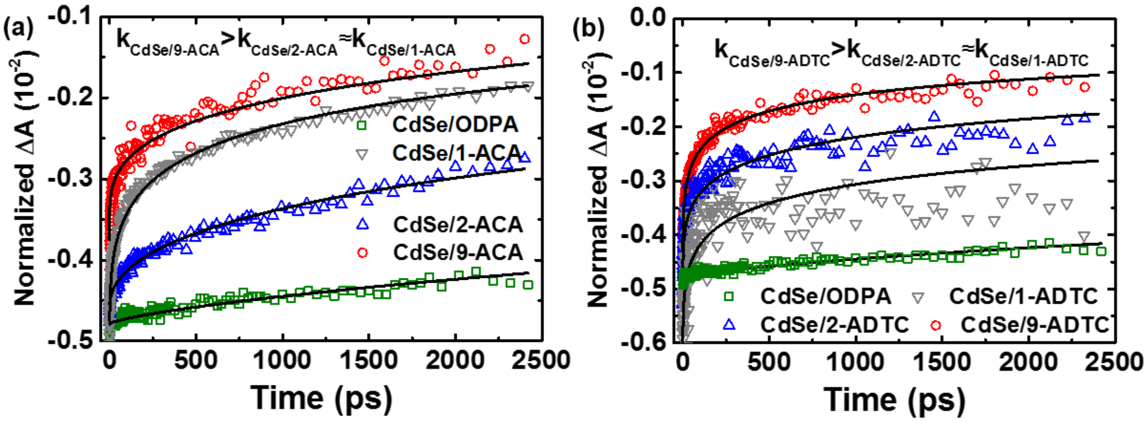

Fig. 7.10, comparing the ground state recovery of CdSe/ODPA NCs with CdSe/ACA or CdSe/ADTC hybrid complexes, there is much faster recovery for the ground state bleach for the CdSe NCs in the ACA or ADTC functionalized NCs. The measurements cover 2.4 ns after excitation and range from 430 nm to 800 nm, but the signal is noisy around 430 nm to 480 nm due to the scattering of the pump light. However, we can still see the growth of a new band at 433 nm, which corresponds to the triplet states of anthracene. Therefore, since no absorption associated with the radical cation or anion was observed, we can conclude that there is direct triplet transfer from excited CdSe NCs to the triplet state of surface bonded ACA or ADTC isomers.

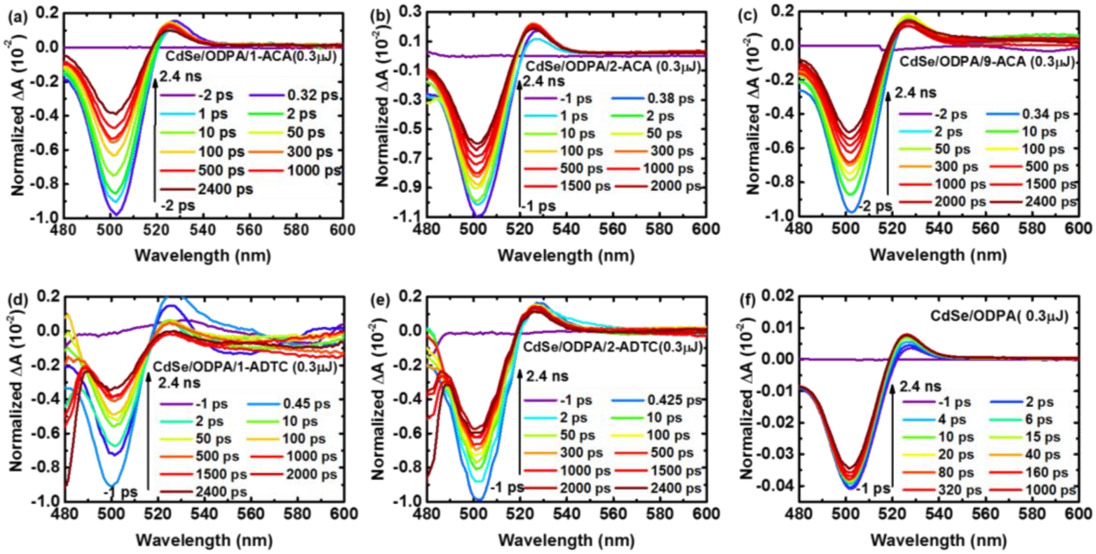

Fig. 7.9 Ultrafast transient absorption (TA) different spectra of (a) CdSe/1-ACA (a); (b) CdSe/2- ACA; (c) CdSe/9-ACA; (d) CdSe/1-ADTC; (e) CdSe/2-ADTC and (f) CdSe/ODPA, illustrating more rapid recovery of ground state of CdSe when binding with ACA or ADTC isomers. TA experiments were done by selectively exciting the CdSe NCs in toluene using 465 nm pulse laser (0.3 μJ per pulse, >30 fs FWHM).

7.13.3 Analysis of the kinetics of triplet energy transfer (TET), extracting the rate constant, kTET, and TET efficiency, ΦTET for the anthracene transmitters.

Kinetics were monitored at 505 nm and at 490 nm, which is close to the first excitonic peak of CdSe NC (Fig. S7). Other than triplet energy transfer to the anthracene transmitter, the initially populated CdSe excited states can be quenched by dark states or trap states. Thus a stretched exponential function was used to capture the rate of TTET[33]. The kinetic traces obtained from ultrafast TA experiments were fit using equation S2, S3 and S4; results from these fitting procedures are shown in Table 1 and Table S3, Fig. 3a and 3b for 505 nm, and in Fig. S4 for 490 nm.

$$\Delta A = A \cdot \exp((-\left(\frac{t}{\tau}\right)^{\beta}) \qquad \text{eq. 7.10}$$

Where A and τ are the amplitude and the stretched lifetime respectively, corresponding to the TET between CdSe and the surface-bound acceptor. β is the stretching exponent. Using

$$\langle \tau \rangle = \frac{\tau}{\beta} \mathrm{n}\Gamma\left(\frac{1}{\beta}\right)$$ eq. 7.11

The average weighted lifetime, , was calculated using τ and β.

$$\langle k \rangle = \frac{1}{\langle \tau \rangle} - \frac{1}{\langle \tau_0 \rangle}$$ eq. 7.12

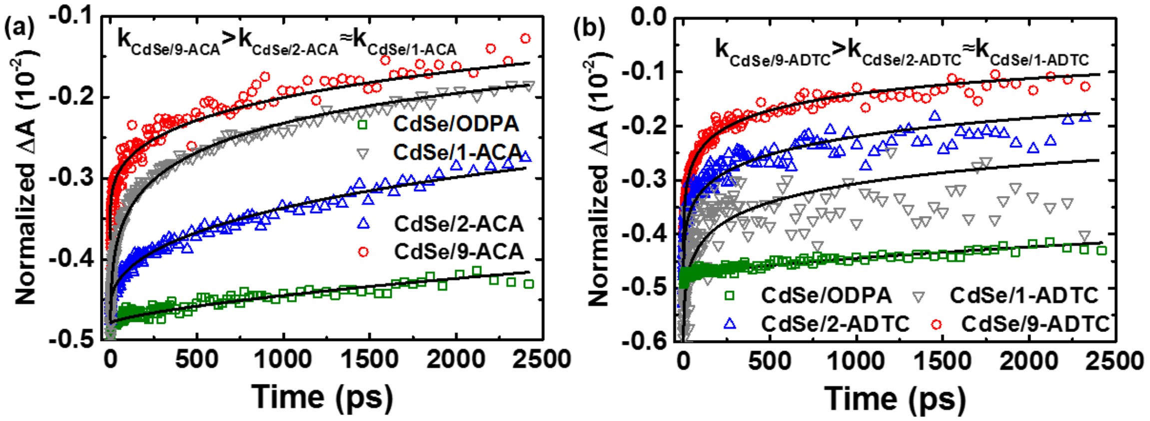

Fig. 7.10 Ground state recovery of CdSe NCs investigated by kinetics at 490 nm, illustrating much faster quenching in (a) anthracenecarboxylic acid (ACA) functionalized CdSe NCs. Native octadecylphosphonic acid functionalized CdSe NCs (ODPA, green square), 1-ACA (grey triangle), 2-ACA (blue triangle) and 9-ACA (red circle) isomers; and (c) 9-anthracene dithiocarbamate (ADTC) functionalized NCs, 1-ADTC (grey triangle), 2-ADTC (blue triangle) and 9-ADTC (red circle). The black solid line is the fit.

7.13.4 Fitting parameters of TA at 490 nm

Table 7.9 Fitting parameters of transient absorption ground state bleach at 505 nm with eq. 7.12 and eq. 7.13.

Transmitter	β	τ/ ns	<τ>/ns
CdSe/ODPA	0.66	29.9	39.9
CdSe/1-ADTC	0.24	1.30	39.7
CdSe/2-ADTC	0.25	1.60	39.9
CdSe/9-ADTC	0.20	0.18	19.5
CdSe/1-ACA	0.24	1.34	39.7
CdSe/2-ACA	0.41	12.5	39.9

7.14 Characterization of surface chemistry of Si:C18 and Si:9EA

7.14.1 Proton NMR of Si:C18 and Si:9EA

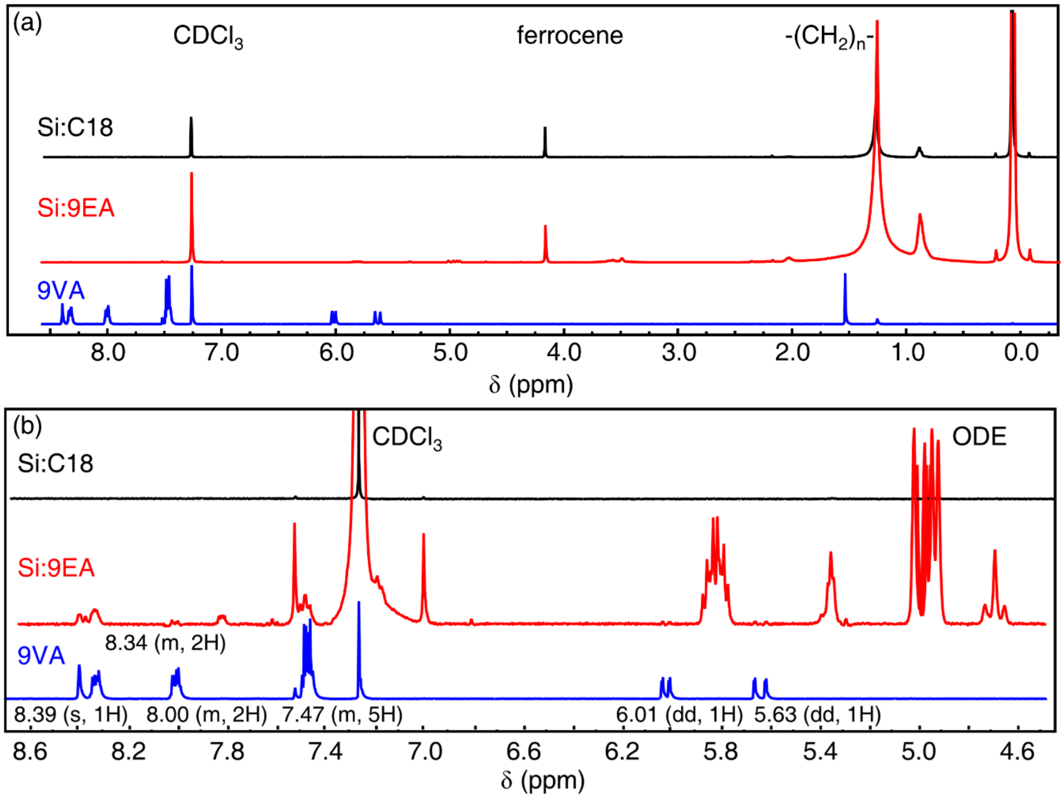

Fig. 7.11 (a) Proton NMR spectra of Si:C18 and Si:9EA ($\langle N_{9EA} \rangle = 2.2 \pm 0.3$) and 9VA in $CDCl_3$ with ferrocene as a standard. (b) Expansion of the aromatic region.

^{1}H NMR spectra of Si:C18 and Si:9EA ($\langle \mathrm{N_{9EA}} \rangle = 2.2 \pm 0.3$) are shown in Fig. 7.11. All spectra were acquired overnight. Toluene and methanol were evaporated under high vacuum and the entire sample dissolved in $CDCl_3$. Ferrocene was added as an internal standard. Comparing NMR spectra of Si:C18 and Si:9EA, the broad peaks at 1.25 ppm and 0.82 ppm are assigned to ODE's $-(CH_2)_n-$ aliphatic protons and terminal $-CH_3$, respectively. For 9VA, the singlet at 8.39 ppm corresponds to the proton at its 10 position and the doublet of doublets at 5.61 ppm and 6.03 ppm correspond to 9VA's vinyl protons. NMR spectra of Si:9VA show near complete elimination of signal from these vinyl protons while still showing aromatic proton signal, indicating nearly all anthracene in solution binds to Si.

7.14.2 Attenuated Total Reflectance Infrared Spectra of Si:C18 & Si:9EA

Attenuation total reflection infrared (ATR-IR) spectroscopy confirms the assigned structures of Si:C18 and Si:9EA. Fig. 7.11 displays ATR-IR spectra for as-synthesized Si NCs powder (magenta), Si:C18 (black), Si:9EA (red) and the pure 9VA precursor used for hydrosilylation (blue). The as-prepared Si NCs exhibit three distinct absorptive features within the *SiH_n envelope corresponding to the Si–H stretching modes from silicon trihydride SiH_3 (ν = 2138 cm^{-1}), dihydride SiH_2 (ν = 2108 cm^{-1}) and monohydride SiH (ν = 2082 cm^{-1}) surface terminations. ATR-IR signatures of ligand-functionalization include a loss of the SiH_n absorption peak, appearance of -CH_2- and -CH_3 absorption peaks at δ = 2853, 2922 and 2956 cm^{-1}; and Si-C stretches at 792 cm^{-1} and 1260 cm^{-1}. Comparing IR spectra of 9VA and Si:9EA, the diagnostic peaks in the range of 1625 - 1633 cm^{-1} correspond to C=C aromatic ring stretching and indicate the presence of surface-bound anthracene. These peaks are not very intense due to the low concentration of 9EA on the NC surface. We note there are signatures of oxidation for the functionalized Si NCs even when stored in a nitrogen glovebox with water < 0.5 ppm and oxygen < 0.2 ppm. This is reflected in the decrease of Si-H_n silicon hydride signals and the growth of peaks at 1080 cm^{-1} and 1009 cm^{-1}, which are assigned to Si-O stretches. These features of oxidation are also in other reports of thermal hydrosilyation and do not appear to be a severe barrier to triplet energy transfer.[3]

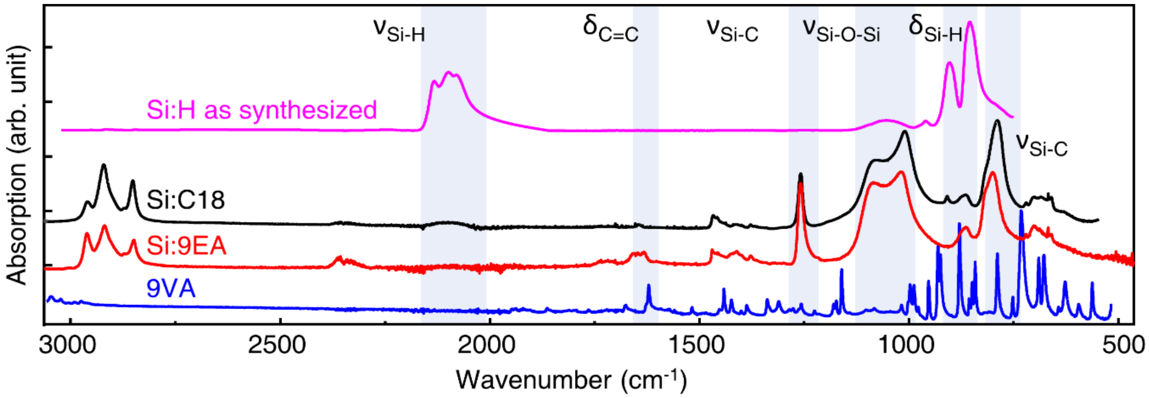

Fig. 7.12 Attenuated total reflectance infrared spectra (ATR-IR) of hydrogen-terminated, as synthesized Si nanocrystals (NCs, magenta), Si NCs capped with only octadecane (Si:C18, black), Si NCs functionalized with both octadecane and 9VA (Si:9EA, red) and pure 9VA (blue).

7.14.3 Transmission Electron Microscopy and X-Ray Diffraction Patterns of Si:C18

Transmission electron microscopy (TEM) and x-ray diffraction (XRD) were used to characterize the average size and degree of crystallinity of Si:C18 particles prior to 9EA functionalization. Fig. 7.13a displays a representative TEM image of a Si:C18 particle showing it consists of a single crystalline domain. The measured spacing between the lattice fringes is 0.314 nm, consistent with the 111 planes of silicon. XRD patterns measured for Si:C18 particles (Fig. 7.13b) show diffraction peaks consistent with Si's known diamond lattice. Scherrer analysis applied to the 111 peak at $2\theta = 28.4^{\circ}$ yields an average crystallite size of 3 nm.

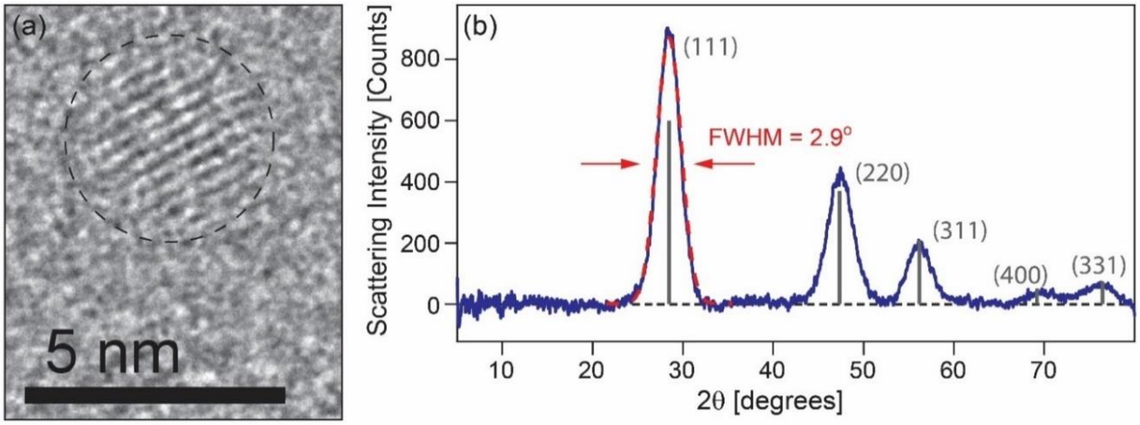

Fig. 7.13 (a) Representative TEM image of a Si:C18 NC. Uniform lattice fringes can be seen confirming the particle consists of a single crystalline domain. (b) XRD pattern of Si:C18 NCs. Stem peaks (grey) correspond to the expected Si powder pattern based on Si's diamond lattice.

7.15 Transient absorption for silicon nanocrystals

7.15.1 Triplet Sensitization of 9-methlyanthracene

Following photoexcitation of Si, TA spectra of Si:9EA NCs show growth of a sharp photoinduced absorption band peaked at 433 nm and a similarly sharp photobleach at 390 nm whose rate of growth tracks the decay of Si photoinduced absorption. These features are similar to bands previously assigned to the lowest excited triplet state (T_1) of anthracene derivatives,[6–8] suggesting their appearance signals energy transfer from excited Si NCs to 9EA bound to their surface. To test this assignment, we measured the TA spectrum of 9-methylanthracene (9MA) in toluene via a triplet sensitization experiment. 9MA was chosen for this comparison rather than the 9-vinylanthracene (9VA) precursor we covalently attach to Si NCs as the pendant vinyl group of 9VA is converted from sp^2 to sp^3 carbons during attachment.

To determine 9MA's triplet spectrum, a mixture of 9MA and platinum octaethylporphyrin (PtOEP) in toluene was prepared. Photoexcitation of PtOEP's Q-band at 532 nm places it into its lowest excited singlet state, which rapidly intersystem crosses to its triplet state on a ~165 fs timescale.[9] As PtOEP possess a triplet energy of 1.9 eV[10] that is higher than that of 9MA (~1.8 eV), diffusional collisions of photoexcited PtOEP with 9MA molecules in their ground state can result in triplet energy transfer from PtOEP to 9MA.

Fig. 7.14 a plots TA spectra of the PtOEP:9MA solution following PtOEP photoexcitation at 532 nm. At short time delays (1 ns), two prominent photobleaching transitions can be seen at 384 nm and 536 nm that are attributable to PtOEP's Soret and Q-band respectively. The small photobleach at 502 nm represents a vibrational side band of PtOEP's Q-band. Between these features, a broad photoinduced absorption peaked at 422 nm appears that matches well prior assignments of PtOEP's T_1 state.[9] Over time, these features from PtOEP's T_1 state decay, leaving behind a sharp resonance peaked at 431 nm along with a shoulder extending to higher energy. As these features overlap with spectral signatures from PtOEP's T_1 state, a singular value decomposition (SVD) algorithm was used to separately identify the spectrum that grows from the decay of PtOEP's T_1 state. The two primary components recovered from this analysis are plotted in Fig. 7.14b. The first component matches our assignment of PtOEP's T_1 state while the second we assign to the 9MA T_1 state. This assignment is based on the fact that the 9MA T_1 state is the only energetically accessible photoexcited state that can be produced by PtOEP's T_1 state in our mixture, the bleaching transition at 384 nm falls very close to the lowest energy peak in 9MA's ground state absorption spectrum (389 nm), signaling this state arises from excited 9MA molecules, and the prominent photoinduced absorption bands at 410 and 431 nm agree well with prior assignments of photoinduced T_1 absorption bands of many anthracene derivatives.[6–8] Importantly, we find features in 9MA's T_1 TA spectrum well match those appearing in TA spectra of Si:9EA following the decay of Si NC photoinduced absorption

(Fig. 3.3b, chapter 3), leading us to conclude photoexcitation of Si NCs drives spin-triplet energy transfer to anthracene ligands at their surface.

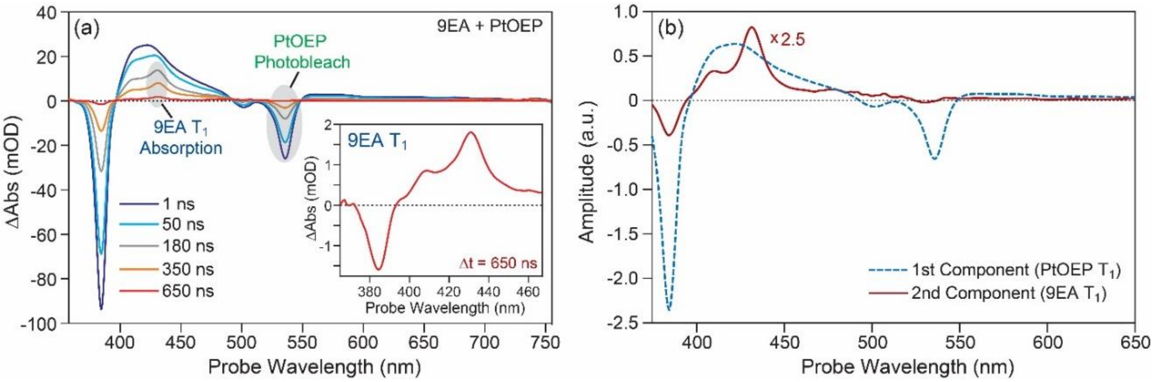

Fig. 7.14 (a) TA spectra of a PtOEP:9MA mixture following PtOEP excitation at 532 nm. As spectral signatures from PtOEP's T_1 state decay, new features appear between ~375 – 450 nm that we assign to 9EA's T_1 state (inset). (b) SVD analysis of TA spectra of PtOEP:9MA recovers two primary components, which we assign to the T_1 states of PtOEP (blue dashed) and 9MA (red).

7.15.2 Isolation of 9EA Triplet Growth Kinetics from TA Spectra

TA spectra of Si:9EA show 9EA triplet production occurs with a rate that matches the decay of signal from the photoexcited Si NC core (Fig. 3.3b & Fig. 3.3d, chapter 3), indicating 9EA triplet excitons form as a result of energy transfer from Si. However, extracting a rate for this process is complicated by the fact that spectral signatures of 9EA triplet excitons overlap with a broad photoinduced absorption band from photoexcited Si NCs. Thus, prior to fitting kinetic data signaling production of 9EA triplet excitons, we need to remove overlapping contributions to 9EA spectral signals from the photoinduced absorption background stemming from excited Si NCs. Fortunately, this can be done by examining the decay of Si:9EA TA spectra in a spectral region where 9EA triplet excitons give rise to zero signal as this region solely reports on the dynamics of the photoexcited Si NC core. Thus, to remove contributions to the TA spectrum of Si:9EA from photoexcited Si, we recorded a TA spectrum of Si:C18, which features no 9EA molecules, and normalized the spectrum recorded for Si:C18 at each TA time delay to that of Si:9EA within the spectral range of 550 – 625 nm where triplet sensitization experiments show 9EA triplet excitons produce no spectral signal (Fig. 7.15b). Subtraction of this normalized signal from that of Si:9EA produces a TA spectrum showing dynamics that stem from 9EA alone.

Fig. 7.15shows TA spectra of Si:9EA before and after this background subtraction procedure is performed. Prior to subtraction, we find dynamics measured at a probe wavelength of 433 nm, the spectral peak of the 9EA T_1 induced absorption signal, display complicated kinetics, immediately rising from t = 0 before showing a slight decay followed by a slower rise over ~20 ns before decaying again on a ~100 ns timescale (Fig. 7.15c, red). Of these various kinetic processes, only the ~20 ns rise stems from 9EA while the rest are tied to photoexcited Si NCs and their subsequent internal dynamics (see Fig. 7.16). Similarly, complicated kinetics are seen at a probe wavelength of 390 nm, which initially shows a strong positive signal rather than the expected negative signal due to photobleaching of 9EA's ground state (Fig. 7.17c, blue). After subtraction of the Si NC signal, we see that most of these complicated kinetics disappear, revealing a clear rise of photoinduced absorption from 9EA's T_1 state at 433 nm that is mirrored by the growth of a negative signal at 390 nm tied to photobleaching of 9EA's ground state (Fig. 7.17d). Such coordinated growth of T_1 induced absorption and ground state photobleaching signal that energy transfer from Si to 9EA directly populates its T_1 state.

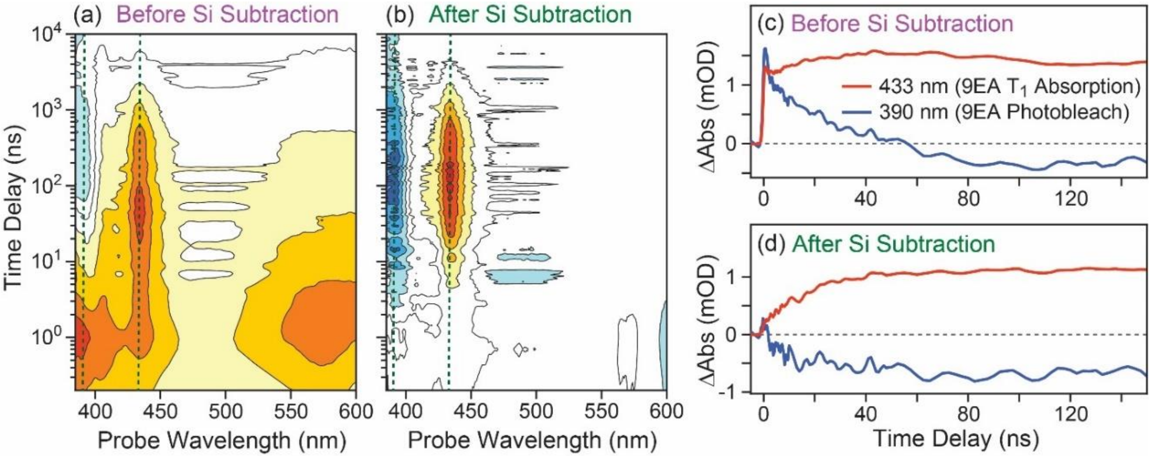

Fig. 7.15 TA spectra of Si:9EA before (a) and after (b) subtraction of photoinduced absorption signal from the photoexcited Si NC core. Positive photoinduced absorption signals are shown as red/orange contours while blue contours signal negative photobleaching signals. (c & d) Spectral slices taken at 390 and 433 nm before (c) and after (d) Si NC photoinduced absorption subtraction. The positions where these slices are taken are highlighted as dashed green lines in panels (a) & (b).

7.15.3 Kinetic Model for Silicon-to-9EA Spin-triplet Exciton Transfer

TA spectra in Fig. 3.3of the main text indicate photoexcitation of Si:9EA results in triplet exciton transfer from excited Si NCs to 9EA molecules tethered to their surfaces. However, our data also shows this energy transfer process is not 100% efficient as (1) photoinduced absorption signal from Si NCs persists following relaxation of 9EA triplet excitons in TA measurements and (2) photon upconversion experiments show persistent red Si NC emission even in the presence of 9,9-diphenylanthracene triplet energy acceptors. To explain the origin of these two observations and obtain a quantitative estimation of the Si-to-9EA triplet energy transfer yield, we have constructed a kinetic model that explicitly accounts for the size distribution (and hence variations in exciton energy) of Si NCs within our Si:9EA ensemble as well as heterogeneity in the number of 9EA molecules bound to NCs within this ensemble. Fig. 3.4a of chapter 3 provides a graphical overview of this model, which is described by the following kinetic equations:

$$\frac{d[Si]}{dt} = -k_{Si}[Si] - k_{TET}(E_a)N_{9EA}[Si] \qquad \text{eq. 7.13}$$

$$\frac{d[T_{9EA}]}{dt} = k_{TET}(E_a)N_{9EA}[Si] - k_{9EA}[T_{9EA}] \qquad \text{eq. 7.14}$$

Here, [Si] and $[T_{9EA}]$ respectively represent the concentration of photoexcited Si NCs and 9EA spin-triplet excitons produced by energy transfer from Si. The rate of energy transfer from Si to 9EA is described by $k_{TET}(E_a)$, which is scaled by an Arrhenius activation energy depending on the difference in the exciton energy of a Si NC, E_{Si}, and the triplet energy of 9EA, E_T:

$$k_{TET}(E_a) = k_{TET}^{0}\exp\left(-E_a/k_bT\right) \text{ where } E_a = E_T - E_{Si} \qquad \text{eq. 7.15}$$

We assume the rate of triplet energy transfer from Si to 9EA is additionally scaled by the number of available 9EA triplet acceptors bound to a Si NC, N_{9EA}. Relaxation rates for the return of photoexcited Si NCs and 9EA triplet excitons to the ground state are described by k_{Si} and k_{9EA} respectively.

To fit the growth and decay of photoexcited Si NC and 9EA triplet populations, we assume our Si:9EA ensemble contains a distribution of Si NCs with different characteristic exciton energies whose distribution is described by the steady-state emission spectrum of the Si:C18 sample. We believe this is a reasonable assumption as the dynamics of triplet energy transfer we observe occur on the nanosecond timescale, which suggests triplet transfer takes place after any internal relaxation processes within photoexcited Si NCs occurs that result in energy relaxation to low-energy emissive states. We also assume the probability that a Si NC binds a specific number of 9EA molecules is given by a Poisson distribution whose average value, $\langle N_{9EA}\rangle$, is equal to 2 as estimated from absorption spectra of Si:9EA (Section 3B above).

To describe k_{Si}, we parameterize this term based on the decay observed for Si:C18 NCs that feature no triplet-accepting 9EA molecules. In accordance with prior reports of Si NC photoexcited dynamics,[11] we find Si:C18 NCs undergo relaxation over multiple timescales, that stem from a few nanoseconds to hundreds of microseconds (Fig. 7.16, blue). Such complex decay can be reproduced by a model that assumes different NCs within the Si:C18 ensemble contain differing numbers of traps or defects that facilitate photoexcited carrier decay:

$$k_{Si} = k_{Si}^{0} + \sum_{m} N_m k_m \qquad \text{eq. 7.16}$$

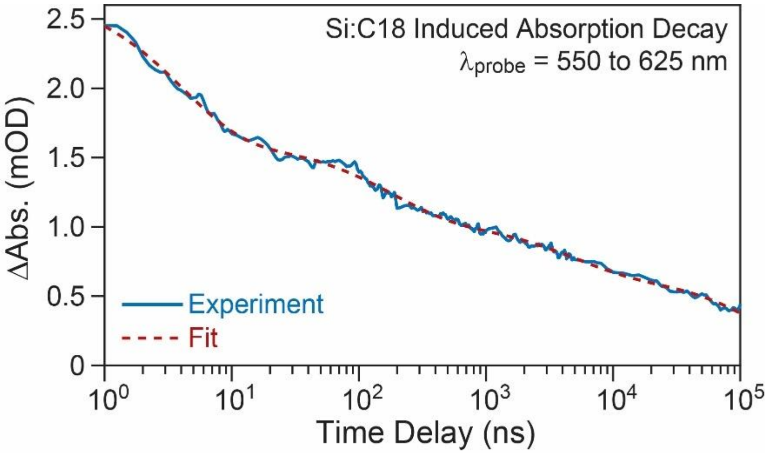

Fig. 7.16 Relaxation dynamics of photoinduced absorption of Si:C18 NCs averaged over probe wavelengths from 550 to 625 nm along with a fit described by eq. 7.16. Full spectral dynamics appear in Fig. 3.3a of the main text and recovered fitting parameters are described in Table 7.10.

Here, the summation in eq. 7.16 is performed over the different types of traps present within the NC ensemble, with N_m being the number of traps of a particular type within a given NC, k_m being the carrier relaxation rate facilitated by that type of trap, and k_{Si}^{0} being the intrinsic relaxation rate of a NC in the absence of carrier traps. This model can be solved analytically, assuming particle traps are spread according to a Poisson distribution among NCs within the ensemble:[12]

$$[\mathrm{Si}] = \exp(-k_{\mathrm{Si}}^{0} t + \textstyle\sum_m \langle N_m \rangle (\exp(-k_m t) - 1)) \qquad \text{eq. 7.17}$$

We find inclusion of at least three types of traps with different characteristic relaxation rates is needed to fully reproduce the photoexcited population decay of Si:C18 (Fig. 7.16, red dashed). While this suggests the NCs within our ensemble contain a variety of structures that lead to heterogeneous relaxation kinetics, at present we leave the interpretation of the underlying origin of these relaxation kinetics to further work. Rather, we simply use the relaxation timescales recovered from fitting data in Fig. 7.16 as inputs into our model for describing Si-to-9EA triplet energy transfer.

Fig. 3.4 of the main text compares the fitting results of our model with dynamics measured following photoexcitation of our Si:9EA ensemble for the growth and decay of 9EA triplet excitons and relaxation of Si NCs. The model reproduces the behavior seen in the data exceptionally well over 5 decades in time. Kinetic parameters extracted from the fit are summarized in Table 7.10. From this data we extract a triplet energy transfer timescale, $1/k_{\mathrm{TET}}^{0}$, of 15.2 ns. We note that repeated measurements of Si:9EA samples yielded a distribution of timescales for this value, ranging from 15.2 ns to 46.1 ns, with an average value of 25.8 ns. However, we have chosen to highlight the data in Fig. 3.4 rather than other recorded datasets as it is of the highest signal-to-noise quality of our measurements and no signatures of sample photooxidation were observed over the course of its measurement.

Interestingly, we note that to fully fit the [Si] relaxation dynamics of the Si:9EA ensemble, we need to slightly adjust the values for the average number of two of the Si NC trap sites, $\langle N_1 \rangle$ and $\langle N_3 \rangle$, that facilitate carrier decay relative to those used to fit the relaxation of the Si:C18 sample

(Table 7.10). Such changes may reflect changes in the surface chemistry of Si NCs linked to 9EA attachment. However, we note changes in the values of $\langle N_1 \rangle$ and $\langle N_3 \rangle$ used to optimize the fit to the Si:9EA data are small and locking these values to those recovered from the Si:C18 fit negligibly impact our fit to the rise and decay kinetics we measure for 9EA triplet excitons, $[T_{9EA}]$. Hence, we find adjusting these values to only have a minor impact on the value of k^0_{TET} recovered from our model.

Table 7.10 Parameters used to fit TA spectra of Si:9EA and Si:C18. Constraints imposed on each parameter during fitting are listed in the column on the right. $\langle N_1 \rangle$, $\langle N_2 \rangle$, and $\langle N_3 \rangle$ are the average number of different types of carrier traps used to fit the decay of Si:C18 and k_1, k_2, and k_3 their associated decay constants. Only 4 free parameters were needed to fit the dynamics of Si:9EA, and constraining two of these parameters, $\langle N_1 \rangle$ and $\langle N_3 \rangle$, to match values recovered from fitting Si:C18 makes only a marginal reduction in the overall quality of the fit to the Si:9EA data

	Si:9EA	Si:C18	Method of Parameter Determination
$\langle N_{9EA} \rangle$	2	NA	Estimated from absorption spectra of Si:9EA
$1/k^0_{TET}$	15.2 ns	NA	Floated to fit Si:9EA dynamics
$1/k_{9EA}$	1.16 μs	NA	Floated to fit Si:9EA dynamics
$1/k^0_{Si}$	180 μs	180 μs	Constrained when fitting Si:9EA based on Si:C18 decay
$\langle N_1 \rangle$	0.092	0.51	Floated to fit Si:9EA and Si:C18 individually
$1/k_1$	4.95 ns	4.95 ns	Constrained when fitting Si:9EA based on Si:C18 decay
$\langle N_2 \rangle$	0.43	0.43	Constrained when fitting Si:9EA based on Si:C18 decay
$1/k_2$	213 ns	213 ns	Constrained when fitting Si:9EA based on Si:C18 decay
$\langle N_3 \rangle$	0.86	0.47	Floated to fit Si:9EA and Si:C18 individually
$1/k_3$	5.59 μs	5.59 μs	Constrained when fitting Si:9EA based on Si:C18 decay
E_T	1.805 eV	NA	Estimated from References 13 and 14

7.15.4 Dependence of Triplet Energy Transfer Rate on $\langle N_{9EA} \rangle$

We note our extracted timescale of 15.2 ns for silicon-to-9EA energy transfer is dependent on

$\langle \mathrm{N}_{9\mathrm{EA}} \rangle$ and hence our methodology for estimating the extinction cross-section of both 9EA molecules and the Si NCs to which they bind. In estimating the latter, we have used extinction values published by Carroll et al.[3] for 6.5 nm diameter Si NCs and assumed a cubic dependence of these values on NC diameter to estimate extinction coefficients for the 3.1 nm diameter NCs we investigate here. However, work by Lee et al.[15] has suggested that Si NC extinction within the spectral range we use to compute NC concentration decreases slower with shrinking NC size than a cubic dependence on NC radius would predict. Likewise, electronic coupling between Si and 9EA may lower the molar extinction of 9EA relative to that of 9MA, whose extinction coefficient we use to estimate the concentration of 9EA. The former would lead us to overestimate the number of Si NCs in our sample solutions, while the latter would cause us to underestimate of the concentration of 9EA molecules. The end result in either case would be an underestimation of $\langle \mathrm{N}_{9\mathrm{EA}} \rangle$, which would lead our model to overestimate $\mathrm{k}_{\mathrm{TET}}^{0}$.

To investigate the extent to which such an underestimation impacts our conclusions, we have fit our data wherein we have constrained $\langle \mathrm{N}_{9\mathrm{EA}} \rangle$ to be equal to 10.8, a value we estimate using extinction cross-sections reported for Si NCs by Lee et. al.[15] This value assumes that the molar extinction coefficient of 9EA molecules bound to Si NCs is not substantially changed from that of 9MA, but we estimate errors tied to this assumption to be smaller than the variance in Si NC cross-section we compute using values from Carroll et al.[3] and Lee et. al.[15]

Fig. 7.17a plots results of this fit to our TA data alongside those shown in the main text for which $\langle \mathrm{N}_{9\mathrm{EA}} \rangle$ was constrained to be 2. We find that the model with $\langle \mathrm{N}_{9\mathrm{EA}} \rangle = 10.8$ produces a fit that is nearly indistinguishable from that with $\langle \mathrm{N}_{9\mathrm{EA}} \rangle = 2$, with values of $\langle \mathrm{N}_1 \rangle$, $\langle \mathrm{N}_3 \rangle$, and $1/\mathrm{k}_{9\mathrm{EA}}$ that are only moderately adjusted from those reported in Table 7.10 (0.021, 0.43, and 1.14 □s respectively). The largest change in the parameters assocaited with the $\langle \mathrm{N}_{9\mathrm{EA}} \rangle = 10.8$

fit is the value of $1/\mathrm{k}^{0}_{\mathrm{TET}}$, which increases from 15.2 ns to 74.8 ns, a slowdown in the rate of triplet energy transfer of 4.9× that roughly mirrors the 5.4× increase in $\langle \mathrm{N}_{9\mathrm{EA}} \rangle$ presupposed by this fit.

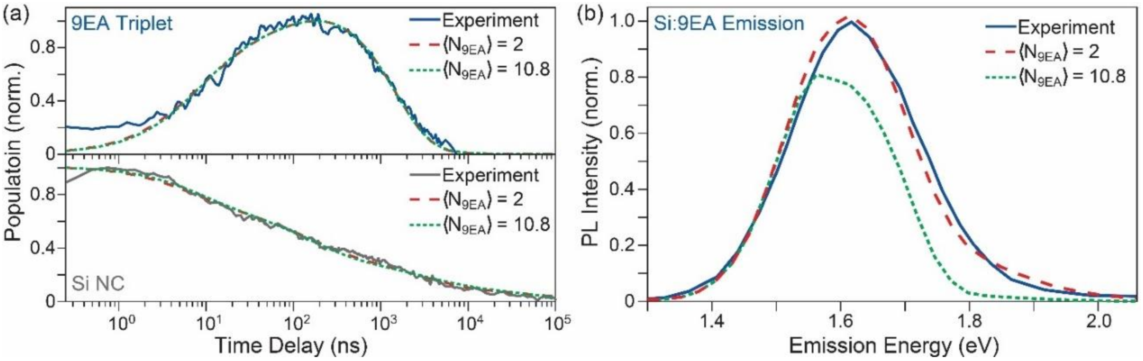

Fig. 7.17. (a) Fits to time-dependent populations of 9EA triplet excitons (top) and excited Si NCs (bottom) using our kinetic model with $\langle N_{9EA} \rangle$ = 2 (red dashed) and $\langle N_{9EA} \rangle$ = 10.8 (green dotted). (b) Comparison of experimental Si:9EA emission spectra (blue) and that computed from our kinetic model with $\langle N_{9EA} \rangle$ = 2 (red dashed) and $\langle N_{9EA} \rangle$ = 10.8 (green dotted).

However, while we find our model can well fit our TA data when $\langle \mathrm{N}_{9\mathrm{EA}} \rangle$ is held at 10.8, Fig. 7.17b shows the model does a poorer job in reporducing the PL emission amplitude and peak position. This result makes sense as the larger number of molecules bound to Si NCs presupposed by the model eliminates the possiblity of having NCs in our sample that lack 9EA molecules bound to their surface according to Poission statistics. In our fit highlighted in the main text with $\langle \mathrm{N}_{9\mathrm{EA}} \rangle$ = 2, NCs lacking any bound 9EA account for 13.5% of the NC population and provide a natural explanation for residual Si NC emission observed at energies above the 9EA triplet energy (1.8 eV).

We note that binding of 9EA to Si could result in a change of its triplet energy, which would provide an alternative explanation for the high energy emission tail. However, given that bound molecules experience a decrease in their S_1 state energy relative to 9MA, an increase in their triplet energy seems unlikely as it is built from the same spatial orbital occupancy. Likewise, if we assume some 9EA molecules that bind to Si NCs are incapable of accepting triplets, perhaps due to a preference of triplet energy transfer occurring to molecules bound to specific Si NC surface facets, our model could better reproduce the emission amplitude and center position with a larger value of $\langle \mathrm{N_{9EA}} \rangle$. However, such heterogeneous triplet molecular binding is difficult to characterize and to our knowledge distributed energy transfer kinetics stemming from such binding have not been observed in any covalent NC:triplet acceptor systems.

As increasing $\langle \mathrm{N_{9EA}} \rangle$ by 5.4× produces a poorer overall reproduction of our PL data, we have chosen to highlight our fit with $\langle \mathrm{N_{9EA}} \rangle = 2$ in the main text. We believe this value is a conservative one as it likely underestimates $\langle \mathrm{N_{9EA}} \rangle$, but ultimately has little impact on the qualitative conclusions we draw from our model. We observe clear evidence of Silicon-to-9EA triplet energy transfer over tens of nanoseconds and this conclusion is unchanged by varying $\langle \mathrm{N_{9EA}} \rangle$ within a reasonable window based on published extinction values for Si NCs and 9MA. With improved analytical methods for determining $\langle \mathrm{N_{9EA}} \rangle$, we can refine estimates of $1/\mathrm{k_{TET}^{0}}$ in future work.

7.16 Characterization of PbS QD with short ligands

7.16.1 Attenuated total reflection infrared (ATR-IR) spectroscopy of PbS@ligand

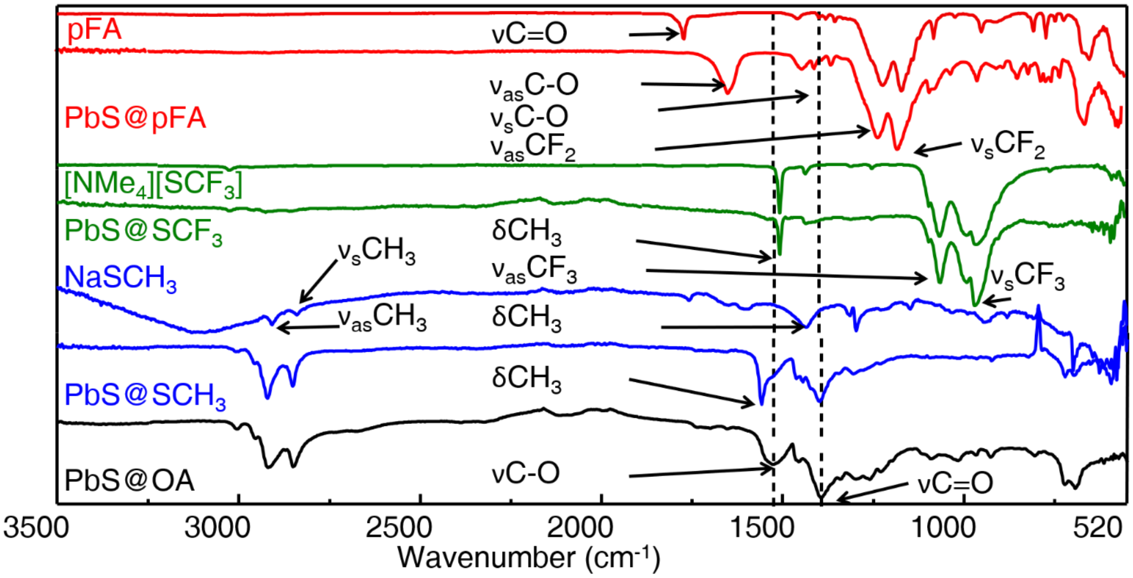

Fig.7.18 Infrared spectra of PbS@ligand complexes after unbound ligands were removed by centrifugation and cleaning. The two dashed lines are vibrations of C-O and C=O respectively of OA when bound on the QD surface.

Table 7.11. The vibrational frequencies of characteristic bonds for the free (red) and bound (blue) ligands on the surface of the PbS QD (blue) from the spectra in Fig.7.18.

Mode	ν /cm^{-1}	Mode	ν /cm^{-1}		Mode	ν /cm^{-1}		Mode	ν /cm^{-1}	
	PbS@OA		PbS@pFA	pFA		PbS@SCF$_3$	[NMe$_4$][SCF$_3$]		PbS@SCH$_3$	NaSCH$_3$
ν(C-H)	2918	ν(C=O)	-	1754	δ(C-H)	1488	1488	δ(C-H)	2912	2908
		ν$_{as}$(C-O)	1623	-						
ν(C-H)	2948	ν$_s$(C-O)	1462	1438	ν$_s$ (CF$_3$)	1045	1045	ν$_{as}$(CH$_3$)	1445	1435
ν(C-O)	1523	ν$_s$(CF$_2$)	1209	1200	ν$_{as}$ (CF$_3$)	966	955	ν(CH$_3$)	1307	1298
δ(C-H)	1394	ν$_{as}$(CF$_2$)	1151	1149	ν$_{as}$ (CF$_3$)	955	941	δ(C-S)	-	698[34]

7.16.2 TEM characterization of PbS@ligand complexes

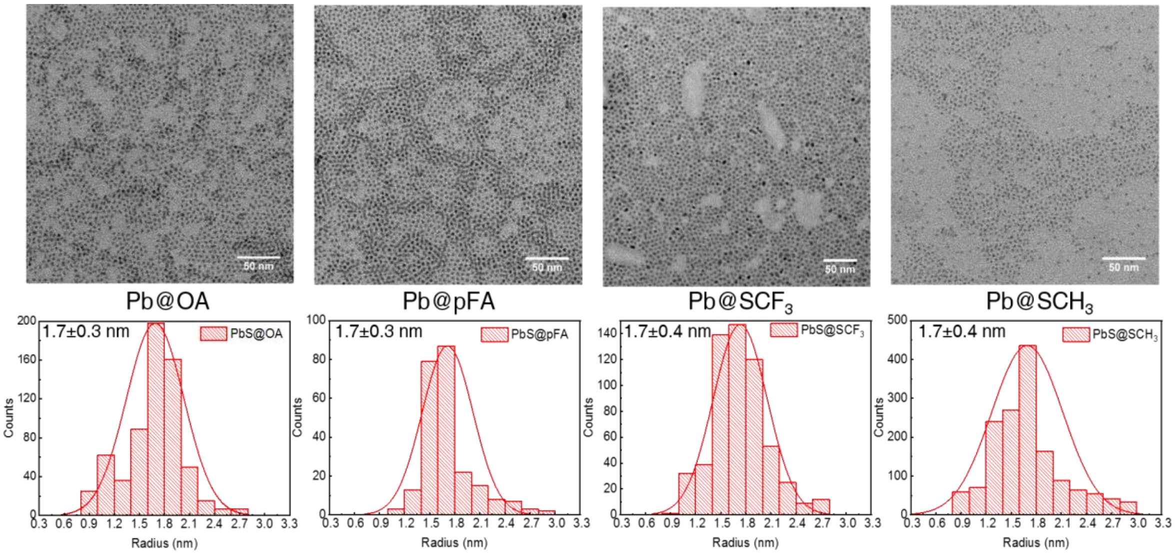

Fig. 7.19. TEM images of PbS@ligand complexes. From left to right: PbS@OA, PbS@pFA, PbS@SCF$_3$ and PbS@SCH$_3$ QDs, respectively. The corresponding size distributions are obtained from analysis of the TEM images with Image J software. The histogram plots the average radius of the QDs with standard errors.

7.16.3 charge transfer: analysis of steady-state PL quenching using the Stern-Volmer equation

The Stern-Volmer quenching constants are obtained from Fig. 7.4. The amplitude averaged lifetime has been applied to obtain the Stern-Volmer dynamic quenching constant K_D. This is because using the intensity-weighted lifetimes, or the ratio of the intensity-weighted lifetime without BQ, $\bar{\tau}_0$, to the intensity weighted lifetime with BQ, $\bar{\tau}$, or $\bar{\tau}_0/\bar{\tau}$ vs. [BQ] is not linear. This is in agreement with Sillen and Engelborghs's theoretical discussion that in most cases, the amplitude averaged lifetime is preferred except when calculating the average collisional quenching constant.[35]

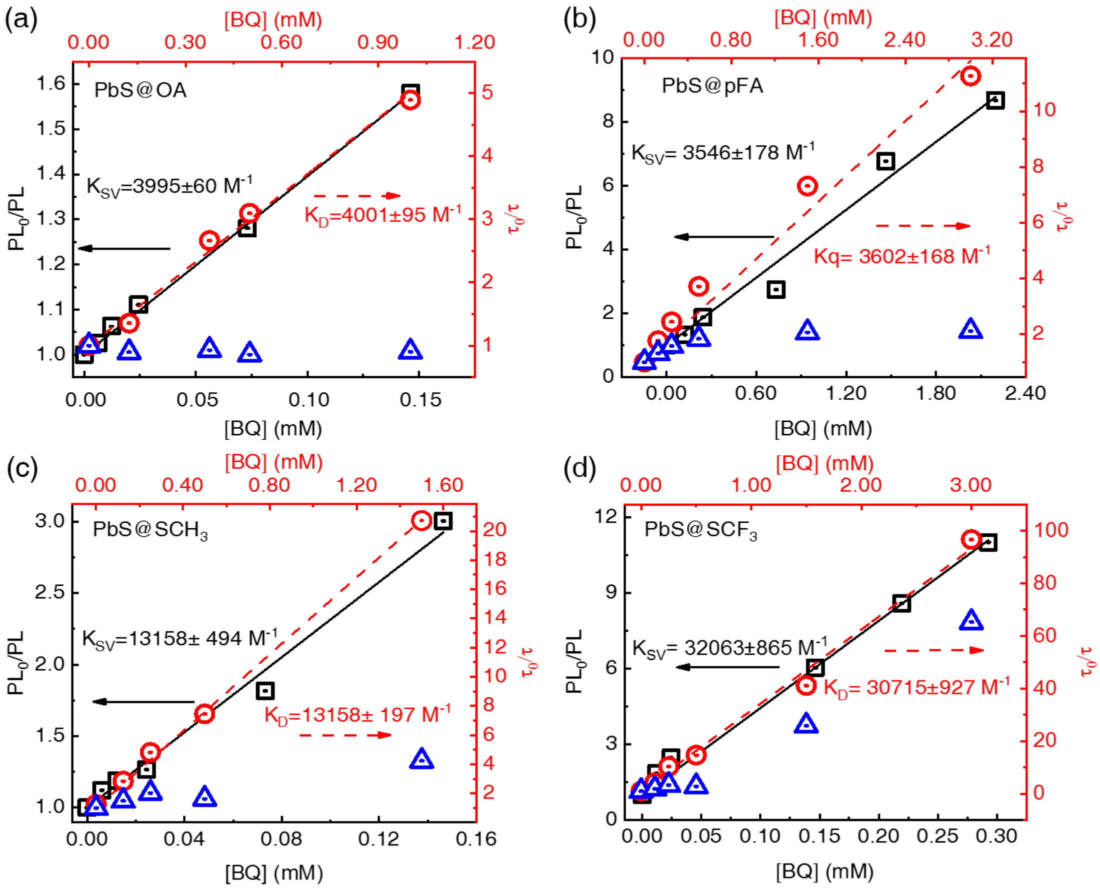

Fig. 7.20 PL_0/PL vs. [BQ], ô$_0$/ô (including $< \bar{\tau}_0 >/< \bar{\tau} >$and $\bar{\tau}_0/\bar{\tau}$ vs. [BQ] for PbS@OA -(a), PbS@pFA-(b), $PbS@SCF_3$ -(c) and $PbS@SCH_3$ -(d). PL_0 and ô$_0$ (including $< \bar{\tau}_0 >$ and $\bar{\tau}_0$) are the steady-state PL and intrinsic lifetimes (including amplitude and intensity average) of PbS@pFA in the absence of BQ, while PL and ô (including $< \bar{\tau} >$ and $\bar{\tau}$) are the corresponding values in the presence of BQ. K_D and K_{SV} are the Stern-Volmer quenching constants being obtained from a linear fit to the changes in QD amplitude average lifetime and steady-state PL respectively. Black square is PL_0/PL. Red circle is $< \bar{\tau}_0 >/< \bar{\tau} >$and violet triangle shows $\bar{\tau}_0/\bar{\tau}$.

7.16.4 Ultraviolet Photoelectron Spectroscopy (UPS)

Sample fabrication: UPS data was obtained with PbS@ligand complexes in thin film. The films were fabricated, transferred and measured in a nitrogen-filled glovebox without being exposed to the atmosphere. Oleic acid functionalized PbS NC (λ_{abs}=1058 nm) were synthesized according to the hot injection method.[36] Thin films of PbS QDs with complete ligand exchange were fabricated in two steps

(1) Spin-coating (12000 rpm) partial ligand exchanged solution onto (3-Mercaptopropyl) trimethoxysilane (3MPT) treated glass (for absorption measurement) or onto indium tin oxide coated glass (for UPS measurement) (see conditions in colloidal ligand exchange section in this SI)

(2) Dip-coating the partially ligand exchanged thin film in a 1 mg/ml ligand solution for 5 minutes, then spin-coating away any remaining solution and cleaning three times with good solvent for ligand.

Steps (1) and (2) were repeated if the desired thin film thickness (30 nm) is not achieved. As shown in Fig. 7.2 a/b, UV-Vis-NIR electronic absorption measurements and ATR-IR of the resulting thin film verified quantum confinement was preserved and complete ligand exchange respectively. In Fig. 7.2b, vibrational peaks at 2700-2900 cm^{-1}, corresponding to -CH_2, -CH_3 stretching, vanished after complete ligand exchange.

Table 7.12 Parameters of UPS samples of PbS@ligand thin film before and after fully ligand exchange.

Ligand	CB/eV	E_{gap}/eV	λ_{max}/nm	Work function /eV	VB onset/eV	Ionization energy/eV
SCH_3	-2.95	1.14	1090	-4.09	0.35	4.44
SCF_3	-3.02	1.18	1050	-4.20	0.53	4.73
OA	-3.37	1.16	1073	-4.53	0.64	5.17
pFA	-4.27	1.18	1052	-5.45	0.75	6.20

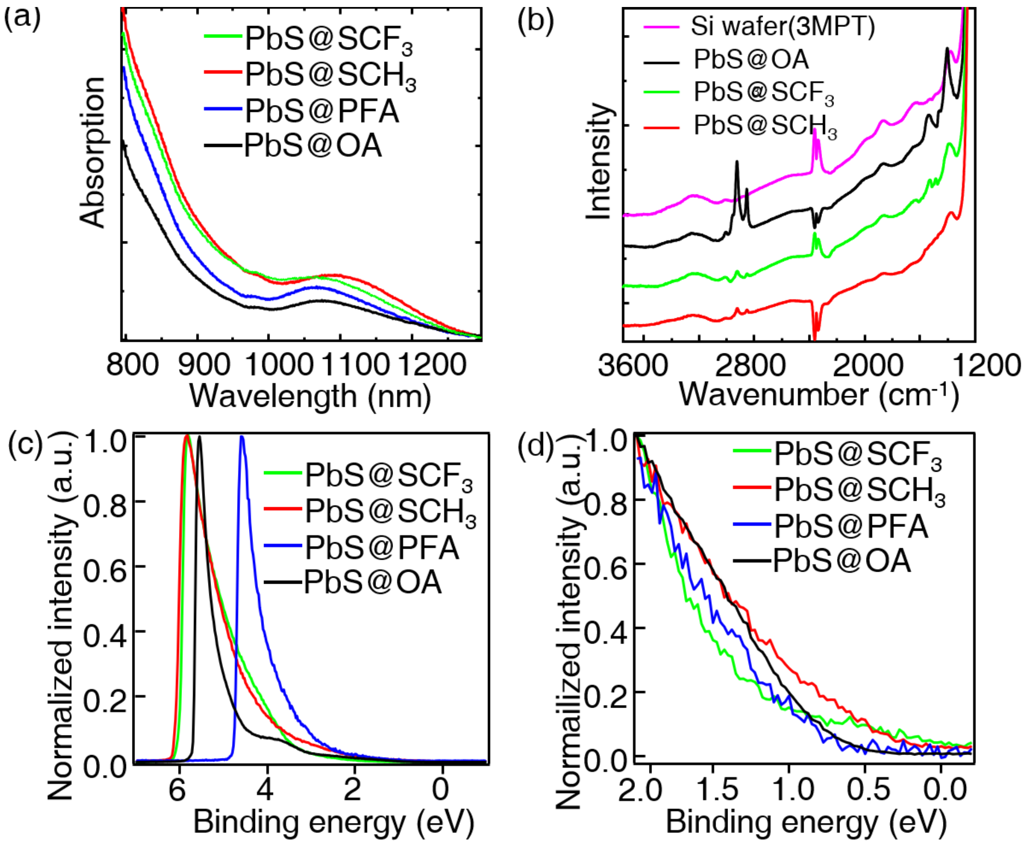

Fig. 7.21 (a) Absorption spectra of PbS@ligand after complete ligand exchange on (3-Mercaptopropyl) trimethoxysilane treated glass. (b) ATR-IR of PbS@ligand after complete ligand exchange on (3-Mercaptopropyl) trimethoxysilane treated silicon wafers. UPS spectra measured with a 10.2 eV H Lyman-á lamp of PbS@ligand thin films on ITO coated glass. The secondary electron cut-off regions are shown in (c) and the valence band onset in (d).

7.17 Cyclic voltammetry (CV) measurements of the highest occupied molecular orbital (HOMO) and lowest unoccupied molecular orbital (LUMO) of NCs and ligands

7.17.1 Measurement of molecular HOMO and LUMO via cyclic voltammetry (CV)

Electrochemical measurements were conducted on a Gamry interface 1000 electrochemical analyzer with a three-electrode system under argon in an anhydrous dichloromethane (DCM) solution of tetra-n-butylammonium hexafluorophosphate (0.1 M). A glassy carbon electrode was used as a working electrode, a platinum-wire was used as the counter electrode, and an

Ag/Ag$^+$ (0.01 M $AgNO_3$ in DCM) electrode was used as the reference electrode. The sample was dissolved in DCM. The CV curves were calibrated with the ferrocene/ferrocenium (Fc/Fc$^+$) redox couple as a standard measured together with the samples under the same conditions, after the samples were measured. The energy level of Fc/Fc$^+$ was assumed at to be – 4.8 eV with respect to vacuum.[37] The data process followed previous work[38].The half-wave potential of the ferrocene/ferrocenium (Fc/Fc$^+$) redox couple ($E_{1/2,\ Fc,\ Fc+}$) was estimated from $E_{1/2,\ Fc,\ Fc+} = (E_{ap} + E_{cp})/2$, where E_{ap} and E_{cp} are the anodic and cathodic peak potentials, respectively. The half-wave potential of Fc/Fc$^+$ was found to be 0.453V $\{E_{1/2,\ Fc,Fc+} = (E_{ap} + E_{cp})/2 = (0.630+0.275)/2 = 0.453\ V\}$ related to the Ag/Ag+ reference electrode. The HOMO energy levels of 9-ACA and 9-ADTC were calculated using the equation: $E_{HOMO} = -(4.8 - E_{1/2,\ Fc,Fc+} + E_{ox,\ onset}) = -(4.347 + E_{ox,\ onset})$ eV, where $E_{ox,\ onset}$ is the onset oxidation potential relative to the Ag/Ag+ reference electrode. The LUMO energy levels of molecules were calculated by adding the optical gap from the respective HOMO energy levels ($E_{LUMO} = E_{HOMO} + E_{g,\ opt}$).

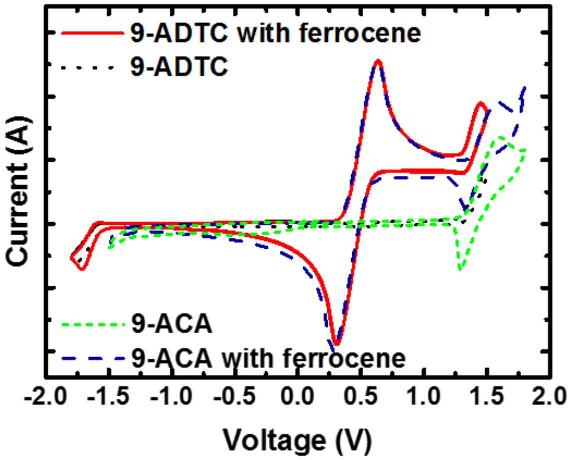

Fig. 7.22 Cyclic voltammogram of 9-ACA and 9-ADTC in dichloromethane (vs. Ag/Ag+ in dichloromethane solution with 0.1 M tetra-n-butylammonium hexafluorophosphate as supporting electrolyte, at a scan speed of 50 mV s^{-1})

7.17.2 Cyclic voltammetry of $[NMe_4][SCF_3]$ in acetonitrile

The CV of $[NMe_4][SCF_3]$ in acetonitrile is irreversible due to dimerization of the thiolate groups.[5] Half-peak potentials ($E_{p/2}$) were used to estimate the oxidation potential, $E^o_{1/2}$. The $E_{p/2}$ of $[NMe_4][SCF_3]$ is +0.99 V vs. $Ag/AgNO_3$ nonaqueous reference electrode (Ag wire in 0.01 M $AgNO_3$ acetonitrile solution).

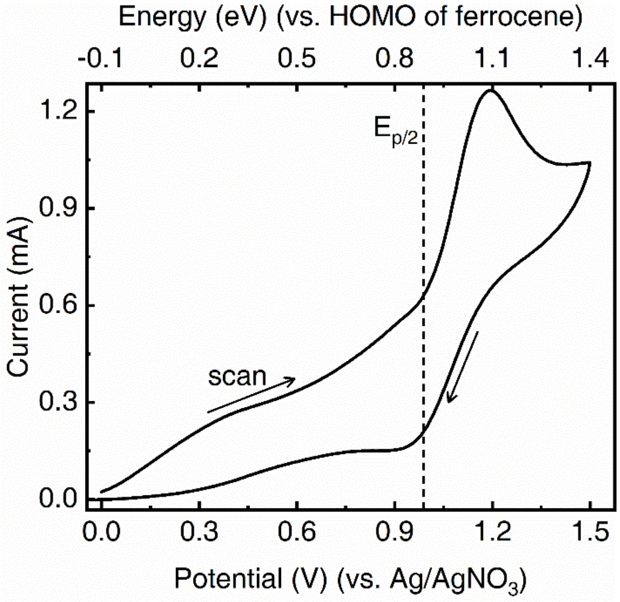

Fig. 7.23 Cyclic voltammetry of $[NMe_4][SCF_3]$ in acetonitrile at room temperature (measurement details described in the experimental section). The highest occupied molecular orbitals (HOMO) of ferrocene with respect to vacuum is –4.8 eV. The dashed line shows the half peak potential ($E_{p/2}$) position of $[NMe_4][SCF_3]$.

7.17.3 Cyclic Voltammetry measurements of the conduction band (CB) and valence band (VB) of PbS@ligand complexes

Electrochemical measurements were conducted with a WaveDriver 10 Potentiostat using a three-electrode system under Ar in an anhydrous DCM solution of tetra-n-butylammonium hexafluorophosphate (0.1 M) at - 40°C. A glassy carbon electrode was used as working electrode, a platinum-wire was used as the counter electrode, and a non-aqueous Ag/$AgNO_3$ (0.01 M $AgNO_3$ in v/v DCM: acetonitrile= 1: 5) electrode was used as the reference electrode. The electrolyte in DCM is cooled to -40°C and then the sample of PbS@SCF_3, or PbS@SCH_3 complex in toluene, or PbS@pFA in $PhCF_3$ were added into DCM solution separately such that [PbS] = 45.3 ìM. The ferrocene/ferrocenium (Fc/Fc^+) redox couple was used as a standard with a value of -4.8 eV with respect to vacuum.[6]

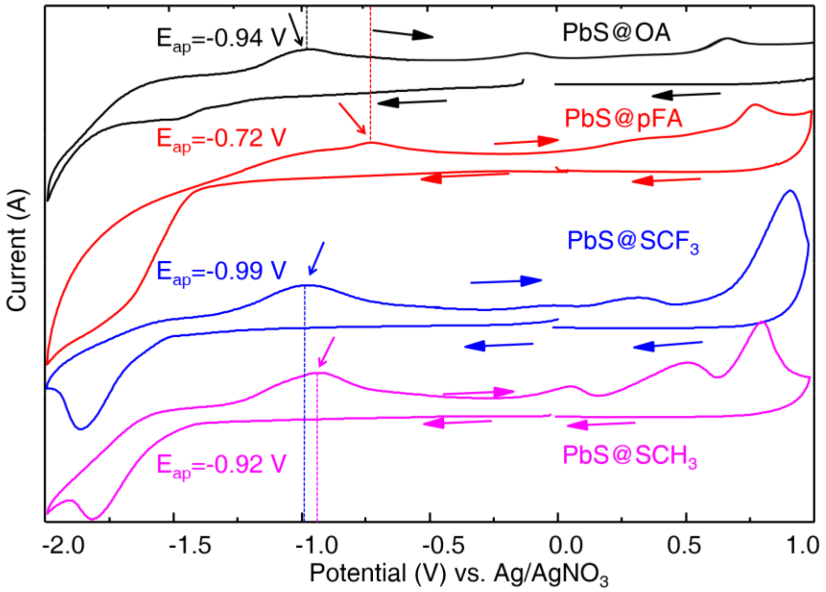

Fig. 7.24 Cyclic voltammetry (CV) of PbS QDs at -40°C. The CVs were performed in mixture of toluene and dichloromethane at a scan speed of 100 mV s^{-1}. Dash lines indicate the anodic peak (E_{ap}) positions beingused to calculate the conduction band of the QDs.

Table 7.13Solvent composition for cyclic voltammetry measurements for PbS@ligand complexes. The concentration of PbS QD is kept at 45.3 ìM during CV measurement. [ligand] is the concentration of ligand in ligand exchange and CV measurement, including pFA, -SCF_3 and -SCH_3

Complex	Solvent	[PbS]/μM	[Ligand]/mM
PbS@SCH_3	Toluene: DCM =1:2	45.3	1.81
PbS@SCF_3	Toluene: DCM =1:2		1.81
PbS@pFA	$PhCF_3$: DCM=1:2		2.26
PbS@OA	Toluene: DCM =1:2		0

7.18 Parameters used to calculate the diffusion-limited rate constant

The diffusion-controlled rate constant, k_0, is calculated from the Smoluchowski equation, eq.

7.18 with the collision radii of PbS QD and BQ at room temperature in toluene obtained from literature.[7] Here, we assume that the collision radius of PbS@ligand has no significant change in both toluene and $PhCF_3$, and is similar to the parent oleic acid capped QD because only one third of the original OA ligands were replaced by ligand exchange for the PET experiments. The diffusion limited rate constant is calculated with eq. 7.18. where R_D and R_A are the collision radii of donor (D), QDs here and acceptor (A), BQ here. D_D and D_A are diffusion coefficients of donor and acceptor and N_A is Avogadro's number. This equation describes the diffusive flux of BQ with a diffusion coefficient D_A through the surface of a sphere of radius R_D. The diffusion coefficient for PbS@pFA in $PhCF_3$ is calculated from Stokes-Einstein equation (eq. 7.19) by assuming that collision radii of D and A have no change in toluene and $PhCF_3$ solvents. k is Boltzmann's constant, η is the solvent viscosity, and R is the molecular or QDs radius.

$$k_0 = \frac{4\pi N_A}{1000}(R_D + R_A)(D_D + D_A) \qquad \text{eq. 7.18}$$

$$\mathrm{D} = \mathrm{kT}/6\pi\eta\mathrm{R} \qquad \text{eq. 7.19}$$

Table 7.14 Parameters being used to calculate the diffusion-limited rate constant, D. D_D, D_A are the diffusion coefficients for PbS QD donors and BQ acceptors. Diffusion coefficients for QD and BQ in toluene are obtained from Weiss et al.[21, 22] and Saiki et al.[20] R_A and R_D are the solvated radius of BQ and PbS@ligand, calculated from the diffusion constants in toluene. Diffusion coefficient constants of QDs and BQ are obtained from the Stokes-Einstein equation, eq. 7.19 with solvated radius of BQ and QDs in toluene.

PbS@ligan	Solven	$\eta_{solvent}/10$	$D_A/10^-$	$D_D/10^-$	R_A/n	R_D/n	$k_0/1$
PbS@OA	toluene	5.60[39]	2.26±0.01[40, 41]	1.34±0.05[42]	0.172	2.91	5.28
$PbS@SCF_3$							
PbS@SCH							
PbS@pFA	$PhCF_3$	5.55[43, 44]	2.28	1.36			5.32

7.19 Characterization of $PbS@SCF_3$ thin films

7.19.1 Applying Grazing incidence small angle x-ray scattering (GISAXS) to characterization thin film

The GISAXS has been shown in chapter 5, seen in Fig. 5.3.Here is the simulated diffraction peaks by using GIXSGUI via MATLAB.

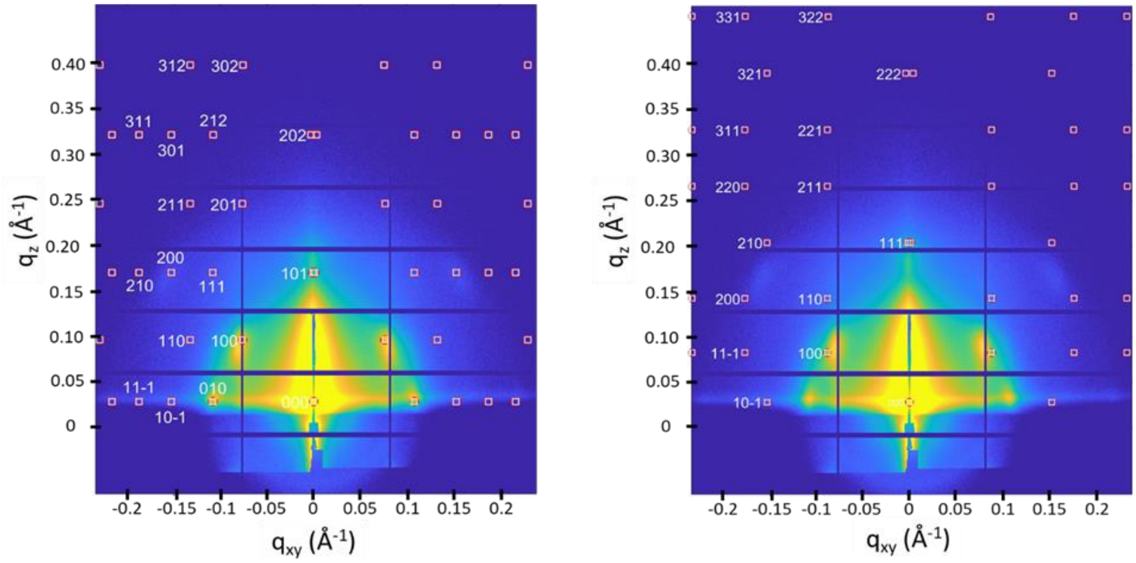

Fig. 7.25 Simulated diffraction peaks overlaid on the experimental diffraction pattern for dipcoated films before annealing. The diffraction pattern was simulated as a cubic unit cell with the (101) (a) or the (111) (b) plane parallel to the substrate. A symmetry of P_1 was used to calculate all possible peak positions without considering the specific symmetry of the lattice. Due to limited number of peaks, space group and symmetry could not be determined.

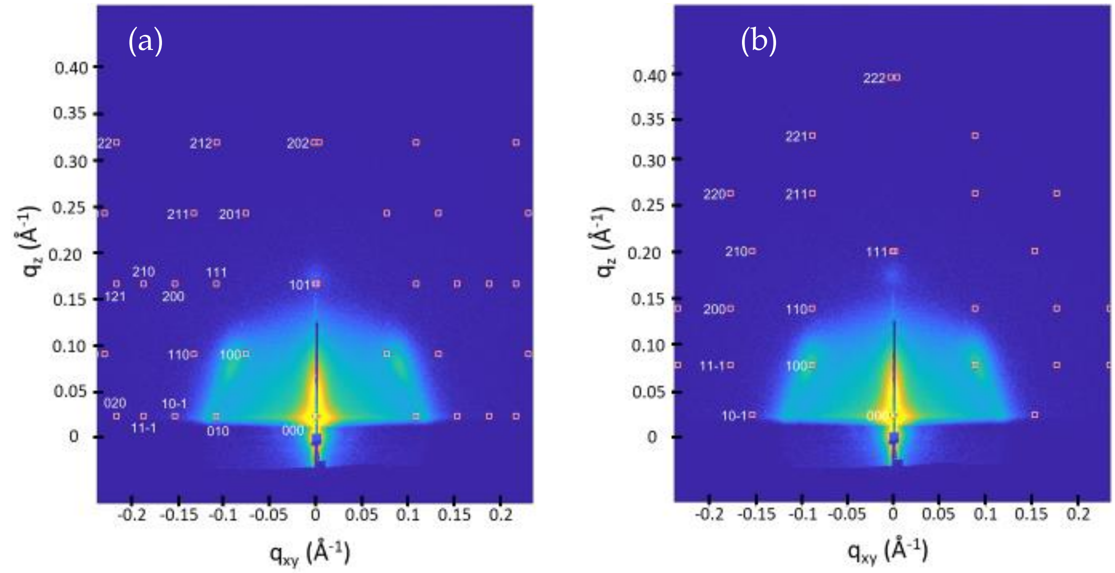

Fig. 7.26 Simulated diffraction peaks overlaid on the experimental diffraction pattern for dipcoated films before annealing. The diffraction pattern was simulated as a cubic unit cell with the (101) (a) or the (111) (b) plane parallel to the substrate. A symmetry of P_1 was used to calculate all possible peak positions without considering the specific symmetry of the lattice.

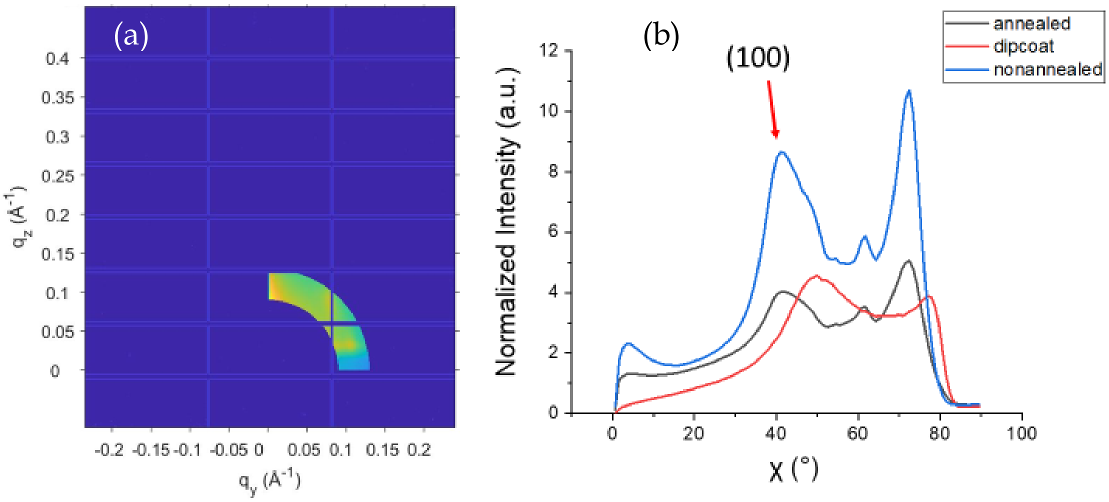

Fig. 7.27 (a) Plotted region mask and (b) reshaped χ-Q plot comparing the normalized intensity among the annealed, nonannealed and dipcoated samples. The intensities were normalized with respect to the exposure time and sample thickness. We also made a geometric correction to the intensity through multiplying by a factor of sin(χ).

7.19.2 Optical characterization of partial-ligand-exchanged PbS–OA+SCF$_3$ QDs

OA capped PbS QDs were ligand exchanged in a mixture of toluene and acetonitrile with [NMe$_4$][SCF$_3$] to replace one third of OA with $\ominus$SCF$_3$ ligands. Optical characterization of partial-ligand-exchanged PbS QD, PbS–OA+SCF$_3$ is shown in Fig. 7.28.

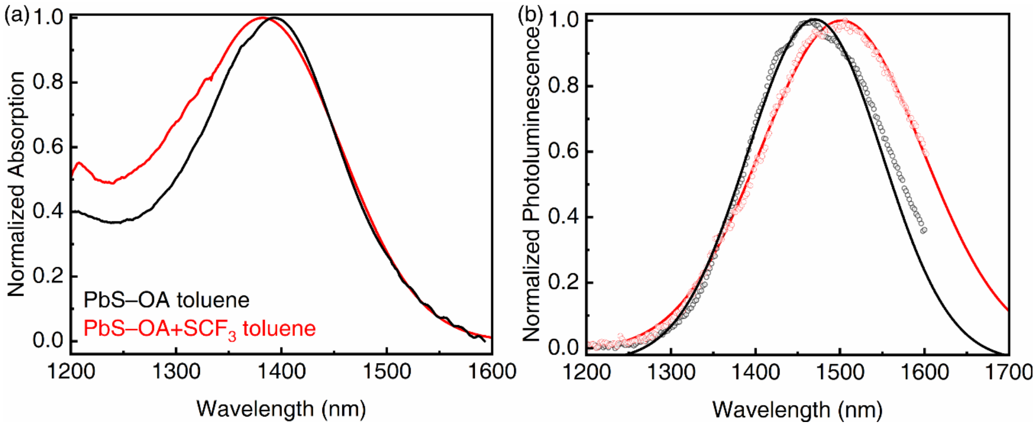

Fig. 7.28 (a) Optical absorption and (b) photoluminescence (PL) of PbS QDs capped with OA, PbS–OA (black) and PbS–SCF$_3$+OA (red, OA: SCF$_3$ = 2:1) in toluene with 488 nm excitation. The blue shift of the 1st exciton peak and red shift of the PL are in agreement with our previous work on PbS QDs with diameter=3.8nm.[31]

7.19.3 Transmission electron microscopy characterization of PbS–SCF_3 superlattice film

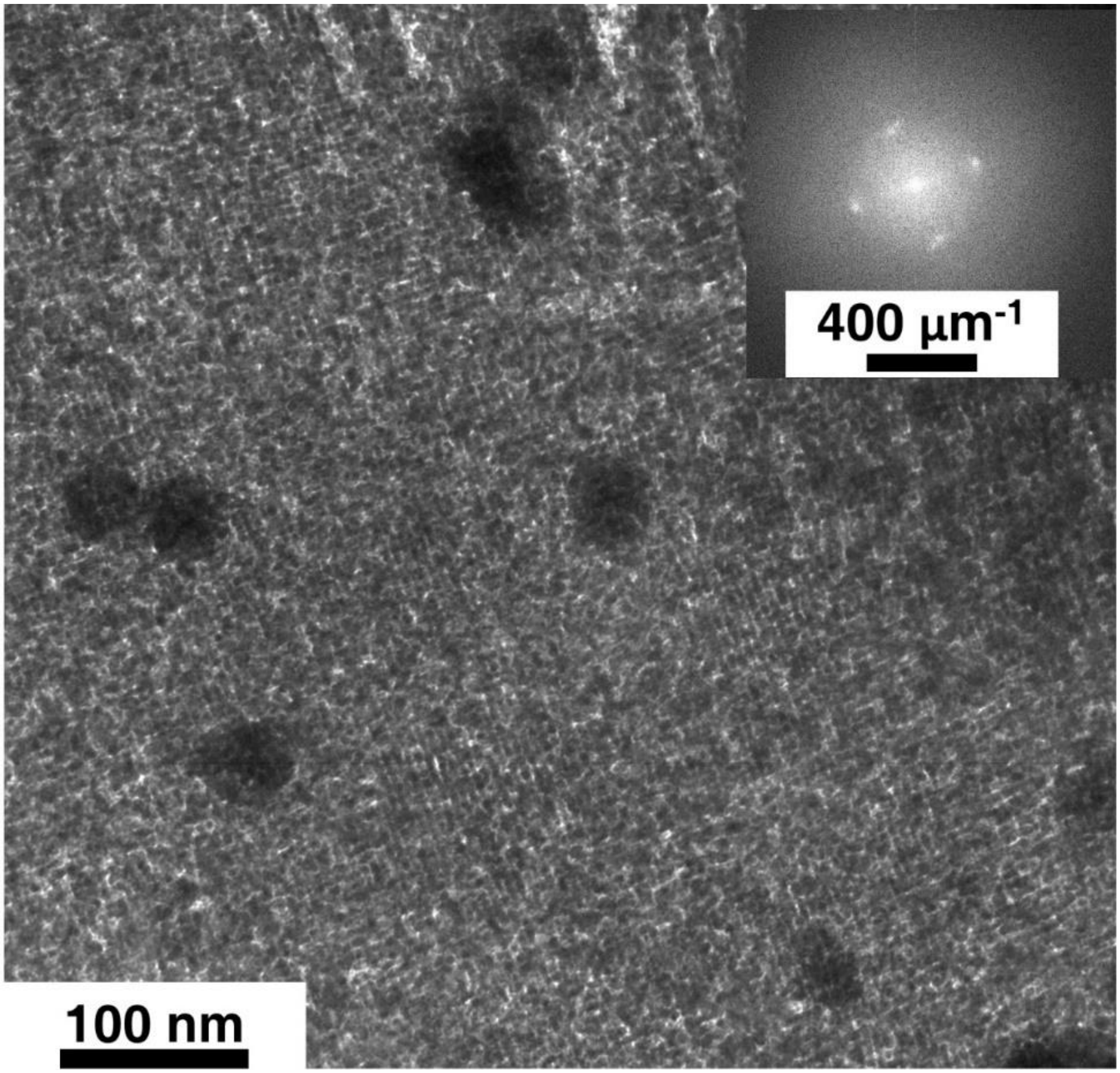

Fig. 7.29 TEM images of PbS–SCF_3 QD superlattice with local area 650 nm x 650 nm. The insert is the corresponding FFT image with two pairs of scattering spots stemming from long range order of the QDs. There are some polymeric impurities visible.

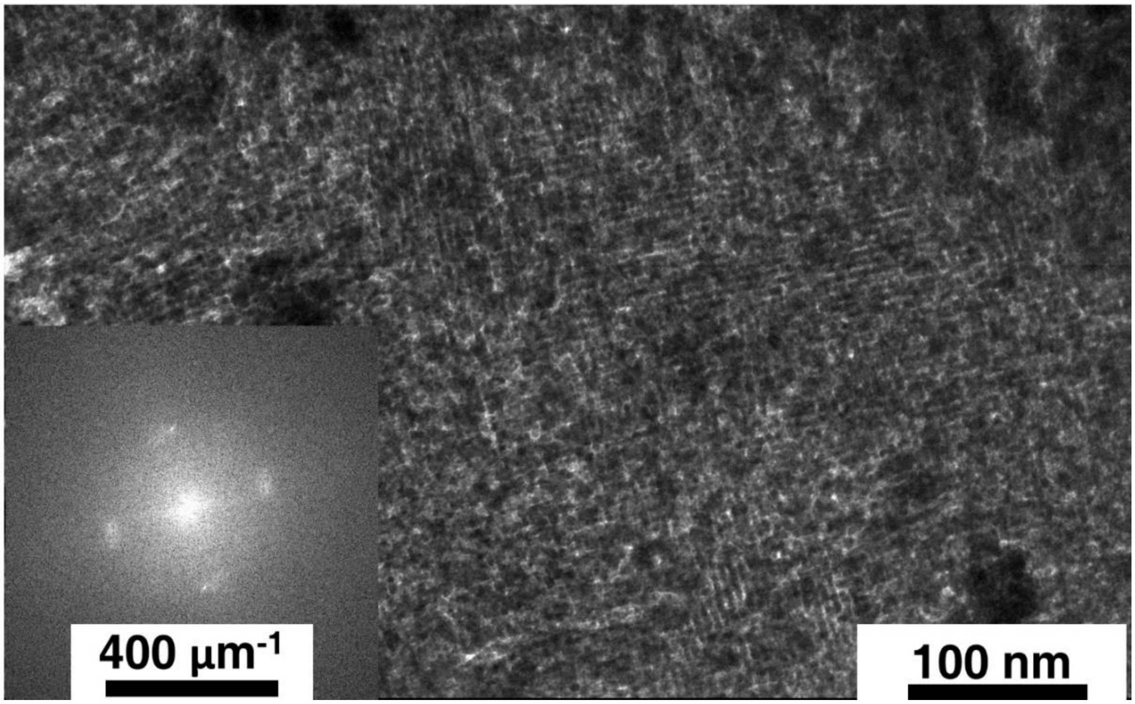

Fig. 7.30 Additional TEM images of the PbS QD superlattice with local area 760 nm x 300 nm. The insert is the corresponding FFT image with two pairs of scattering spots.

8.14.4 Atomic force microscope (AFM) images of dipcoating PbS–SCF_3 QDs film

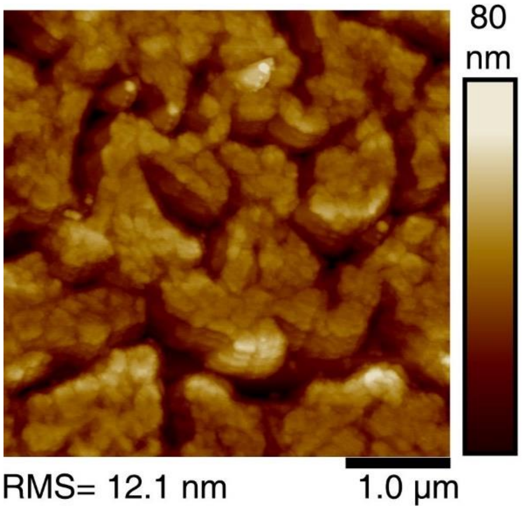

Fig. 7.31 AFM images of dipcoating PbS–SCF_3 QDs film without annealing.

7.19.4 Ultraviolet photoelectron spectroscopy (UPS)

The conduction band (CB) minimum, E_C, is estimated by adding the energy of the valence band (VB) maximum, optical band gap, E_g^{opt} and the Coulombic stabilization energy of the confined electron and hole as described previously.[45]

$$E_C = E_V + E_G^{opt} + 1.786\frac{e^2}{4\pi\varepsilon_0\varepsilon_{QD}R} \qquad \text{eq. 7.20}$$

where e is the charge of the electron, ε_0 is the permittivity of free space, ε_{QD} is the optical dielectric constant of the QD core material, and R is the quantum dot radius (determined by matching the first absorption peak in solution to a published sizing curve[13]).

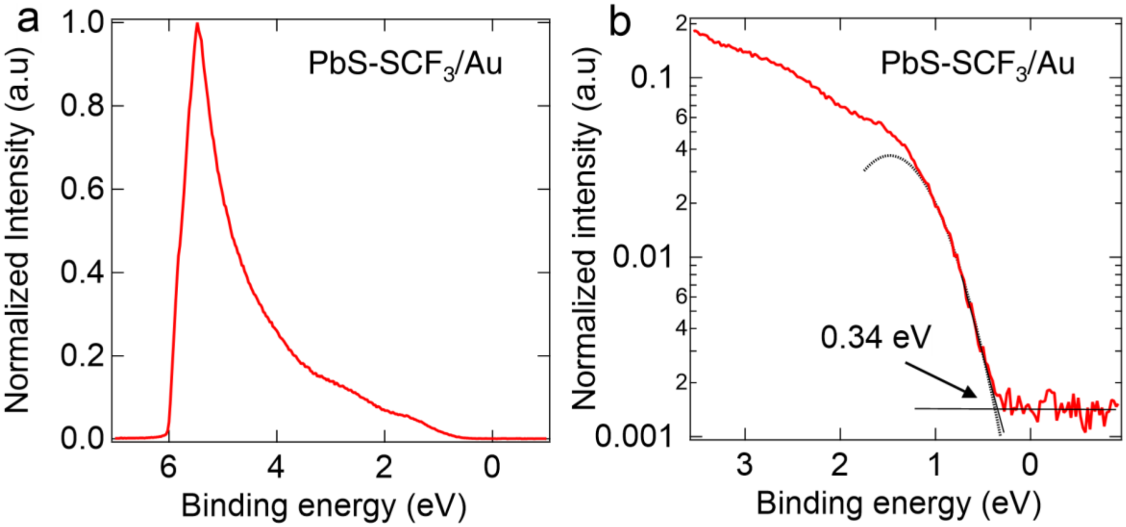

Fig. 7.32 UPS spectra measured with a 10.2 eV H Lyman-α lamp of PbS–SCF$_3$ QD thin films on gold coated silicon wafer. (a) Complete spectra on a linear scale, which clearly shows the secondary electron cut-off region, and (b) the valence band onset region on a semi-log plot.

Table 7.15 Parameters of UPS samples of PbS–SCF$_3$ thin film on gold coated substrate. The lack of a well-defined valence band (VB) onset in the UPS measurements and the use of a logarithmic plot to extract the VB onset introduces some uncertainty (ca. ± 0.1 eV) due to the assignment of the background level. For example, different UPS systems will have different signal to noise ratios that will likely influence where the background intersects the parabolic fit. The work function (Φ), VB maximum (E_V), and VB onset relative to the Fermi energy are obtained from Fig. 7.32. E_g^{opt} is the optical bandgap from optical absorption spectra. Coulombic stabilization energy (eV) of the confined electron and hole and energy of conduction band (CB) minimum (E_C) are calculated with eq. 7.20.

Sample	Substrate	Φ (eV)	VB onset (eV)	E_V (eV)	λ_{max} [1] (nm)	E_g^{opt} (eV)	Coulombic stabilization energy (eV)	E_C (eV)
PbS–SCF_3 /Au	Au	4.20	0.34	-4.54	1420	0.87	0.085	-3.58
[1] λ_{max} is the first exciton absorption maximum of dipcoating PbS–SCF_3 film.								

7.20 Thin film field-effect transistor measurements

Average hole mobilities μ_{AVE} were calculated from transfer curves acquired at source drain voltage, $V_{DS} = –70/ –80$ V, in the saturation regime with equation:

$$\mu = \left(\frac{\partial\sqrt{|I_{DS}|}}{\partial V_G}\right)^2 \frac{2L}{WC_i} \qquad \text{eq. 7.21}$$

Where W is the channel width, L is the channel length, and C_i is the capacitance per unit area of the gate oxide. The carrier mobilities reported here are averages of 3−5 devices.

The I-V curves are non-ideal with two slopes. Here, two slopes are used to calculate the carrier mobility as described by Phan et al and Choi et al.[46, 47] Since the gate voltages, V_G, can be scanned from positive to negative, or vice-versa, we plot four mobility values. Considering the crystalline domains of the PbS QD superlattice are on the order of the channel lengths, it is not surprising that there is some deviation between devices. However, annealed PbS QD thin films fabricated on 3-MPTMS thiol SAMs only show one slope, unlike the TFTs presented in Fig. 7.33 below.

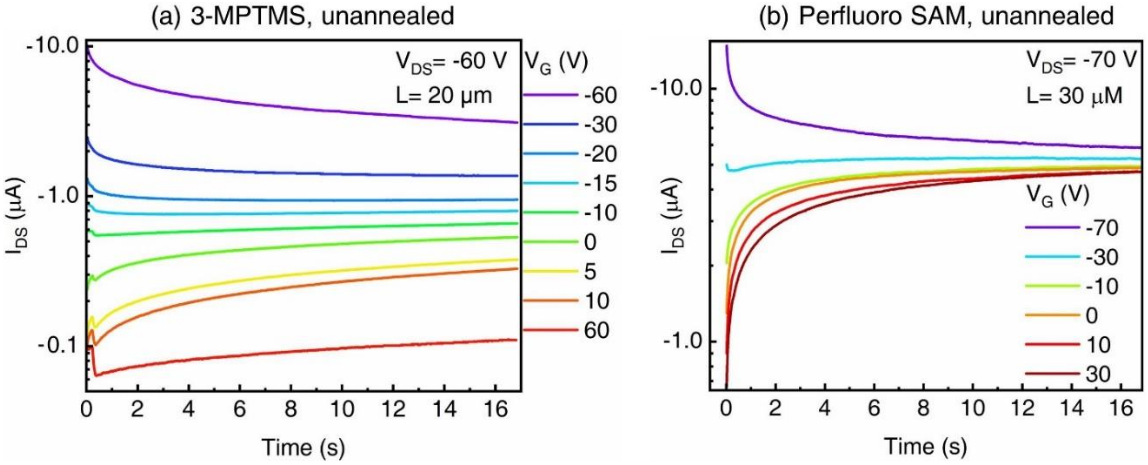

Fig. 7.33 Bias stress curves for unannealed PbS–SCF_3 QD thin films spin-coated on (a) 3-MPTMS treated or (b) perfluoro treated dielectric (b) where $V_{DS} = -60$ and -70 V respectively as the gate voltage, V_G is varied. In both 3-MPTMS treated or perfluoro treated substrate, the source drain current, I_{DS} decreases in magnitude over time, indicating that the hole current is trapped and not related to the dielectric treatment.

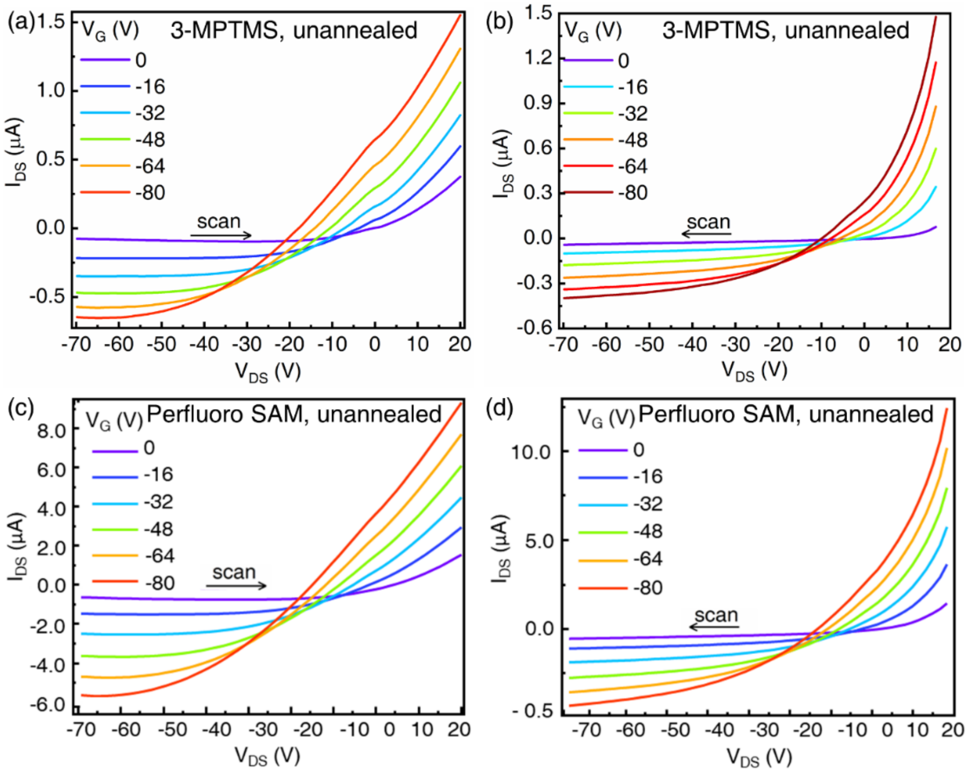

Fig. 7.34 Typical output curves of unannealed PbS–SCF_3 QD thin film transistors (TFTs) with (a, b) 3-MPTMS self-assembled monolayer (SAM) and (c, d) perfluoro SAM on dielectric. Arrows indicate the direction V_{DS} is swept.

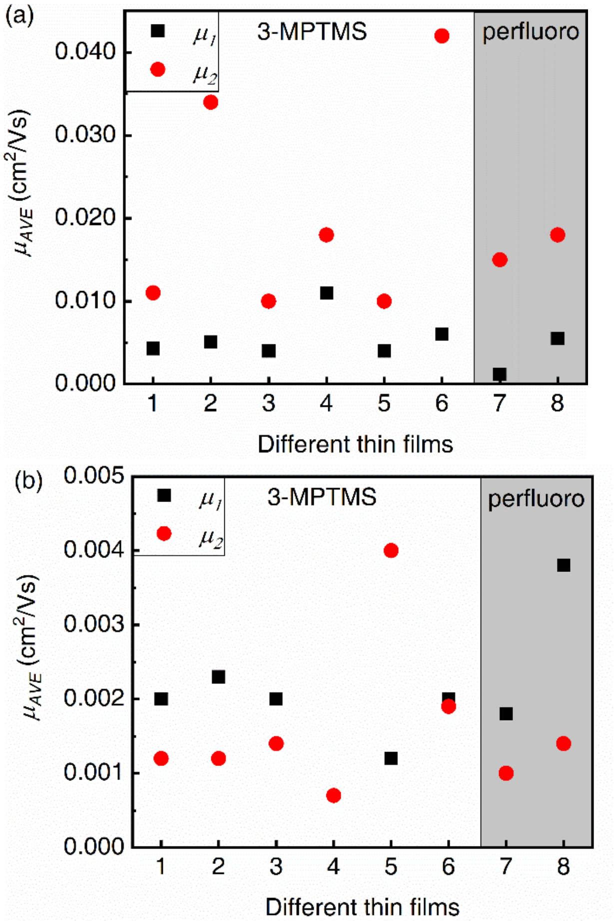

Fig. 7.35 Hole mobilities of TFTs with different SAMs treating the dielectric (3-MPTMS and perfluoro), comparing scanning V_G from negative to positive (a) and vice-versa (b).

PbS–SCF$_3$ film fabricated via dipcoating

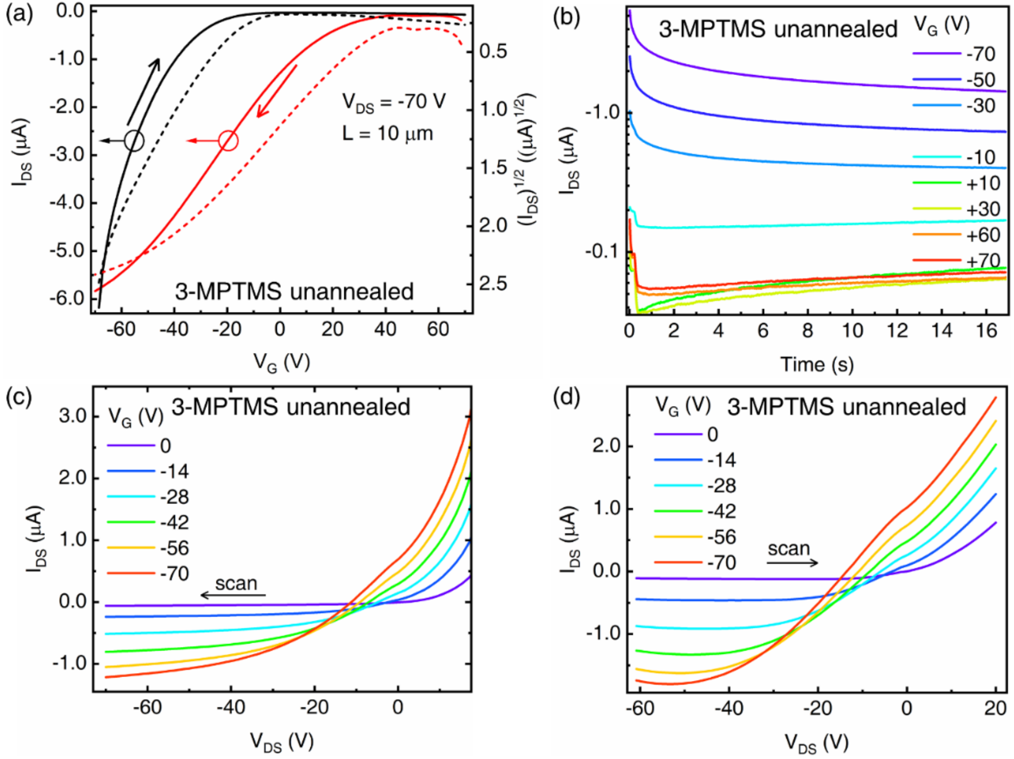

Fig. 7.36. Representative transfer and output curves of dipcoated PbS–SCF$_3$ QD FETs with 3-MPTMS SAM on dielectric. Channel length is 10 μm (a) Transfer curves with source drain voltage, V_{DS}, is kept at −70 V. (b) Bias stress curves of the dipcoating PbS–SCF$_3$ QD thin films where V_{DS} = −70 V, is held as the gate voltage, V_G is varied. The source drain current, I_{DS}, decreases in magnitude over time, indicating that the hole current is trapped. Output curves scanning from (c) negative to positive V_{DS} and (d) positive to negative V_{DS}.

Table 7.16. Summary of transistor performance, including the maximum and average mobilities, μ_{MAX} and μ_{AVE}, the threshold voltage, V_T, and the on/ off ratios, I_{ON} / I_{OFF} corresponding to dipcoated PbS–SCF$_3$ film transistor in Fig. 7.35and Fig. 7.36.

Channel length (μm)	30		20		20	
Scan towards	+V_G	-V_G	+V_G	-V_G	+V_G	-V_G
μ_{AVE} [cm^2/Vs]	0.006	0.003	0.007	0.003	0.006	0.002
μ_{MAX} [cm^2/Vs]	0.020	0.005	0.023	0.005	0.019	0.004
I_{ON}/ I_{OFF}	200	100	200	100	200	100
V_T [V]	-10	+30	-10	+40	-15	+50

7.21 Notes and References

1. Li X, *et al.* Distance Dependent Triplet Energy Transfer between CdSe Nanocrystals and Surface Bound Anthracene. *J Phys Chem Lett* 2016.

2. Boehm AM, *et al.* A new photon source for ultraviolet photoelectron spectroscopy of organic and other damage-prone materials. *Org Electron* 2017, 41: 9-16.

3. Albrecht C. Joseph R. Lakowicz: Principles of fluorescence spectroscopy. *Anal. Bioanal. Chem* 2008, 390(5): 1223-1224.

4. Jiang Z. GIXSGUI: a MATLAB toolbox for grazing-incidence X-ray scattering data visualization and reduction, and indexing of buried three-dimensional periodic nanostructured films. *J Appl Cryst* 2015, 48(3): 917-926.

5. Roth HG, *et al.* Experimental and calculated electrochemical potentials of common organic molecules for applications to single-electron redox chemistry. *Synlett* 2016, 27(05): 714-723.

6. Knowles KE, *et al.* Dual-Time Scale Photoinduced Electron Transfer from PbS Quantum Dots to a Molecular Acceptor. *J Am Chem Soc* . 2012, 134(30): 12470-12473.

7. Meites L. *Handbook of analytical chemistry*. McGraw-Hill: New York, 1963.

8. Liang Z, *et al.* Influence of dopant size and electron affinity on the electrical conductivity and thermoelectric properties of a series of conjugated polymers. *J Mater Chem A* 2018, 6(34): 16495-16505.

9. Carbone L, *et al.* Synthesis and micrometer-scale assembly of colloidal CdSe/CdS nanorods prepared by a seeded growth approach. *Nano Lett* 2007, 7(10): 2942-2950.

10. Yu WW, *et al.* Experimental determination of the extinction coefficient of CdTe, CdSe, and CdS nanocrystals. *Chem Mater* 2003, 15(14): 2854-2860.

11. Kubin RF, *et al.* Fluorescence quantum yields of some rhodamine dyes. *J Lumin* 1983, 27(4): 455-462.

12. Hendricks MP, *et al.* A tunable library of substituted thiourea precursors to metal sulfide nanocrystals. *Science* 2015, 348(6240): 1226-1230.

13. Moreels I, *et al.* Size-Dependent Optical Properties of Colloidal PbS Quantum Dots. *ACS Nano* 2009, 3(10): 3023-3030.

14. Zhang J, *et al.* PbSe Quantum Dot Solar Cells with More than 6% Efficiency Fabricated in Ambient Atmosphere. *Nano Letters* 2014, 14(10): 6010-6015.

15. Zhu J, *et al.* Design, synthesis, X-ray crystallographic analysis, and biological evaluation of thiazole derivatives as potent and selective inhibitors of human dihydroorotate Dehydrogenase. *J Med Chem* 2015, 58(3): 1123-1139.

16. Hong C, *et al.* Novel aromatic–polyamine conjugates as cholinesterase inhibitors with notable selectivity toward butyrylcholinesterase. *Biorg Med Chem* 2014, 22(12): 3213-3219.

17. Tyrra W, *et al.* A new synthesis of trifluoromethanethiolates—characterization and properties of tetramethylammonium, cesium and di (benzo-15-crown-5) cesium trifluoromethanethiolates. *J. Fluor. Chem.* 2003, 119(1): 101-107.

18. Yin G, *et al.* Trifluoromethylthiolation of Aryl Iodides and Bromides Enabled by a Bench-Stable and Easy-To-Recover Dinuclear Palladium(I) Catalyst. *Angew Chem Int Ed* 2015, 54(23): 6809-6813.

19. Morris JV, *et al.* Fluorescence quantum yield determinations. 9, 10-Diphenylanthracene as a reference standard in different solvents. *J Phys Chem* 1976, 80(9): 969-974.

20. Reineke S, *et al.* Room temperature triplet state spectroscopy of organic semiconductors. *Sci. Rep* 2014, 4.

21. Padhye MR, *et al.* Lowest triplet state of anthracene. *J Chem Phys* 1956, 24(3): 588-594.

22. Kellogg R. Second triplet state of anthracene. *J Chem Phys* 1966, 44(1): 411-412.

23. Gee N, *et al.* Relative permittivities of 10 organic liquids as functions of temperature. *J. Chem. Thermodyn.* 1993, 25(4): 549-554.

24. Abjean R, *et al.* Refractive index of carbon tetrafluoride (CF4) in the 300-140 nm wavelength range. *Nuclear Instruments and Methods in Physics Research Section A: Accelerators, Spectrometers, Detectors and Associated Equipment* 1990, 292(3): 593-594.

25. Straty G, *et al.* Dielectric constant and polarizability of saturated and compressed fluid methane. *Cryogenics* 1973, 13(12): 712-715.

26. Rollefson R, *et al.* Index of Refraction of Methane in the Infra-Red and the Dipole Moment of the CH Bond. *Physical Review* 1940, 57(8): 710-717.

27. Champion JV, *et al.* Electro-optic Kerr effect in n-alkane liquids. *J. Chem. Soc. Faraday Trans* 1970, 66(0): 2671-2680.

28. Haynes WM. *CRC Handbook of Chemistry and Physics, 95th.* CRC press: Boca Raton, 2014.

29. Lifanova N, *et al.* Molecular-Structure Of Certain Perfluorocarbon Compounds Based on Equilibrium Dielectric-Properties Data. *Zhurnal Fizicheskoi KhimiI* 1992, 66(1): 237-240.

30. Banus J, *et al.* 12. The heterolytic fission of the carbon-iodine bond in trifluoroiodomethane. *Journal of the Chemical Society (Resumed)* 1951(0): 60-64.
31. Xia P, *et al.* Surface Fluorination for Controlling the PbS Quantum Dot Bandgap and Band Offset. *Chem Mater* 2018, 30(15): 4943-4948.

32. Huang Z, *et al.* Hybrid molecule–nanocrystal photon upconversion across the visible and near-infrared. *Nano letters* 2015, 15(8): 5552-5557.

33. Mongin C, *et al.* Direct observation of triplet energy transfer from semiconductor nanocrystals. *Science* 2016, 351(6271): 369-372.

34. Hudson RL. Infrared spectra and band strengths of CH3SH, an interstellar molecule. *Phys. Chem. Chem. Phys.* 2016, 18(36): 25756-25763.

35. Sillen A, *et al.* The correct use of "average" fluorescence parameters. *Photochem Photobiol* 1998, 67(5): 475-486.

36. Hendricks MP, *et al.* A tunable library of substituted thiourea precursors to metal sulfide nanocrystals. 2015.

37. Liu Y, *et al.* Synthesis and characterization of a novel and highly efficient light-emitting polymer. *Acta Polym* 1999, 50(2-3): 105-108.

38. Deng P, *et al.* N-acylation: an effective method for reducing the LUMO energy levels of conjugated polymers containing five-membered lactam units. *Chem Commun* 2012, 48(55): 6960-6962.

39. Rumble JR (ed). *CRC Handbook of Chemistry and Physics 98th edition*. CRC Press/Taylor & Francis: Boca Raton, FL., 2018.

40. Saiki H, *et al.* Diffusion of porphyrins and quinones in organic solvents. *Phys. Chem. Chem. Phys.* 1999, 1(2): 303-306.

41. Weinberg DJ, *et al.* Control of the Redox Activity of Quantum Dots through Introduction of Fluoroalkanethiolates into Their Ligand Shells. *J. Am. Chem. Soc*. 2016, 138(7): 2319-2326.

42. Aruda KO, *et al.* Temperature-Dependent Permeability of the Ligand Shell of PbS Quantum Dots Probed by Electron Transfer to Benzoquinone. *J Phys Chem Lett.* 2015, 6(14): 2841-2846.

43. De Lorenzi L, *et al.* Density and Viscosity of 1-Methoxy-2-Propanol, 2-Methyltetrahydrofuran, α,α,α-Trifluorotoluene, and Their Binary Mixtures with 1,1,1-Trichloroethane at Different Temperatures. *J. Chem. Eng. Data* 996, 41(5): 1121-1125.

44. Lorenzi LD, *et al.* Densities and Viscosities of 1,1,1-Trichloroethane with 13 Different Solvents at 298.15 K. *J. Chem. Eng. Data* 1995, 40(6): 1172-1177.
45. Brown PR, *et al.* Energy Level Modification in Lead Sulfide Quantum Dot Thin Films through Ligand Exchange. *ACS Nano* 2014, 8(6): 5863-5872.

46. Phan H, *et al.* Electrical Double-Slope Nonideality in Organic Field-Effect Transistors. *Adv Funct Mater* 2018, 28(17): 1707221.

47. Choi HH, *et al*. Critical assessment of charge mobility extraction in FETs. *Nat Mater* 2017, 17(1): 2-7.